Dephasing and Quantum Noise in an electronic Mach-Zehnder Interferometer

Dissertation
zur Erlangung des Doktorgrades der Naturwissenschaften
(Dr. rer. nat.)
der Fakultät für Physik
der Universität Regensburg
vorgelegt von
Andreas Helzel
aus Kelheim

Dezember 2012

Promotionsgesuch eingereicht am: 22.11.2012

Die Arbeit wurde angeleitet von: Prof. Dr. Christoph Strunk

Prüfungsausschuss:
Prof. Dr. G. Bali (Vorsitzender)
Prof. Dr. Ch. Strunk (1. Gutachter)
Dr. F. Pierre (2. Gutachter)
Prof. Dr. F. Gießibl (weiterer Prüfer)

In Gedenken an Maria Höpfl.
Sie war die erste Taxifahrerin von Kelheim und wurde 100 Jahre alt.

Contents

List of Figures

1. Introduction

"You are not thinking. You are merely being logical."

Niels Bohr to Albert Einstein
during their great debate on Quantum Mechanics

Dephasing, i.e. decoherence is the loss of quantum interference due to interactions of the interfering degree of freedom with the many degrees of freedom of the environment. Since no quantum mechanical system is perfectly decoupled from its environment, decoherence and dephasing is an important subject to understand the evolution of the states of a system and to utilize them in an application as a quantum computer or in quantum cryptography. It is subject to active research only since the 1980s [1]. Before this time the problem was treated only rather "philosophically" by the known collapse of the wave function by a classical macroscopic measurement apparatus in the Copenhagen interpretation of quantum mechanics. For this reason dephasing is closely related to the measurement problem of quantum mechanics, because this describes a decoherence process as well. Even when a single state interacts with a second state, the time evolution of their product state will lead to an entangled state. And this can lead to surprising effects of this quantum correlations of a state or a system with its environment. So the investigation of dephasing is attended by the recognition of the fundamental importance of entanglement of quantum systems or states.
The question arises here if this interaction between a system of interest and its environment can only be explained by the randomization of the phases of the states, or if it is also important how the system influences the environment and if these effects are equivalent or must be distinguished. The first is an almost classical view that the environment acts as a perturbance on the system, while the second is more abstract, because the decoherence is due to the information the environment "measures" on the system.
It was together with the advent of *mesoscopic physics* that these decoherence effects were studied more and more extensively in the physics community. Dephasing describing a process where the behavior of a quantum mechanical particle (or system) becomes gradually classical, due to interaction with the environment, can be best investigated in systems which are at the border between the microscopic, pure quantum mechanical world and the macroscopic classical world. They range from few nanometers (such as large molecules [2], carbon nanotubes [3], or self assembled quantum dots [4]) up to several micrometers (as in 2DEG material with large Fermi wave lengths and large mean

free paths). These sizes are now accessible for technological processing and this offers the possibility to control most parameters of a quantum mechanical system. For example one can realize in a two-dimensional electron gas by applying metal top gates and charging them negatively the typical textbook problem of a particle in a box, a so-called quantum dot [5]. With these gates the size of this electron box and thus the level structure as well as the tunnel coupling to the leads/environment can be modified and one obtains an artificial atom that can be fully controlled. To ensure large coherence lengths and to reduce/control thermal influence of the environment, experiments of mesoscopic system require low temperature (<4 K). Then one can investigate in a controlled way how certain parameters, such as magnetic field, a bias voltage, or temperature influence quantum effects. Coherence lengths are determined very often by measuring the width of a weak localization peak in the conductance in the magnetic field dependence [6, 7].
Maybe the most intuitive way to learn about the coherence of processes is by measuring the *interference* of the states of interest. 1802 the first double slit experiment with light was conducted by Thomas Young. After that more sophisticated interferometers were constructed, most famously the Michelson-Morley experiment 1887, that disproved the ether theory [8]. More than 150 years after Young the first double slit experiment with particles, electrons, was done by Claus Jönsson in 1961 [9], followed by the intriguing experiment by Tonomura et al. [10] which shows nicely how a pattern of interference fringes develops out of single electrons, arriving one by one at a screen. What better way to say "You are both right!" to the dispute, that went on for decades (even centuries concerning light), whether there are waves or particles. Particle-wave duality could be even shown for C_{60} molecules [11].
A basis which is more favored when thinking about quantum information processing and quantum computers is solid state physics. Here, for example, a double slit like experiment was performed by Yacoby et al. [12] in a two-dimensional electron gas (2DEG), where the double slit was realized by metallic top gate structures. Interference experiments in normal-metal rings are here of less importance due to their low coherence lengths [13]. After the first simple interference experiments in a 2DEG soon more sophisticated interferometers were developed, such as Fabry-Perot interferometers [14] or the for this work important Mach-Zehnder interferometers [15]
Quantum noise is a term which is used for any noise that originates from quantum mechanical effects. For example, at (almost) zero temperature, noise arises from zero-point fluctuations. As soon as the lowest energy of a system exceeds $E_0 > k_\mathrm{B}T$, thermal fluctuations play a minor role and one arrives at a general lower bound of noise due to the zero-point fluctuations [16]. Another famous example, as well in optics [17] as in mesoscopic electronic systems [18], is the so-called *shot noise*, predicted by Walter Schottky in 1918 for vacuum tubes, whose origin is the *granularity*, i.e. the quantum, of charges involved in the process [19]. Shot noise can even reveal some of the quantum mechanical nature and the correlations in a system, when it is reduced from its expected value,

as described by the Fano factor [20–22].

In this thesis an electronic Mach-Zehnder interferometer operated with quantum Hall edge channels, as first shown in Ref. [15], is investigated. A Mach-Zehnder interferometer is a very straight forward two beam interferometer. A single mode beam of particles is partitioned by a beam splitter, the partial waves accumulate a certain phase difference $\Delta\varphi$ along the two paths, and are merged again in a second beam splitter where they interfere. Depending on the phase difference $\Delta\varphi$, constructive interference is observed in one of two drains. An interferometer of such kind offers a direct possibility to learn more about dephasing effects in the integer quantum Hall regime. In addition, as a solid state two-path interferometer and its sensitivity to phase differences, it is suitable as a detector for states of adjacent quantum systems, as for example a qbit or a quantum point contact (QPC) [23].
To follow the subsequent presentation of the experiments on the Mach-Zehnder interferometer, chapter 2 gives an overview of all the basic concepts needed. Emphasis is put here on the transport properties of the quantum Hall edge, of which the interferometer transport channels are made up of, especially when there are two edge channels present. From this one can deduce many of the characteristics of an electronic Mach-Zehnder interferometer. Another building block of the Mach-Zehnder interferometer are QPCs, which either serve as beam splitters and as quantum mechanical systems under investigation. Since they are also operated at finite voltage bias, non-equilibrium noise of a QPC is described in terms of the full counting statistics (FCS). This chapter ends with a description of the Aharonov-Bohm effect, interferometers based in it, and as a special case of this basic properties of an electronic Mach-Zehnder interferometer.
Proximate chapters 3 and 4 deal with the measurement setup and the fabrication of a Mach-Zehnder interferometer.
The first experimental part, chapter 5, displays measurements of electronic Mach-Zehnder interferometers alone, to describe their properties. Such as the dependence of the coherence, expressed in the parameter “visibility”, on temperature, or especially on a bias voltage, for which the Mach-Zehnder interferometer shows rich characteristics.
In the experiment described in chapter 6, these characteristices of the Mach-Zehnder interferometer are used to investigate the non-equilibrium noise produced of a QPC. This QPC is placed upstream of the interferometer and the fluctuating current is directly injected into the interferometer. For this setting a noise-induced phase transition was predicted due to the strong coupling of the Mach-Zehnder interferometer with all current cumulants of the FCS generator of the QPC.

2. Basics

"Everything we call real is made of things that cannot be regarded as real."

Niels Bohr

In this chapter I will describe basic concepts and theories needed for this work. The first section is a very brief review of the two-dimensional electron gas (2DEG) in semiconductor heterostructures. The following section, representing the main part of this chapter, deals with the quantum Hall effect in general and especially the electron transport in the quantum Hall edge channels. After discussing non-equilibrium noise, the last sections are concerned with the Aharonov-Bohm effect and electronic interferometers.

2.1. The two dimensional electron gas

Even in times of electron transport through large single molecules, carbon nanotubes and graphene monolayers, two dimensional electron systems in semiconductor heterostructures are the basic building block of mesoscopic physics. The most popular material is GaAs/AlGaAs due to the possibility to produce low density and high mobility samples which are easy for subsequent structuring. In the following I will give an account of the according chapter in Ref. [24] if not stated differently.
Starting point are two semiconductors with different electron affinity and different band gap, but (almost) the same lattice constant. In this work GaAs is used with a band gap of $\approx 1.4\,\mathrm{eV}$ and $\mathrm{Al}_x\mathrm{Ga}_{1-x}\mathrm{As}$ with $1.4 - 2.2\,\mathrm{eV}$ (depending on the percentage of Al). Due to matching lattice constants of 5.65 Å they are an appropriate combination as a heterostructure. The materials are deposited by molecular beam epitaxy with a minimum of crystallographic defects. A possible layer sequence is depicted in Fig. 2.1 where the direction of the layer growth is denoted as the z-direction. Of particular importance is the interface between GaAs spacer and AlGaAs substrate, where the band gap shows an abrupt jump. To equilibrate the Fermi energy E_F a charge redistribution occurs, such that electrons diffuse particularly from the Si-doped AlGaAs layer through the AlGaAs spacer into the GaAs substrate, leading to a distortion of the band structure as shown in Fig. 2.1. Thus a narrow (triangular) potential minimum forms at the GaAs/AlGaAs interface reaching below E_F. This is a so called quantum well in the z-direction and

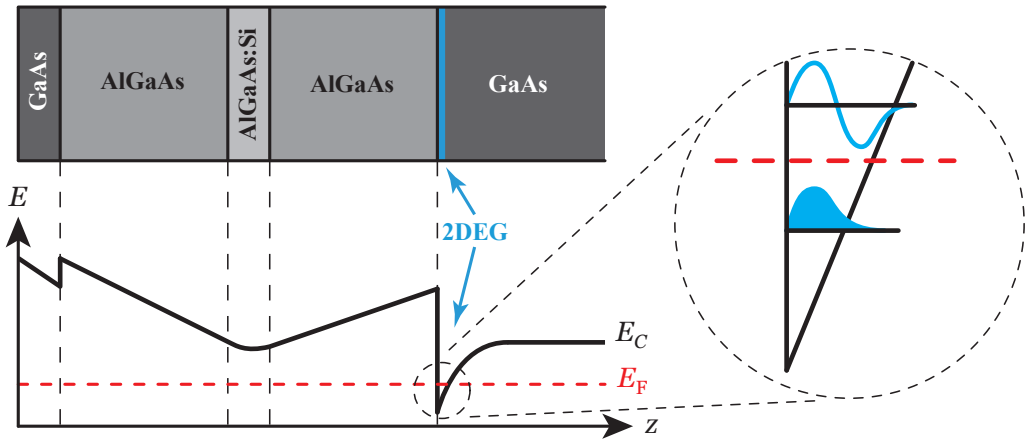

Figure 2.1.: Typical layer sequence of a GaAs/AlGaAs heterostructure and the according development of the conduction band E_C. The enhanced view shows the triangular potential well of the conduction band at the GaAs/AlGaAs interface. Only the lowest bound state (possible wave function indicated in light blue) lies beneath the Fermi energy (red) and forms the 2DEG.

when only its lowest subband is occupied (see zoom in Fig. 2.1) one speaks of a two-dimensional electron gas (2DEG), since electrons in there are localized in z-direction, but can move freely in the x-y-plane. The remaining positively charged donors in the doping layer cause a random potential, which results in an enhanced electron scattering in the 2DEG. A thicker spacer layer will increase screening and reduce this negative effect.

The confinement potential at the interface leads to the formation of subbands with a density of states

$$N(E) = \frac{m^*}{\pi\hbar^2}\theta(E - E_\mathrm{s}), \tag{2.1}$$

with m^* being the effective electron mass in GaAs, θ the unit step function and E_s the lower cut-off of the subbands. In the enhanced view of Fig. 2.1 the two subbands with the lowest energies are shown. With low enough electron densities n (typically from $2 \times 10^{11}/\mathrm{cm}^2$ to $2 \times 10^{12}/\mathrm{cm}^2$) and low temperatures $T \lesssim 4\,\mathrm{K}$, only the lowest subband is populated and its density of states is a constant. The electron density then gives the Fermi wavenumber, velocity and wavelength as

$$\begin{aligned} k_\mathrm{F} &= \sqrt{2\pi n}, \\ v_\mathrm{F} &= \hbar k_\mathrm{F}/m^*, \\ \lambda_\mathrm{F} &= 2\pi/k_\mathrm{F} = \sqrt{2\pi/n}. \end{aligned} \tag{2.2}$$

This means for the above mentioned densities n one gets Fermi wave lengths of $\lambda_{\mathrm{F}} \approx 20 - 60\,\mathrm{nm}$.
An important parameter of a 2DEG is the electron mobility μ, a direct measure of the momentum relaxation time τ_{m} through its definition

$$\mu = \frac{|e|\tau_{\mathrm{m}}}{m^*}. \tag{2.3}$$

It gives a rate of scattering for ballistical transport and together with the electron density the mean free path

$$l_{\mathrm{m}} = v_{\mathrm{F}}\tau_{\mathrm{m}} = \frac{\hbar\mu}{|e|}\sqrt{2\pi n}. \tag{2.4}$$

The relaxation time τ_{m}, the mobility μ and the mean free path l_{m} deal with any scattering event that changes the momentum of an electron. Typically this can be scattering at crystal impurities, with phonons, photons or between electrons.
In interference experiments as in this work another length scale is more important, the phase relaxation length

$$l_\varphi = v_{\mathrm{F}}\tau_\varphi \quad \text{for} \quad \tau_\varphi \geq \tau_{\mathrm{m}}. \tag{2.5}$$

Here, τ_φ is the phase relaxation time and the assumption $\tau_\varphi \geq \tau_{\mathrm{m}}$ is true for high mobility 2DEGs. It is not possible to provide a (semi)classical picture for this, as for the quantities before, because here we deal with the wave nature of a quantum mechanical particle. It is better to approach this by considering which processes randomize the phase information of an electron along a path L, compared to another possible path L' with which it could interfere, in a thought experiment. Static scatterers, as impurities without any internal degree of freedom, will limit the mean free path, but change the phase only in a defined and, over time, constant way, resulting in a fixed phase relation between the two possible paths. Processes that lead to a randomly fluctuating variation of the phase will cause an averaging of constructive and destructive interference with time. This can be for example scattering off high frequency phonons. In contrast, phonons with lower frequency might affect both possible electron paths in the same way. The most important source for phase relaxation is electron-electron scattering, especially at very low temperatures when phonons are frozen out.However, this occurs only, if there is open phase space into which the electrons can scatter, i.e. non-zero excess energies $\Delta = E - E_{\mathrm{F}}$ due to finite temperature T or applied voltage V are required. For a 2DEG the phase relaxation time is given by:

$$\frac{\hbar}{\tau_\varphi} \sim \frac{\Delta^2}{E_{\mathrm{F}}}\left[\ln\left(\frac{E_{\mathrm{F}}}{\Delta}\right) + constant\right]. \tag{2.6}$$

This differs for conductors with other dimensionalities. In this thesis the reduction of l_φ, i.e., the dephasing will be a major topic for the studied Mach-Zehnder interferometer.

2.2. The quantum Hall effect - Quantized Landau levels

Discovered in 1980 in the group of Klaus von Klitzing, the quantum Hall effect had a major impact on the community of mesoscopic physics [25]. The von Klitzing constant is measured to be $R_{\mathrm{K}} = h/e^2 = 25812.8074434\,\Omega$ and is now even a standard of resistance with the definition $R_{\text{K-90}} = 25812.807\,\Omega$, with a standard deviation of only 0.0000084. This quantum phenomenon can be observed in millimeter sized samples and thus reaches even into the macroscopic world. The transport in the quantum Hall regime is as perfectly ballistic as can be and displays mean free path values of a millimeter. However, one has to remember the difference of mean free path l_{m} and phase relaxation length l_φ. The latter will be a central topic of chapters 5 and 6.
We start with the Schrödinger equation for electrons in the subband E_{s} of a 2DEG with the effective mass m^*, without any confinement potential, but including a magnetic field B in z-direction:

$$\left[E_{\mathrm{s}} + \frac{p_y^2}{2m^*} + \frac{(eBy + \hbar k_x)^2}{2m^*}\right]\chi(y) = E\chi(y) \tag{2.7}$$

This can be rewritten in the form

$$\left[E_{\mathrm{s}} + \frac{p_y^2}{2m^*} + \frac{1}{2}m^*\omega_{\mathrm{c}}\left(y + y_k\right)^2\right]\chi(y) = E\chi(y) \tag{2.8}$$

$$\text{with} \qquad y_k \equiv \frac{\hbar k}{eB} \quad \text{and} \quad \omega_{\mathrm{c}} \equiv \frac{eB}{m^*}, \tag{2.9}$$

which is essentially a one-dimensional Schrödinger equation of a parabolic potential with eigenfrequency of the cyclotron frequency ω_{c} centered at $-y_k$. Thus one easily finds the corresponding eigenenergies of

$$E(i) = E_{\mathrm{s}} + \left(i + \frac{1}{2}\right)\hbar\omega_{\mathrm{c}}, \qquad i = 0, 1, 2, ... \tag{2.10}$$

We end up with quantized energy levels, the so called Landau levels, equally spaced by $\Delta E = \hbar\omega_{\mathrm{c}}$.
Physically this quantization can be visualized by thinking of the classical motion of electrons in an external magnetic field. Electrons move on circular orbits which are shrinking with increasing magnetic field. These orbits have to be quantized, since the phase of the electron wave function has to change by integer multiples of 2π along one cycle. This defines the discrete energy levels of Eq. 2.10.
The resulting density of states is no longer a constant with the lower cut off energy E_{s}

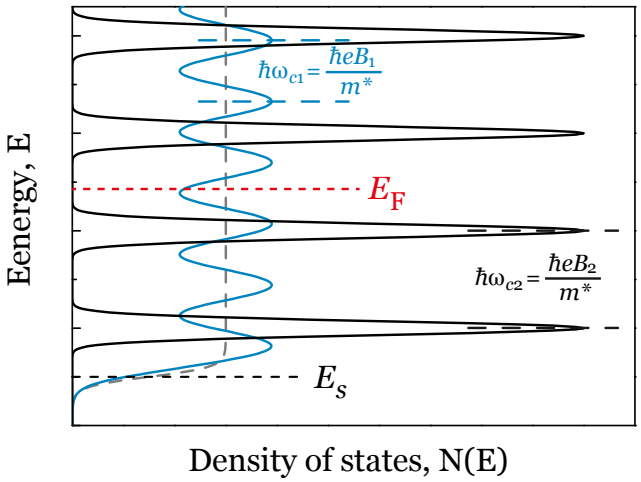

Figure 2.2.: Density of states in the bulk of a 2DEG for various magnetic fields. The dashed gray line describes the constant DOS at $B = 0$, the dark cyan line is for intermediate fields, where Landau levels start to develop. The black line is for magnetic fields deep in the quantum Hall regime when Landau levels are discrete and well separated.

as in Eq. 2.1, but contains peaks (delta functions broadened by scattering) originating from $E(n)$

$$N(E,B) \approx \frac{(2)eB}{h} \sum_{i=0}^{\infty} \delta \left[E - E_s + \left(i + \frac{1}{2} \right) \hbar\omega_c \right]. \tag{2.11}$$

The number 2 in brackets represents the possible spin degeneracy, only required for small magnetic fields. At larger fields the degeneracy is lifted due to Zeeman splitting and we do not need this factor. From Eq. 2.11 we can determine for a given electron density n and magnetic field B the number of occupied Landau states, the so called filling factor[1]

$$ff = \frac{nh}{eB}. \tag{2.12}$$

Eq. 2.11 desplays that with increasing field B the Landau levels are pushed to larger energies above E_F and fewer levels are occupied (see Fig. 2.2), while more and more electron states fit into each level(see 2.9, for constant Δk electron states require less real space Δy_k with increasing field B).

[1]Different from most literature I do not use the sign ν for the filling factor but *ff*, because it is also common to use ν for the visibility which will be introduced later and is the main parameter for the Mach-Zehnder interferometer which we will study.

Usually the filling factor is treated as an integer number, since we have a series of discrete states which can be either filled or not. This is true for many cases, but concerning the exact transport properties (see section 2.3.2) and the interference (see chapter 5) in the quantum Hall regime it is important to know exactly where the Fermi energy lies between consecutive or inside Landau levels.
With this single particle Landau quantization we will explain the transport in the integer quantum Hall effect (IQHE) in the following section. Increasing the magnetic field beyond $ff = 1$ one would arrive in the regime dominated by the fractional quantum Hall effect (FQHE), where a new many-body ground state forms and electrons combined with magnetic flux build new quasi-particles. All measurements within this thesis have been performed at filling factors $2 > ff > 1$ and effects of Landau levels with fractional filling factors $ff = 5/3$ and $4/3$ are not observed, so a detailed treatment of the FQHE is not required here.

2.3. Transport in the quantum Hall regime

2.3.1. Quantum Hall edge states and Landauer-Büttiker formalism

As seen above, available states for transport in the quantum Hall regime exist only when a Landau level is aligned with the Fermi energy. However, this is only true in the bulk of the sample. The spatial confinement potential of a sample with finite size leads to a bending of the Landau levels upwards as shown in Fig. 2.3(a). Even if the Fermi energy lies between two Landau levels, electron states at the sample edge are present, which turn out to be one dimensional almost perfect ballistic conductors. These so called edge channels have a unique property: via Eq. 2.9 the confinement potential $U(y)$ enters the dispersion relation

$$E(i,k) \approx E_\mathrm{s} + (i + 1/2)\,\hbar\omega_\mathrm{c} + U(y_k). \tag{2.13}$$

Thus, electrons in the $+k$ state, moving from left to right in Fig. 2.3(b), are located at the lower edge of the sample, whereas the $-k$ states moving in the opposite direction are at the upper edge.[2] Thus the transport channels from left to right are separated from the ones from right to left. If the sample is wide enough, starting from a few microns, there is only negligible overlap between states at adjacent edges and no backscattering is possible. The property, that different transport channels are separated and the electrons move only along the sample edge in a certain orientation is called chiral. This makes the edge channels (almost) ideal ballistic transport channels.

[2] Calculating the velocity from Eq. 2.13: $v(i,k) = \frac{1}{\hbar}\frac{\partial E(i,k)}{\partial k} = \frac{1}{\hbar}\frac{\partial U(y_k)}{\partial k} = \frac{1}{\hbar}\frac{\partial U(y)}{\partial y}\frac{\partial y_k}{\partial k} = \frac{1}{eB}\frac{\partial U(y)}{\partial y}$. The last factor, $\partial U(y)/\partial y$, changes sign for opposite sides of the sample.

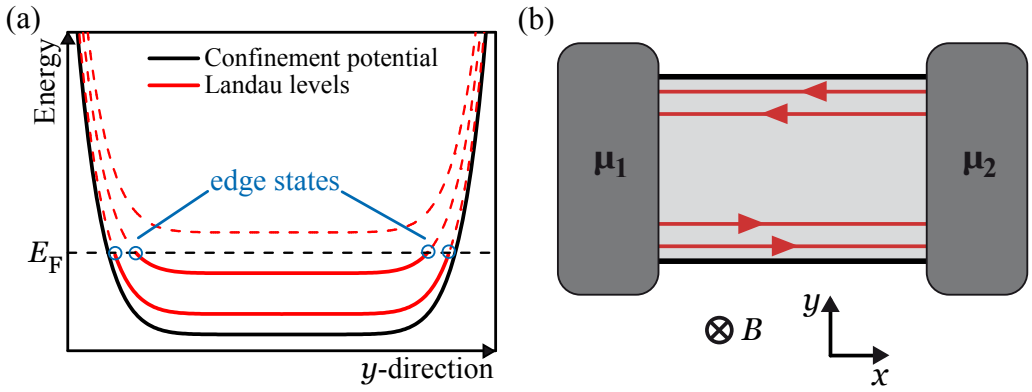

Figure 2.3.: Edge states develop due to the confinement potential of the sample. (a) The Landau levels in a cross section along the y-direction. In the center of the sample we find the described discrete Landau levels (red straight lines indicate filled states, dashed lines empty states) and no states at the Fermi energy, which is located between two levels. At the sample edges the Landau levels follow the bending of the confinement potential and intersect the Fermi energy at certain positions close to the edge, forming so-called edge states. Only these states contribute to transport when no Landau level is aligned to the Fermi energy in the bulk of the sample. Due to their bending the edge states are chiral, as seen in (b) in top view.

The Landauer-Bü ttiker formalism provides a very descriptive explanation how these transport channels lead to the quantized Hall resistance $\rho_{xy} = \frac{V_H}{I}$ and the Shubnikov-de Haas oscillations in the longitudinal resistance $\rho_{xx} = \frac{V_x}{I}\frac{\text{width}}{\text{length}}$ as shown in Fig. 2.4.
The Landauer-Büttiker formalism is appropriate for mesoscopic conductors with a finite number of modes (i.e. ballistic transport channels) and reflectionless contacts. A conduction mode itself has no resistance, but due to a recombination of electron states from infinite modes in a lead to a single mode in the mesoscopic conductor a contact resistance arises, independent of contact geometry or dispersion relation $E(k)$ of the transport mode. This contact resistance is the von Klitzing constant $R_K = h/e^2 \approx 25.8\,\text{k}\Omega$. These considerations lead to the Landauer formula

$$G = \frac{e^2}{h} M\mathcal{T}, \tag{2.14}$$

where M denotes the number of available transport modes and $\mathcal{T}$ the average probability that an electron injected at one end of the conductor will be transmitted to the other end. This leads to a current through the sample of

$$I = \frac{e}{h} M\mathcal{T}\left[\mu_L - \mu_R\right] = \frac{e^2}{h} M\mathcal{T}\left[V_L - V_R\right], \tag{2.15}$$

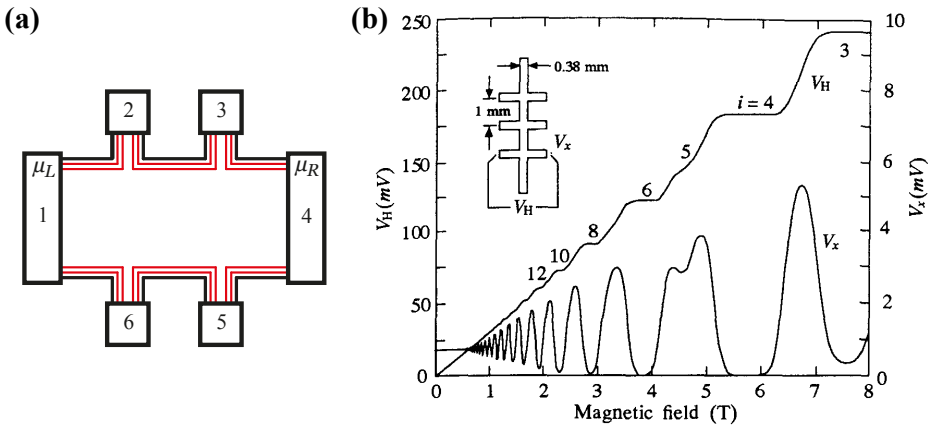

Figure 2.4.: (a) A sketch of a typical Hall bar with numbered contacts at $ff = 2$. Red lines represent the two edge channels. A constant current I flows between contacts 1 and 4 due to the potential difference $\Delta\mu = \mu_L - \mu_R$. Longitudinal voltage V_x is measured between contacts 2 - 3 or 5 - 6, Hall voltage V_{H}, e.g., between 2 - 6. (b) A measurement of Hall and longitudinal voltages vs. magnetic field. The Hall voltage V_{H} displays plateaus at fractions of $R_{\mathrm{K}}I$, while the longitudinal voltage V_x shows minima at plateaus and maxima in between.

assuming $M(E) = const.$ and $\mathcal{T}(E) = const.$ in the energy window $\mu_L - \mu_R$. This two terminal formula was extended for multiple terminals by Büttiker simply by summing over all the terminals q that lead to a current into p

$$I_p = \frac{e}{h} \sum_q \left[\bar{\mathcal{T}}_{q \leftarrow p} \mu_p - \bar{\mathcal{T}}_{p \leftarrow q} \mu_q \right], \tag{2.16}$$

where the transmission function $\bar{\mathcal{T}}_{p \leftarrow q}$ is the average transmission from terminal p into terminal q. Defining

$$G_{pq} \equiv \frac{e^2}{h} \bar{\mathcal{T}}_{p \leftarrow q}, \tag{2.17}$$

satisfying the *sum rule* $\sum_q G_{qp} = \sum_p G_{pq}$ one can rewrite 2.16 as

$$I_p = \sum_q G_{pq} \left[V_p - V_q \right]. \tag{2.18}$$

This set of equations gives the possibility to inspect the conductance in a typical Hall bar as shown in Fig. 2.4(a). Assuming a number of edge channels M (here $M = 2$) and no backscattering, i.e. perfect ballistic transport, the transmission function $\bar{\mathcal{T}}_{pq}$ is easy to evaluate. One has to take into account the number of present edge channels M and

since electrons travel from one terminal along the edge without disturbance to the next, it follows that $\bar{\mathcal{T}}_{pq} = M$. Then one can write

$$\begin{Bmatrix} I_1 \\ I_2 \\ I_3 \\ I_4 \\ I_5 \\ I_6 \end{Bmatrix} = \begin{bmatrix} G_\mathrm{C} & 0 & 0 & 0 & 0 & -G_\mathrm{C} \\ -G_\mathrm{C} & G_\mathrm{C} & 0 & 0 & 0 & 0 \\ 0 & -G_\mathrm{C} & G_\mathrm{C} & 0 & 0 & 0 \\ 0 & 0 & -G_\mathrm{C} & G_\mathrm{C} & 0 & 0 \\ 0 & 0 & 0 & -G_\mathrm{C} & G_\mathrm{C} & 0 \\ 0 & 0 & 0 & 0 & -G_\mathrm{C} & G_\mathrm{C} \end{bmatrix} \begin{Bmatrix} V_1 \\ V_2 \\ V_3 \\ V_4 \\ V_5 \\ V_6 \end{Bmatrix} \tag{2.19}$$

with the contact, or two terminal conductance

$$G_\mathrm{C} = \frac{e^2 M}{h}. \tag{2.20}$$

What one can see here is that the current I_q through a terminal q is usually a sum of the current that "leaves" the terminal due to its own potential V_q and the current that flows into it from the precedent terminal p and its voltage V_p.
Eq. 2.19 can be simplified a lot. We can set the potential of one terminal to be zero, e.g. $V_4 = 0$. Also, we want the current to flow from terminal 1 to 4 and the remaining terminals to be voltage probes, thus $I_2 = I_3 = I_5 = I_6 = 0$. Electrons entering the edge channels from terminals 1 or 4 will retain their energy μ_L (μ_R) due to the perfect ballistic transport in the edge channel and thus carry on their voltage μ_L/e (μ_R/e) until the next current carrying terminal which is not floating (as the voltage probes are) where they experience the contact resistance. This is exactly what one would assume for a ballistic conductor, as the edge channels. And what turns out to be the case only taking zero current for voltage probes into account. This leads to

$$V_2 = V_3 = V_1, \quad V_5 = V_6 = V_4 = 0. \tag{2.21}$$

We see that the current going from terminals 1 to 4 is limited by the contact resistance

$$I_1 = G_\mathrm{C} V_1, \tag{2.22}$$

and that the conductance is just the sum over all the channels M, each contributing a conductance quantum $g_0 = \frac{e^2}{h}$.
Fig. 2.4(b) shows a typical Hall measurement of the Hall voltage V_H and the longitudinal voltage V_x for a 2DEG in a GaAs/AlGaAs heterostructure. Below 0.5 T we see the classical behavior of constant longitudinal voltage (a constant current I is flowing), and linear Hall voltage. At increasing magnetic fields the Hall voltage develops into a series of steps and the longitudinal voltage shows oscillations. These oscillations are called Shubnikov-de Haas oscillations. With magnetic field the density of states splits up into Landau levels which are shifted with the field. When the Fermi energy lies between

two Landau levels, transport through the sample is only carried by edge channels, as analyzed above. Then the longitudinal resistance is

$$R_{\mathrm{L}} = \frac{V_x}{I_1} = \frac{V_2 - V_3}{I_1} = \frac{V_6 - V_5}{I_1} = 0, \tag{2.23}$$

because the voltage difference at two adjacent probes is zero, both being at the same potential V_1 or V_4. The according Hall resistance is then

$$R_{\mathrm{H}} = \frac{V_{\mathrm{H}}}{I_1} = \frac{V_2 - V_6}{I_1} = \frac{V_3 - V_5}{I_1} = G_{\mathrm{C}}^{-1}, \tag{2.24}$$

which is just the two terminal resistance. This is simple to see, since the upper half of the voltage probes float on the voltage of one current terminal and the lower ones on the other current terminal, so the Hall voltage drop is the one at the terminals of the current leads. The two terminal conductance is a multiple of the conductance quantum. The multiplier is the number of modes M, which in the quantum Hall regime is the number of edge channels which is of course identical with the filling factor ff. With this we can rewrite Eq. 2.24 obtaining the known formula of the quantum Hall resistance

$$R_{\mathrm{H}} = \frac{1}{ff}\,\frac{h}{e^2} = \frac{1}{ff}\,R_{\mathrm{K}}, \tag{2.25}$$

with the von Klitzing constant R_{K}.
This situation corresponds to a minimum in the Shubnikov-de Haas oscillations as seen in Eq. 2.23 and a plateau of the Hall voltage/resistance. When the magnetic field increases further, a Landau level crosses eventually the Fermi energy. The edge channels of the lower levels remain, but because one level is aligned with the Fermi energy there are electron states in the bulk of the sample which are classically resistive and not ballistic like the edge channels. This bulk resistivity appears as a maximum in the longitudinal resistance and as a step in Hall resistance from $ff = i$ to $ff = i - 1$. When the Landau level is completely pushed above the Fermi energy one sees again a minimum of the longitudinal resistance and the next plateau of the Hall resistance.
The conductance is entirely dependent on the number of present edge channels, which is an integer number. At a Hall plateau the two terminal conductance is simply an integer multiple of the conductance quantum due to the approximately one dimensional character of the edge channel. For many observations this simple view is enough, but for an exact description of the quantum Hall edge one needs to go beyond that.

2.3.2. Compressible and incompressible strips

So far the quantum Hall edge was treated as shown in Fig. 2.5(a)-(c). The confinement potential bends the Landau levels up across the Fermi energy, the one dimensional edge

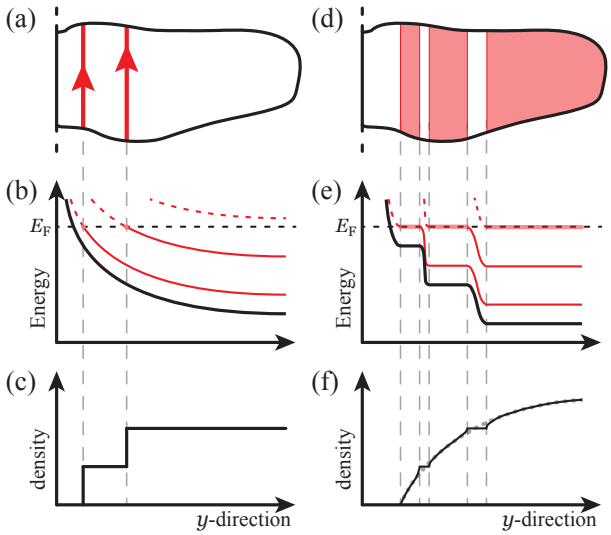

Figure 2.5.: Reconstruction of quantum Hall edge: (a) A top view sketch of a sample edge in the IQHE regime at $ff \geq 2$ with edge channels (thick red lines) similar to Fig. 2.3(b). (b) The according confinement potential (black line) and Landau levels (straight red lines: occupied; dashed: empty) as in Fig. 2.3(a) and (c) the electron density, i.e., the local filling factor close to the edge, which changes step like. (d)-(f) The corresponding diagrams for the self-consistently reconstructed QH edge. (d) The sample edge becomes a series of compressible (pale red) and incompressible strips (white), along which the Landau levels (e) adjust themselves step like (thick pale red line when locked to the Fermi energy) and the density (filling factor) becomes a smooth function in compressible strips and develops plateaus in the incompressible strips.

channels are formed and the local filling factor, i.e. electron density, changes steplike from the bulk filling factor in the inside of the sample towards zero at the edge with each Landau level leaving the sample at a specific point in the y-direction. At a position, where there are no electron states at the Fermi surface, electrons are localized due to the Landau quantization of the magnetic field. This implies that the electron density cannot vary as in the metallic case, even when an electric potential is applied. Thus, no metallic screening. This is called *incompressible* electron gas. In contrast, at zero magnetic field, or when a Landau level is aligned with the Fermi surface, the electron gas is called *compressible*, because the electrons can move and act metallic and show very good screening.

Striclty speaking, it is not appropriate to treat the quantum Hall edge by only regarding bending of the Landau levels with the underlying confinement potential. In fact, one has to consider the (smoothly) decreasing local electron density $n(y)$ towards the sample edge at zero magnetic field, which can be either due to the electric potential of

surface states at an etched edge or the potential of a depleting top gate. This situation at $B = 0$, in addition to the discrete Landau level peaks in the density of states at large magneitc fiels, leads to a fragmentation of the electron gas into compressible and incompressible spatial regions [26]. By considering an electrostatic potential $\Phi(y)$ in the plane of the 2DEG close to a depleted region one can solve Poisson's equation $\frac{d\Phi}{dy} = \frac{4\pi e n(y)}{\varepsilon}$ and arrives at a local charge density profile for $B = 0$ depicted by the dotted gray line in Fig. 2.5(f). The potential can be calculated self-consistently with a Thomas-Fermi-Poisson approximation [27]. A high perpendicular magnetic field then leads to a redistribution of charges due to the strongly nonlinear low-temperature screening properties of the Landau quantization. Thus, $n(y)$ neither decreases smoothly towards the edge, as it would if it were purely compressible, nor step-like as in the picture of edge channels with incompressible regions with only integer filling factors in between. It splits into alternating regions (strips) along the edge [see Fig. 2.5(d)-(f)]. In the so called incompressible strips the electron density is constant, with fixed integer filling factor; the potential shows a jump; there are no states at the Fermi surface and screening is not possible. In the compressible strips the electron density varies smoothly, the filling factor is fractional, a Landau level is pinned at the Fermi energy and the strip shows metallic screening.
The ballistic transport happens in the incompressible strips and leads to the Hall plateaus of the Hall resistance and the zero longitudinal resistance, while the compressible strips are responsible for how the Hall resistance increases between plateaus and how high the longitudinal resistance peaks at half filling factors are [27].
The width of the incompressible strips depends on the magnetic field. With increasing field they become more narrow and are pushed more closely to the edge. When the width of an incompressible strip falls below λ_{F} eventually it collapses [27]. The ballistic transport of the collapsed channels is then carried by the remaining incompressible strip. This behavior was nicely illustrated in Ref. [28] and Ref. [29].

2.3.3. Luttinger liquid in the QH regime at filling factor 2

Here I will give an overview of electron transport in one dimension, i.e., the Luttinger liquid, following Ref. [30] and for the special case of the integer quantum Hall effect at $ff = 2$ Ref. [31] and [32].
We have seen that the electrons in the edge states in the incompressible strips are confined to one dimension. Now let's see what this means for their properties, especially their transport properties. In higher dimensions (2 and more) the Fermi liquid theory accounts for almost everything. Free electrons can be nicely described by it and even if there is interaction between them the basic theory stays the same. The surrounding electron sea can be treated as a mean field and each electron is dressed with density fluctuations (particle-hole excitations of the ground state) and together can be treated

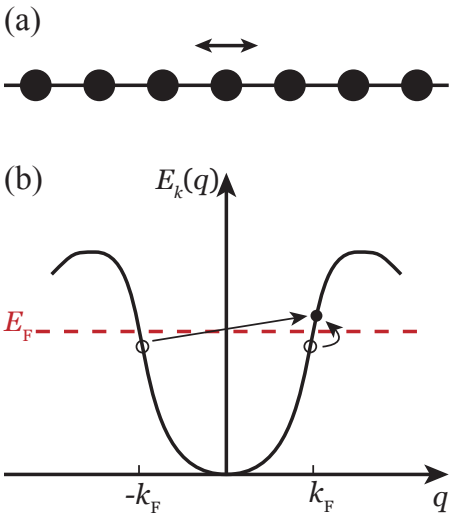

Figure 2.6.: (a) Sketch of a one-dimensional chain/lattice. Due to the 1D character a single particle cannot move freely by itself, only a collective motion is possible. (b) Dispersion relation in 1D, shows that excitations close to the Fermi energy are either part of the nesting problem ($\Delta k = 2k_F$) or are 0 and have defined wave vectors q.

as quasiparticles, which are again free fermions of a Fermi liquid. Apart from these individual excitations there are also collective excitations, known as plasmons, which can be excited for example with light pulses in a metal surface. However, this is rather an exception.
In 1D the situation is completely different: here particles are arranged like pearls on a rope. One sees immediately that no individual movement is possible [see Fig. 2.6(a)] and collective excitations are the only means for transport. The 1D Fermi "surface", which consists of only two points [Fig. 2.6(b)], leads on one hand to the problem, that nesting[3] is not just an exception, but a rule, and on the other hand to a special peculiarity: electron-hole excitations close to the Fermi energy have, unlike in the case of higher dimensions, a well defined momentum q of either $k \sim 0$ or $k \sim 2k_\mathrm{F}$ and energy $E(k) = v_\mathrm{F}k$ and can thus be viewed as defined particles which are then bosons, since they involve two fermions, i.e., the destruction of one and the creation of another.
In the following I want to go more into detail how this 'bosonization' works. We start with a chain of particles whose local density operator can be written as a series of delta

[3]We speak of a nesting property of a system, when there exists a wave vector Q such that for a domain of values in k-space the energy relative to the chemical potential $\xi(k) = \varepsilon(k) - \mu$ satisfies $\xi(k + Q) = -\xi(k)$. This can lead to a singularity over which one cannot integrate when calculating the susceptibility $\chi(k)$.

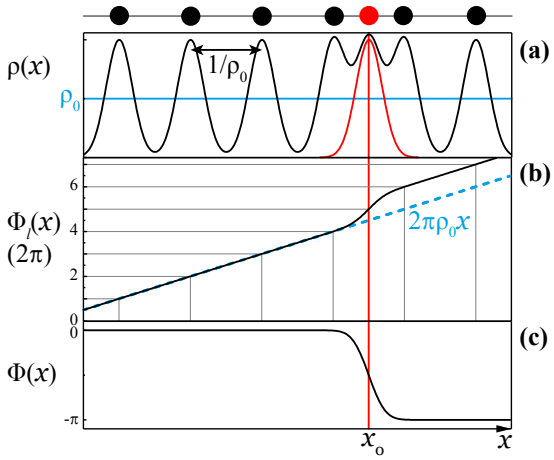

Figure 2.7.: Bosonization of a 1D lattice of particles at x_i (black circles, top) and an additional particle at the position x_0 (red circle). (a) The oscillating density with maxima at particle positions x_i. The blue line is the average density ρ_0, disregarding the additional peak at x_0. In (b) the counting field Φ_l is depicted, which increases by 2π each time when crossing a particle at x_i. The blue dashed line represents the perfect crystalline solution. Φ_l shows a deviation from this line at x_0 resulting in a jump of $-\pi$ in the field Φ in (c).

peaks

$$\rho(x) = \sum_i \delta(x - x_i), \tag{2.26}$$

with x_i being the position of the ith particle. The average density is ρ_0 and the mean distance between the particles $d = 1/\rho_0$ is also the distance between their equilibrium positions. Since in 1D a particle is defined by its number i one can introduce a labelling field $\Phi_l(x)$, which is defined by $\Phi_l(x_i) = 2\pi i$. This means one goes in x from left to right and each time one comes across a particle, 2π is added to Φ_l. For a perfect 1D lattice this is just $\Phi_l(x) = 2\pi\rho_0 x$. With this labelling field, the density operator 2.26 can be rewritten as

$$\rho(x) = \sum_p \frac{\nabla\Phi_l(x)}{2\pi}\delta(\Phi_l(x) - 2\pi p). \tag{2.27}$$

For convenience we write the labelling field in terms of another field $\Phi(x)$, which is the deviation of $\Phi_l(x)$ from the equilibrium

$$\Phi_l(x) = 2\pi\rho_0 x - 2\Phi(x). \tag{2.28}$$

Putting this into Eq. 2.27 and using Poisson's summation formula we arrive at

$$\rho(x) = \left[\rho_0 - \frac{1}{\pi}\nabla\Phi(x)\right] \sum_p \exp\left[i2p(\pi\rho_0 x - \Phi(x))\right]. \tag{2.29}$$

A particle-creation operator can be written in the form

$$\psi^\dagger(x) = [\rho(x)]^{1/2}\, e^{-i\theta(x)} \tag{2.30}$$

where $\theta(x)$ is another field. For fermions this looks like

$$\psi_F^\dagger(x) = \left[\rho_0 - \frac{1}{\pi}\nabla\Phi(x)\right]^{1/2} \sum_p e^{i(2p+1)(\pi\rho_0 x - \Phi(x))} e^{-i\theta(x)}. \tag{2.31}$$

This enables us to describe the electronic (fermionic) system in terms of the boson fields $\Phi(x)$ and $\theta(x)$ and theoretically they can be treated with boson creation and annihilation operators $b^\dagger$ and b. Now after having introduced these fields we can check what they actually do in a physical picture.
As one can easily see in Eq. 2.30 the field $\theta(x)$ can be seen as the phase of a particle, analogous to the superconducting phase of a BCS wave function. However, in this work this field is of little interest. The field $\Phi(x)$ is much more important; it defines the local density (Eq. 2.29) and introduces a phase to a particle by itself (Eq. 2.31). With the help of Fig. 2.7 and two special cases I want to illustrate the meaning of Φ. If we take a constant Φ (and this might be as well 0) we see in Eq. 2.28 that one ends up in the case of a perfect lattice. The density Eq. 2.29 becomes

$$\rho(x) \propto \rho_0 \cos(2k_F x - 2\Phi) \tag{2.32}$$

with the maxima (the individual charges) are separated by $d = 1/\rho_0$. The second case is the long wavelength solution, when we average over distances large compared to the interparticle distance d. Then the density becomes

$$\rho_{long}(x) \cong \rho_o - \frac{1}{\pi}\nabla\Phi(x) \tag{2.33}$$

and we see that a gradient in Φ adds or removes particles. A jump by $-\pi$ of Φ at a certain position x_0 means an addition of exactly one particle at this point. Or in other words, and maybe even better, the jump in Φ of $-\pi$ represents a density fluctuation (increase) of the order of one charge more than the average charge density. Now let's imagine that this jump of Φ moves from right to left, the density excitation (plasmon) propagates and in the end we have changed Φ by π and transferred one particle from one side to the other. This can be verified if we put Eq. 2.33 into the continuity equation $\partial\rho/\partial t + \nabla j = 0$. Then we arrive at $j = \partial_t\Phi/\pi$ for the current. Also with Eq. 2.32 we can make the same conclusion, a change of Φ by π can be seen as a movement of the particles by a distance $1/\rho_0$ and a particle transfered from right to left. This shows in a simplified picture how the bosonic fields can describe transport.
Dealing with electrons/fermions we must take into account not only the charge, but also the spin. For this one can just define two fields Φ, one for the charges Φ_ρ and another

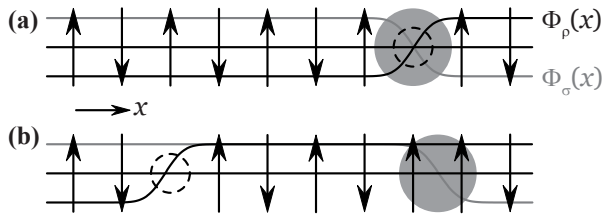

Figure 2.8.: Chain of particles with spin up and down with antiferromagnetic coupling and the annihilation of one particle (a), resulting in independently moving kink in Φ_ρ (dashed circle) and Φ_σ (gray circle) (b). Black and gray lines are charge boson field Φ_ρ and spin boson field Φ_σ respectively.

for the spins Φ_σ. In Fig. 2.8 one can see that Φ_ρ and Φ_σ are decoupled. Removing, e.g., one particle leads to a kink in both Φ_ρ and Φ_σ [see Fig. 2.8(a)]. When this hole is propagating as in Fig. 2.8(b) we see at one point a charge is missing (smooth Φ_σ, but kink in Φ_ρ) and at another one pair of frustrated spins (smooth Φ_ρ, but kink in Φ_σ). This can happen because in 1D separating Φ_σ from Φ_ρ does not lead to an increased number of frustrated spins as in higher dimensions.

With this basic knowledge of electrons in one dimension we can look at the system of interest, that is the transport in the quantum Hall edge states at filling factor $ff = 2$, where two chiral one-dimensional, co-propagating channels are present.
In the integer quantum Hall effect at $ff = 2$ there are two chiral channels in parallel which will interact. With the fermion operator ψ_α, α denoting the outer or inner edge channel, one can write a single-particle Hamiltonian for free chiral fermions for each channel

$$\mathcal{H}_0 = -\hbar i v_F \sum_\alpha \int dx \psi_\alpha^\dagger \partial_x \psi_\alpha. \tag{2.34}$$

With the local density $\rho_\alpha(x) = \psi_\alpha^\dagger(x)\psi_\alpha(x)$ an effective interaction Hamiltonian is

$$\mathcal{H}_{int} = (1/2) \sum_{\alpha,\beta} \iint dx dy U_{\alpha\beta}(x-y)\rho_\alpha \rho_\beta. \tag{2.35}$$

one has to note here, that $\rho_\alpha(x)$ is a local *particle* density. The kind of interaction and thus also the charge is "hidden" in the potential $U_{\alpha\beta}$.
As shown before the fermion operator can be represented in terms of fields Φ_α

$$\psi_\alpha \propto e^{i\Phi_\alpha} \tag{2.36}$$

and the density can be written as

$$\rho_\alpha(x) = (1/2\pi)\partial_x \Phi_\alpha(x). \tag{2.37}$$

Then one obtains the total Hamiltonian

$$\mathcal{H} = \mathcal{H}_0 + \mathcal{H}_{int} = \sum_{\alpha,\beta} \iint \frac{dxdy}{8\pi^2} V_{\alpha\beta}(x-y)\partial_x\Phi_\alpha(x)\partial_y\Phi_\beta(y), \tag{2.38}$$

with a shifted interaction potential

$$V_{\alpha\beta} = U_{\alpha\beta} + 2\pi\hbar v_F \delta_{\alpha\beta}\delta(x-y). \tag{2.39}$$

The second quantization of the boson field with $a^\dagger_{\alpha k}$ and $a_{\alpha k}$ leads to

$$\Phi_\alpha(x) = \varphi_\alpha + 2\pi N_\alpha \frac{x}{W} + \sum_{k>0} \sqrt{\frac{2\pi}{Wk}} \left[a_{\alpha k} e^{ikx} + a^\dagger_{\alpha k} e^{-ikx} \right], \tag{2.40}$$

with the zero modes φ_α and N_α. By comparing Eq 2.40 with Eq. 2.37 one can identify $N_\alpha = \int dx \rho_\alpha(x)$ as the total number of electrons in the channel α, and the operator $\exp(-i\varphi_\alpha)$ increases this number by one. The third term in Eq. 2.40 is the sum over plasmonic high frequency density fluctuations. W is the size of the system where one can take in the end the thermodynamic limit of $W \to \infty$. And with this the Hamiltonian looks like

$$\mathcal{H} = (1/2\pi) \sum_{\alpha,\beta,k} k V_{\alpha\beta}(k) a^\dagger_\alpha(k) a_\beta(k) + \hbar \frac{1}{2W} \sum_{\alpha,\beta} V_{\alpha\beta}(0) N_\alpha N_\beta. \tag{2.41}$$

With the ground state energy $E_0 = (1/2W) \sum_{\alpha,\beta} V_{\alpha\beta}(0) N_\alpha N_\beta$ one can use the electrostatic relation for the potential $\Delta\mu_\alpha$:

$$\Delta\mu_\alpha = (1/W)\delta E_0/\delta N_\alpha = (1/W) \sum_\beta V_{\alpha\beta}(0) N_\beta. \tag{2.42}$$

So the number of excess electrons N_α is produced by the bias $\Delta\mu_\alpha$, as one in general expects. The time evolution of the zero modes is given by:

$$N_\alpha(t) = W \sum_\beta V^{-1}_{\alpha\beta}(0) \Delta\mu_\beta, \quad \varphi_\alpha(t) = \frac{-\Delta\mu_\alpha t}{\hbar}. \tag{2.43}$$

Let's look at the interaction $V_{\alpha\beta}$ in detail. The obvious kind of interaction is a via the long-range Coulomb potential. It has a logarithmic dispersion $V_{\alpha\beta}(k) \propto \log(ka)$ and a is the smallest important length scale, which is the interchannel distance, i.e., the width of the compressible strip between the incompressible ones. Further we can assume a distance D_s at which the interaction is screened and $D_s \gg a$, so the interaction is still strong at relevant distances a. Then for low energies one can neglect the logarithmic

dispersion and write $V_{\alpha\beta}(x-y) = V_{\alpha\beta}\delta(x-y)$, so that $V_{\alpha\beta}(k) = V_{\alpha\beta}(0) = V_{\alpha\beta}$. The interaction matrix can be parametrized

$$V_{\alpha\beta} = \hbar\pi \begin{pmatrix} u+v & u-v \\ u-v & u+v \end{pmatrix}, \tag{2.44}$$

with

$$u/v = \log(D_s/a) \gg 1 \tag{2.45}$$

being a new large parameter as a consequence of the long range Coulomb interaction. Diagonalization of the interaction, $V = S^\dagger \Lambda S$, leads to

$$\Lambda = 2\pi\hbar \begin{pmatrix} u & 0 \\ 0 & v \end{pmatrix}, \quad S = \frac{1}{\sqrt{2}} \begin{pmatrix} 1 & 1 \\ 1 & -1 \end{pmatrix}. \tag{2.46}$$

This is an important result, it shows that the Coulomb interaction leads to a separation of the plasmon spectrum into a fast (charge) mode $|u\rangle$ with speed u and a slow (dipole) mode $|v\rangle$ with speed v. As a remark I have to point out, that these modes represent high frequency charge *density* oscillations, rather, than electrons that carry the net current from one end to the other. The phrase *charge* mode is chosen, because it is the in-phase oscillation, thus when looking at the two edge channels at a certain point x, we will see charge q locally in both channels, while the total number of charges is given by the zero mode N_α. In contrast, for the out-of-phase *dipole* mode, we will see at each point x a local charge q in one channel and $-q$ in the other, as in a dipole.

With a new boson operator $a_\alpha(k) = \sum_\beta S_{\alpha\beta} b_\beta(k)$ one can partially diagonalize the Hamiltonian for the quantum Hall edge:

$$\mathcal{H} = \hbar \sum_k \left[uk b_1^\dagger(k) b_1(k) + vk b_2^\dagger(k) b_2(k) \right] + (1/2W) \sum_{\alpha,\beta} V_{\alpha\beta} N_\alpha N_\beta. \tag{2.47}$$

The second sum is responsible for the ground state and the bias depending zero modes as already discussed. The first sum is the diagonalized boson field with the new operators $b_\alpha^\dagger$ and b_α for creation and annihilation of the charge mode ($\alpha = 1$) and dipole mode ($\alpha = 2$).

The Hamiltonian 2.47 leads to the time evolution of the plasmon mode operators

$$b_{1k}(t) = e^{-iukt} b_{1k} \quad ; \quad b_{2k}(t) = e^{-ivkt} b_{2k}. \tag{2.48}$$

We can learn about the evolution of a state after an injection of one additional particle in the outer channel after time t and a certain distance x by looking at the overlap

$$\langle \psi_{N+1} | \psi_{N+1}^\dagger \rangle \propto \int dt e^{\Delta\mu t/\hbar} \langle N | \psi_1(0,0) \psi_1^\dagger(x,t) | N \rangle. \tag{2.49}$$

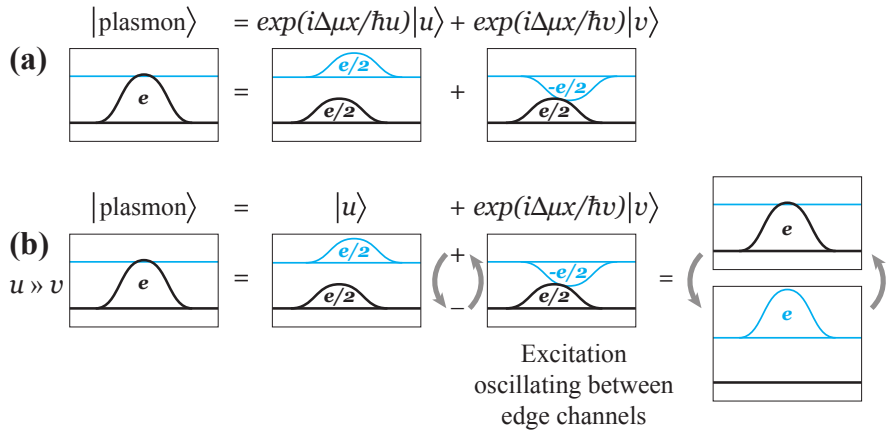

Figure 2.9.: (a) A plasmon excitation with the local charge e in one edge channel splits into two modes, a fast charge mode and a slow dipole mode. Each of them carries a dynamical phase factor depending on their velocity and traveled distance x. (b) In the limit $u \gg v$ the excitation oscillates between the edge channels with the velocity of the dipole mode.

This leads to an infinite number of terms, when written in plamon operators. However, for large x result fast oscillations, that lead to a suppression of corresponding contributions and only the terms in the sum of the charge mode $|u\rangle$ and the dipole mode $|v\rangle$ survive:

$$\langle\psi_{N+1}|\psi^\dagger_{N+1}\rangle \propto \sum C_k e^{-iKx}\delta(\Delta\mu + Ku) + \sum C_{k'} e^{-iK'x}\delta(\Delta\mu + K'u) \qquad (2.50)$$

Here, C_k and $C_{k'}$ are the plasmon correlation functions for the sets of wave numbers k_i ans k'_i, and $K = \sum_i k_i$, $K' = \sum_i k'_i$. What remains are dynamical phases from the charge and dipole mode

$$\langle\psi_{N+1}|\psi^\dagger_{N+1}\rangle \propto e^{i\Delta\mu x/\hbar u} + e^{i\Delta\mu x/\hbar v}. \qquad (2.51)$$

This is illustrated in Fig. 2.9(a). In the limit $u \gg v$, which is appropriate for $2 < ff < 1.5$, one can neglect the phase factor of the charge mode and has a situation as in Fig. 2.9(b): the sum of charge mode with a static phase and dipole mode with the dynamical phase let's the density fluctuation, i.e. the plasmon, that was originally in one edge channel, oscillate to the other and back again. However, one has to point out, that it is the plasmonic excitation, i.e. a charge density fluctiation, that is oscillating between the edge channels and not a charge. The electrons and the current stay in one edge channel. It was shown above, that the current can be written in boson fields as[4]

[4]The factor 2 represents the fact, that one deals with chiral fermions in a channel whose spin degeneracy is lifted due to the usually large magnetic field at $ff = 2$. And since the boson fields describe particle

$2\pi j_\alpha = e\partial_t \Phi_\alpha$. Then we can take the field of Eq. 2.40 together with the time evolutions in Eq. 2.43 and find that the zero mode N_α makes no contribution to the current and φ_α leads to a current of $j_\alpha = e\Delta\mu/2\pi\hbar = (e/h)eV$, which is simply the current in a 1D channel with conductance g_0 by the voltage V. The time evolution of the plasmons Eq. 2.48, which are part in the third term in Eq. 2.40, are high frequency components, that average out and do not contribute to the net current. More important is that they lead to the dynamical phases, which influence the transport property of a phase sensitive device, as for example a Mach-Zehnder interferometer.

2.4. Non-equilibrium fluctuations of a QPC

A usual measurement of a mesoscopic system deals with the conductance G or the resistance R, which refers to an average current[5] $\langle I \rangle$ of an applied voltage V (or vice versa). This carries a big part of the information one can get from the system, but it is not the whole story. The actual response of such a system to a bias voltage V is a fluctuating current $I(t)$. And also the fluctuations $\Delta I(t) = I(t) - \langle I \rangle$ carry important additional information about the system. Mathematically one can exploit probability theory and statistics to deal with such kind of random variable I in terms of a characteristic function

$$h(k) := \langle e^{ikI} \rangle. \tag{2.52}$$

If the probability distribution has a moment-generating function $M(k)$ one gets this simply by

$$M(k) := \langle e^{kI} \rangle = h(-ik) = \sum_{n=0}^{\infty} \frac{k^n}{n!} m_n \tag{2.53}$$

with the moments $m_n = \partial_k^n M(k)|_{k=0} = \langle I^n \rangle$. The cumulant-generating function then is

$$\chi(k) = \ln(h(k)) = \sum_{n=1}^{\infty} \frac{(ik)^n}{n!} \kappa_n \tag{2.54}$$

with the cumulants $\kappa_n = \partial_{ik}^n \ln(h)|_{k=0}$.

For a Gaussian distribution $\kappa_1 = m_1 = \langle I \rangle$ is the mean value μ and $\kappa_2 = m_2 - m_1^2 = \langle I^2 \rangle - \langle I \rangle^2 = \langle \Delta I^2 \rangle$ the variance σ^2, while higher order cumulants and moments are zero. Moments and cumulants are two equivalent tools to describe the probability distribution of some random variable $I(t)$.

densities which satisfy fermionic commutaion relations, but have no charge, we need to include the charge e here to have proper units. Unlike the case above where the charge is part of the interaction potential.

[5] Striclty speaking, this is $\langle I \rangle_t$ to indicate over which variable the average is taken, but out of convenience and since there is no other variable over which one could average I disregard the index t.

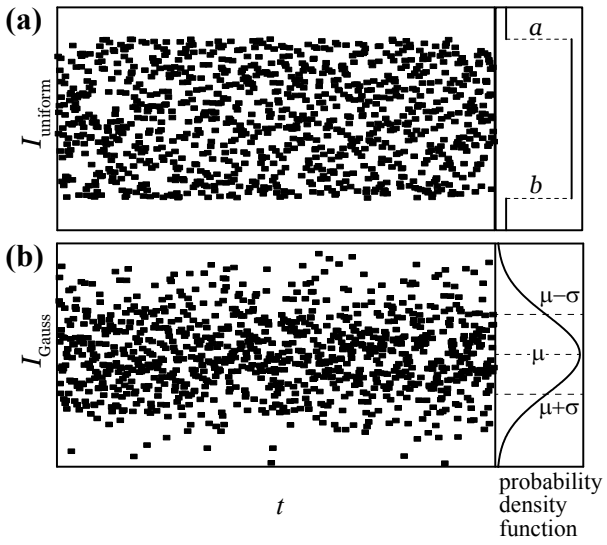

Figure 2.10.: Random variables $I(t)$ for a uniform distribution (a) and a Gaussian distribution (b) with according distribution density functions on the right. The uniform distribution has a characteristic function $h_{uni}(k) = \frac{e^{ikb}-e^{ika}}{ik(b-a)}$ and thus higher order moments and cumulants apart from mean value and variance. The Gaussian or normal distribution, with the characteristic function $h_{gauss}(k) = \exp(ik\mu - \frac{1}{2}\sigma^2k^2)$, is defined only by its mean value μ and its variance σ^2 and has no other moments.

It is only possible to measure directly the average current $\langle I \rangle$ of a mesoscopic system and the power spectral density $S_I(\omega) = 2\int_{-\infty}^{\infty} dt e^{i2\pi\omega t} \cdot C_I(t)$, which is a Fourier transform of the correlation function $C_I(t) \equiv \langle \Delta I(t+t')\Delta I(t') \rangle = \langle \Delta I^2 \rangle e^{-|t|/\tau}$(for uncorrelated events) [33]. To access higher order moments (cumulants) one needs to connect the mesoscopic system of interest to another system which is sensitive to each single event of passing electron responsible for $I(t)$. Theoretically one deals with this by the full counting statistics (FCS) [34] where the idea is to get the probabilities P_m of counting m events (passing electrons $\rightarrow$ current) over the time t with a detector that is coupled via a constant λ to the system, to get a generating function

$$\chi(\lambda) = \sum_m P_m e^{i\lambda m}. \tag{2.55}$$

In Ref. [34] a so called *spin 1/2 galvanometer* is suggested as a detector. That is a spin 1/2 next to the fluctuating current $I(t)$ precessing in the magnetic field $B(t) = \text{const.} \times I(t)$ produced by the current. So the precession angle of the spin measures the transmitted charges $eN(t) = \int_0^t dt' I(t')$. Then we can rewrite the generator 2.55 as

$$\chi(\lambda,\ t) = \langle e^{i\lambda N(t)} e^{-i\lambda N(0)} \rangle \tag{2.56}$$

and get the moments of the current $\partial_{i\lambda}^n \ln(\chi)/t = \langle I^n \rangle$ in the long-time limit [35]. Looking at an ideal single-channel conductor with a scattering potential $U(x)$ and a coupling λ to the detector we have a Schrödinger equation

$$i\hbar\frac{\partial\psi}{\partial t} = \left[\frac{\hbar^2}{2m}\left(-i\frac{\partial}{\partial x} - \frac{\lambda}{2}\delta(x)\right)^2 + U(x)\right]\psi. \tag{2.57}$$

Then we have the scattering matrix

$$S_\lambda = \begin{pmatrix} e^{i\lambda/2}A_L & B_R \\ B_L & e^{i\lambda/2}A_R \end{pmatrix}, \tag{2.58}$$

where $A_{L,R}$ and $B_{R,L}$ are transmission and reflection amplitudes and generally $|A|^2 = |A_{L,R}|^2$ and $|B|^2 = |B_{L,R}|^2$. Energy distributions $n_{L(R)}(E)$ are equilibrium Fermi functions with temperature T and chemical potentials shifted by a dc voltage $eV = \mu_L - \mu_R$. For $V = 0$ one arrives at a generating function

$$\chi(\lambda) = e^{-\lambda_*^2 f(t,T)}, \tag{2.59}$$

with $\sin(\lambda_*/2) = |A|\sin(\lambda/2)$ and $f(t,T) = \frac{1}{2\pi^2}\ln\left[\frac{\hbar}{\pi k_B T E_F}\sinh(\pi k_B T t/\hbar)\right] \propto tT + \text{const}$ for large t. Then one finds the second moment of the distribution

$$\langle \Delta I^2 \rangle = \partial_{i\lambda}^2 log(\chi)/t|_{\lambda=0} = 2|A|^2 f(t,T)/t \propto GT, \tag{2.60}$$

which agrees with the Johnson-Nyquist formula for thermal mediated equilibrium noise. More interesting is the case of finite dc bias when there is shot noise. The bias is reflected in the energy distributions $n_{L(R)}(E) = \left[\exp((E \pm \frac{1}{2}eV)/k_BT) + 1\right]^{-1}$ and one arrives at a generating function of

$$\chi(\lambda) = \exp(-tk_BTr_+r_-/h), \tag{2.61}$$

with

$$r_\pm = s \pm \cosh^{-1}\left[|A|^2\cosh(s + i\lambda) + |B|^2\cosh s\right], \tag{2.62}$$

and $s = eV/2k_BT$. In the limit $k_BT \gg eV$ one would get the equilibrium result 2.59 and for $eV \gg k_BT$ one can simplify to

$$\chi(\lambda) = \left(e^{i\lambda\text{sgn}(V)}|A|^2 + |B|^2\right)^{e|V|t/h}. \tag{2.63}$$

Plugging this into Eq. 2.55 one finds the binomial distribution with the probabilities

$$P_N(m) = \begin{pmatrix} N \\ m \end{pmatrix} p^m q^{N-m}, \tag{2.64}$$

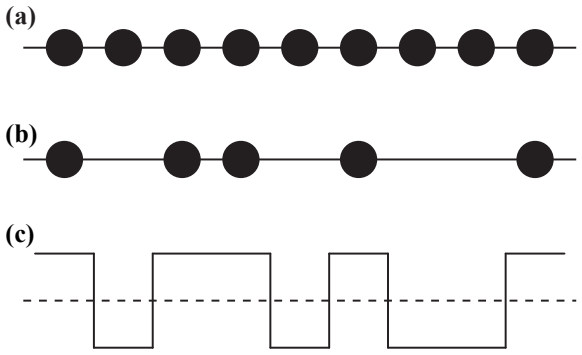

Figure 2.11.: A chain of (fermionic) particles as in Fig. 2.6. (a) A full single mode channel with transmission $\mathcal{T}_{chan} = 1$, (b) with a finite transmission $\mathcal{T}_{chan} < 1$ and (c) would be an according detector signal similar to Ref. [38].

$p = |A|^2$, $q = |B|^2$ and $N = e|V|t/h$. When we define a channel transmission $\mathcal{T}_{chan} = p = |A|^2$ and reflection $\mathcal{R}_{chan} = 1 - \mathcal{T}_{chan} = q = |B|^2$ and recognize N as a number of particles driven by the bias V that attempt to overcome the barrier (and N/t as the maximum current for a single-mode conductor $g_0 V$) and check the first and second moment $\langle I \rangle = pN/t = \mathcal{T}_{chan} g_0 V$ and $\langle \Delta I^2 \rangle = pqN/t = (1 - \mathcal{T}_{chan})\langle I \rangle$ this resembles the Landauer formula and the formula for shot noise intensity [36]. Here one also has to point to the bias depending factor $e^{\pm i\lambda e|V|t/h}$ in Eq. 2.63. This comes from the coupling to the detector and shows that the phase of a transmitted electron is influenced by the detector. Since the probability amplitude stays unaffected this does not alter the probabilities P_m, but can have an important influence on the whole system if the detector is phase sensitive. [35, 37]

Physically shot noise arises due to the granularity of the process. When discrete, identical particles hit a barrier and partially and statistically are transmitted and reflected this kind of noise shows up. It is also referred to as *partition noise*; a fully occupied single mode conductor is noiseless and a barrier with a finite transmission $\mathcal{T}_{chan}$ produces this kind of noise by partitioning the particles into the different channels. Then one does not have a uniform row of particles, but a random series of particles and holes (see Fig. 2.11). This can be seen very nicely in an experiment in which electrons are really detected one by one as in Refs. [38, 39] and basically the only way to get insight into these microscopic processes and to learn about higher order cumulants of the FCS. Other experiments succeeded only in measuring the third moment directy as the spectral density S_{I^3}, which is already a very small quantity [40].

More usual is to utilize the spectral density $S_I = 2q\langle I \rangle(1 - \mathcal{T}_{chan})$ to determine the charge q of the quasi particles that transport current, such as in superconducting materials ($q = 2e$) [41] or fractional charges in the FQHE [42, 43].

To summarize the important points: A barrier with transmission $\mathcal{T}_{chan}$ in a single mode conductor leads to fluctuations which follow binomial statistics and the generating function has higher order moments (cumulants). Measuring the current directly one only has access to the first moments, the average current $\langle I \rangle$ and the variance $\langle \Delta I \rangle$. However, with a detector coupled by a parameter λ to the system, which is able to count single particles, one can recover the whole statistics. Thus the coupling λ plays an important role, because when it is very small, which is usually the case, a distribution can be effectively Gaussian because higher order elements vanish as fast as λ^n.

2.5. Aharonov-Bohm Interferometry

This section is meant to be a short overview of the Aharonov-Bohm effect and interferometers which are built using it.
As one of the *seven wonders of the quantum world* [44] (and in the range of the topic of this thesis there are actually even two more to come) I want to at least briefly discuss the Aharonov-Bohm effect. W. Ehrenberg and R. E. Siday in 1949 [45] were the first who predicted this effect and its first detailed presentation came from Ykar Aharonov and David Bohm [46], so this effect sometimes also is referred to as *Ehrenberg-Siday-Aharonov-Bohm effect*. It shows that electromagnetical potentials V and $\boldsymbol{A}$ are not mere mathematical scaffoldings to describe electromagnetism as they appeared to be at the times of Maxwell, but have a physical meaning and influence like the fields $\boldsymbol{E}$ and $\boldsymbol{B}$.
Let's start with the (time-dependent) Schrödinger equation

$$\left[\frac{1}{2m}\left(\frac{\hbar}{i}\nabla - q\boldsymbol{A}\right)^2 + U\right]\Psi = i\hbar\frac{\partial\Psi}{\partial t} \tag{2.65}$$

with a vector potential $\boldsymbol{A}$ from a homogeneous field $\boldsymbol{B}$ in z-direction, an arbitrary potential energy U for particles with charge q following a defined path as depicted in Fig. 2.12. One can simplify the problem by adding to the wave function the so-called Peierls phase

$$\Psi = e^{ia}\Psi', \tag{2.66}$$

where

$$a(\boldsymbol{r}) \equiv \frac{q}{\hbar}\int_{\mathcal{O}}^{\boldsymbol{r}} \boldsymbol{A}(d\boldsymbol{r}') \cdot d\boldsymbol{r}', \tag{2.67}$$

and $\mathcal{O}$ is an arbitrary reference point. Putting this into Eq. 2.65 one can cancel the common factor of e^{ia} and one is left with

$$-\frac{\hbar^2}{2m}\nabla^2\Psi' + U\Psi' = i\hbar\frac{\partial\Psi'}{\partial t}, \tag{2.68}$$

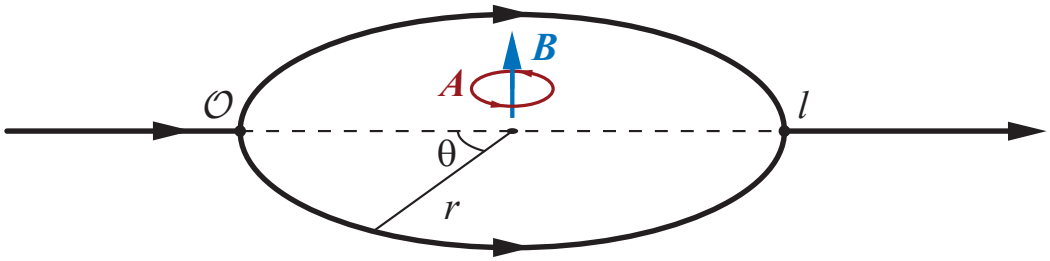

Figure 2.12.: An electron path splits at $\mathcal{O}$ and electrons can go the upper or lower semicircle surrounded by a homogeneous vector potential $\boldsymbol{A}$ and thus acquire a quantum mechanical phase difference $\Delta\varphi = e\Phi/\hbar$ when traveling to l.

which simply is a Schrödinger equation without a vector potential $\boldsymbol{A}$. The phase difference, the so-called Aharonov-Bohm phase, between an electron traveling the upper ($\boldsymbol{r}_+$) and lower ($\boldsymbol{r}_-$) half of a closed path (see Fig. 2.12) is

$$\begin{aligned}\Delta\varphi = a_+(\boldsymbol{l}) - a_-(\boldsymbol{l}) = \frac{q}{\hbar}\left(\int_{\mathcal{O}}^{\boldsymbol{l}} \boldsymbol{A}\cdot d\boldsymbol{r}_+ - \int_{\mathcal{O}}^{\boldsymbol{l}} \boldsymbol{A}\cdot d\boldsymbol{r}_-\right) = \\ = \frac{q}{\hbar}\oint \boldsymbol{A}\cdot d\boldsymbol{r} = \iint \nabla\times\boldsymbol{A}\cdot d\boldsymbol{S} = \frac{q\Phi}{\hbar}\end{aligned} \tag{2.69}$$

with Φ being the magnetic flux penetrating the circle between the paths. What is remarkable here is that this is true not only if the magnetic field stretches over the whole area $\boldsymbol{S}$ between the paths, but also if it is confined to a certain region between the electron paths, so that the electrons do not go directly through the actual field, but pass regions where only a vector potential $\boldsymbol{A}$ is present. The field $\boldsymbol{B}$ produces a classical force on a charged particle and might alter its path, to which we can relate in a classical sense. The vector potential $\boldsymbol{A}$ shifts the quantum mechanical phase of a charged particle, which is classically and experimentally less accessible. This nonlocality is of major importance in quantum mechanics and is another example why it is so inconceivable in daily life terms.

Experimentally it was proved only one year after the publication of Aharonov and Bohm, 1960, by R. G. Chambers in an electron microscope [47]. It remains an important effect to this day, recently studied in solid state physics double-slit experiments in a 2DEG [12, 48] and in mesoscopic rings [49, 50].

Such *Aharonov-Bohm rings* are investigated in a variety of experiments [48, 51, 52]. A more recent experiment is shown in Ref. [53], where it is demonstrated how a which-path investigation will let the wave function of the interfering particle collapse. The Aharonov-Bohm ring contains a quantum dot in one arm, which is capacitively coupled to a QPC for charge read-out. When the quantum dot is adjusted to a Coulomb peak both interferometer arms are open for coherent transport. When measuring Aharonov-Bohm

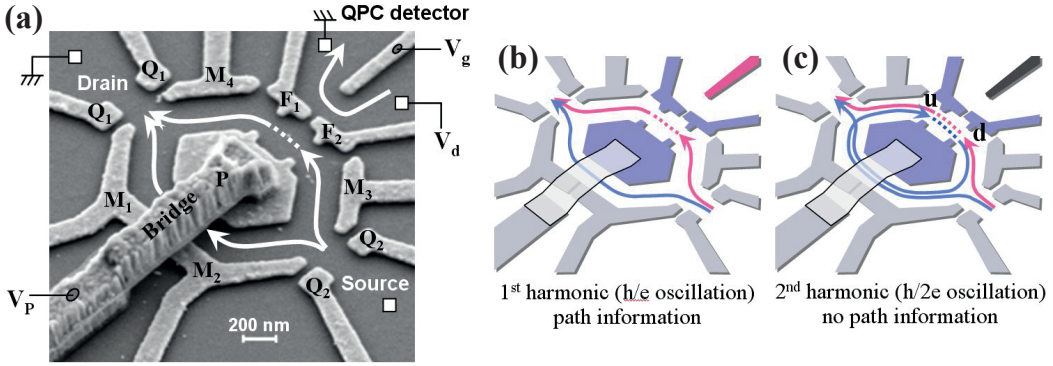

Figure 2.13.: (a) SEM image of a closed-loop Aharonov-Bohm interferometer fabricated on the surface of a 2DEG wafer. The device consists of two parts: an electronic interferometer and a QPC detector. (b) The trajectory leading to the first-harmonic interference (h/e conductance oscillation), where the charge detection is equivalent to the path detection. (c) The trajectory leading to the second-harmonic interference ($h/2e$ conductance oscillation), where the charge detection is not necessarily the path detection. Taken from [53].

oscillation by sweeping the magnetic field two harmonics with oscillation periods of h/e and $h/2e$ respectively can be observed. The first harmonic corresponds to a wave function where the electron goes either one or the other arm and interferes at the drain contact. The second harmonic represents a wave function with interference not just between paths of the two arms, but one path goes once more around the whole interferometer as depicted in Fig. 2.13(c). When operating the QPC simultaneously to detect a charge in the embedded quantum dot, one also measures the which-path information in the case of the first harmonic, because only one path leads through the quantum dot. For the second harmonic both paths go through the quantum dot, thus the interference of the second harmonic is not (less) disturbed by read-out of the QPC. In general one can say, that not only the Aharonov-Bohm effect itself is a quantum effect, interferometers based on it are suitable to study other quantum phenomena, because they can reveal the phase and thus the wave nature of electrons/particles.
A special kind of Aharonov-Bohm interferometer is the electronic Mach-Zehnder interferometer on which I focus in the following section.

2.6. The electronic Mach-Zehnder interferometer

A Mach-Zehnder interferometer is a two-beam interferometer and described in many textbooks of optics [54]. Fig. 2.14 displays the simple concept of a Mach-Zehnder interferometer; an incident light beam coming from a source **S** is divided in a semi-

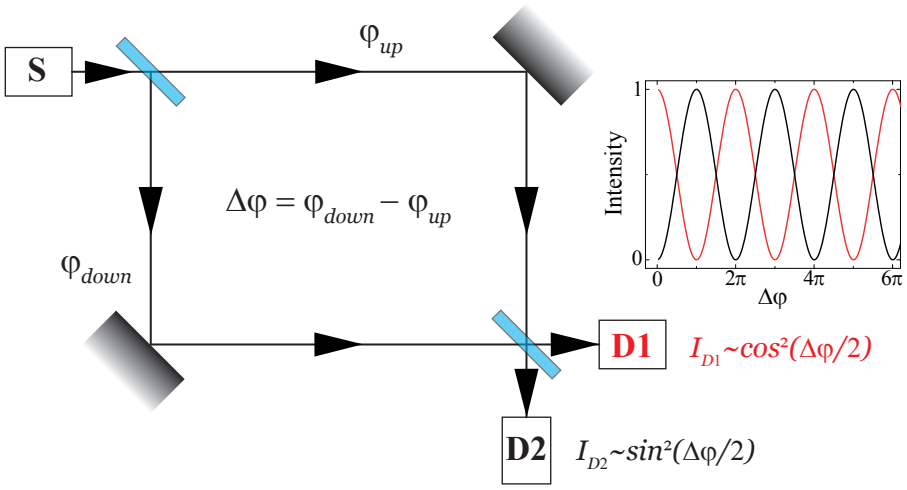

Figure 2.14.: A beam of light incident from **S** is split in two partial beams at the first semi-transparent beam splitter. The two partial beams acquire geometrical phases φ_{up} and φ_{down} respectively and are rejoined at the second beam splitter. The light intensity is measured in detectors **D1** and **D2**.

transparent beam splitter into an *upper* and *lower* beam which acquire on their paths the phases φ_{up} and φ_{down} respectively. Recombined in the second beam splitter they interfere and the phase difference $\Delta\varphi = \varphi_{down} - \varphi_{up}$ causes the oscillation between transport to detector **D1** or to **D2**, resulting in intensity oscillations in each detector with a phase shift of π between each other. In general this interferometer is of interest, because it is sensitive to very small phase shifts, and quantum mechanically, since it can be operated with single photons. This made A. C. Elitzur and L. Vaidman 1993 propose a quantum mechanical interaction-free bomb tester [55], the second of the *Seven wonders of the quantum world* [44], which was realized only one year later by Kwiat et al. [56]. The phase shift of the interferometer is set such that each single photon is ideally led only into, e.g., **D1**. Then, a bomb, which is triggered by a passing photon, is set next to one interferometer arm. If the bomb works, the interference is destroyed and the bomb might explode if a photon passes the corresponding arm. A dud would not interact with a photon and the interference would be sustained. Then, a single photon is sent into the interferometer. Possible scenarios: It is a dud and the photon is detected in **D1** with 100% probability. When it is a bomb, there is a 50% chance that the photon passes the bomb and everything explodes. That it travels in the other arm has 50%, too, and the photon arrives at the second semitransparent mirror without interference effect (and the bomb also does not explode). This means another 50% that it is detected either in **D1**, or **D2**. Resulting in a 25% chance, that the photon is detected in **D2**, indicating a working bomb without letting it explode. So this experiment shows the possibility of

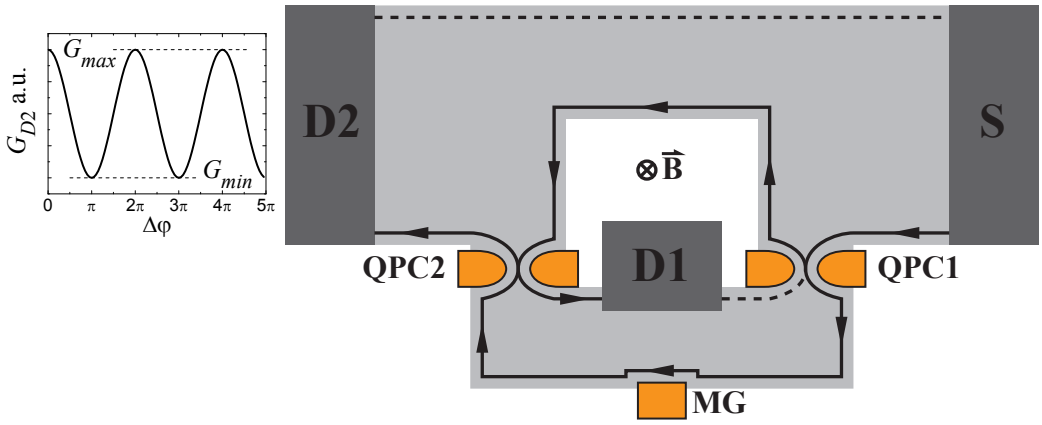

Figure 2.15.: Similar to the optical Mach-Zehnder interferometer an edge channel incident from source **S** is partially transmitted (reflected) at a QPC 1 operating as a beam splitter. An electron wave function traveling with 50% in the upper and lower arm respectively acquires the Aharonov-Bohm phase $\Delta\varphi$ and will interfere corresponding to this phase in QPC 2. Oscillating conductance signals can be detected in the detector drain **D1** or **D2**. The phase difference is adjusted by magnetic field or by the enclosed area by varying the modulation gate **MG**.

an interaction-free measurement and is also interesting for a non-dispersive readout. Another interesting possibility is that one can extend a Mach-Zehnder interferometer to perform the Hanbury Brown and Twiss experiment to see random, bunched, or antibunched photons, depending on the photon source [57]. So far, we looked at the Mach-Zehnder interferometer as a optical device working only with photons, but since this effect also is depending on the statistics of the particle involved [58], one may think about realizing such a interferometer with different kinds of particles.
In the quantum Hall regime the edge channels can be viewed as single mode electron "beams", which are used as a pendant of the light (laser) beams in the optical case. Then QPCs, set to half transmission, are used as beam splitters and the edge of the sample defines the electron paths as can be seen in Fig. 2.15. Electrons originating from source **S** travel to QPC 1, their wave function splits according to the QPC transparency, goes the upper and lower arm of the interferometer and rejoins to interfere at QPC 2. Depending on the accumulated phase difference between the paths the electron is either sent to drains (detectors) **D1** or **D2**. An electronic Mach-Zehnder interferometer was first realized in 2003 by Ji et al. [15]. Originally it was developed to investigate interference of quasiparticles with fractional charges in the fractional quantum Hall regime. However, there are also early proposals to perform, on basis of two coupled Mach-Zehnder interferometers, a Hanbury Brown-Twiss experiment (two-particle interference realized in Ref. [59]) to show entanglement with the violation of Bells inequalities [60,61]. For the

electronic Mach-Zehnder interferometer the phase difference is due to the Aharonov-Bohm effect, and defined by the magnetic flux enclosed by the two electron paths. One can see that it is a special case of an Aharonov-Bohm interferometer. The resulting zero bias conductance in the ith drain is then

$$G_{Di} \propto \mathcal{T}_{SDi} = |\psi_{up,Di} + e^{i\Delta\varphi}\psi_{down,Di}|^2 \tag{2.70}$$

with $\mathcal{T}_{SDi}$ the transmission from source to drain i, which is the square of the absolute value of the sum of the amplitudes. With the transmission (reflection) amplitudes t_i (r_i) (with $|t_i|^2 + |r_i|^2 = 1$) this becomes

$$\begin{aligned} G_{D1} &\propto \mathcal{T}_{SD1} = |t_1 r_2 - e^{i\Delta\varphi} r_1 t_2|^2 = |t_1 r_2|^2 + |r_1 t_2|^2 - 2|t_1 t_2 r_1 r_2| \cos\Delta\varphi \\ G_{D2} &\propto \mathcal{T}_{SD2} = |t_1 t_2 + e^{i\Delta\varphi} r_1 r_2|^2 = |t_1 t_2|^2 + |r_1 r_2|^2 + 2|t_1 t_2 r_1 r_2| \cos\Delta\varphi. \end{aligned} \tag{2.71}$$

We see the oscillating current/conductance to drain $D1$ and $D2$ is shifted by π so that $\mathcal{T}_{SD1} + \mathcal{T}_{SD2} = 1$, or $G_{D1} + G_{D2} = g_0$ for the conductance when taking a single edge channel into account as in Fig. 2.15 (*ff* $= 1$).
When changing the Aharonov-Bohm phase $\Delta\varphi$ we see sinusoidal oscillations in the conductance around a mean value. To change the phase we need to change the magnetic flux enclosed by the interferometer arms. This can be done either by varying the magnetic field, or the area. For the latter a modulation gate **MG** is used as shown in Fig. 2.15 to deflect the edge channel and thus change the area in a very controlled way, in contrast to sweeping the magnetic field by amounts of $\sim 10\,\mu$T while being in the quantum Hall regime at ≈ 5 T.
A degree of coherence in such interferometers is the visibility ν, which is defined as the amplitude of the oscillations divided by the mean value, or in terms of conductance (intensity) extrema [6]

$$\nu = \frac{G_{max} - G_{min}}{G_{max} + G_{min}}. \tag{2.72}$$

Using Eq. 2.71 for the visibility and the transmissions from QPC 1 and 2, $\mathcal{T}_i = |t_i|^2$, we arrive at

$$\nu = \frac{2\sqrt{\mathcal{T}_1(1-\mathcal{T}_1)}\sqrt{\mathcal{T}_2(1-\mathcal{T}_2)}}{\mathcal{T}_1 + \mathcal{T}_2 - 2\mathcal{T}_1\mathcal{T}_2}. \tag{2.73}$$

This simplifies to $\nu = 2\sqrt{\mathcal{T}_1(1-\mathcal{T}_1)}$ when $\mathcal{T}_2 = 0.5$, or vice versa, and displays an arch with a maximum at $\mathcal{T}_1 = 0.5$.
So far we have not taken into account any kind of dephasing and in general this topic will be covered in the chapter 5 and 6 of this thesis. As seen in Eq. 2.6 an important quantity for dephasing is the energy window $\Delta = E - E_\mathrm{F}$, determined by a finite

[6] The usual definition of the visibility is in terms of (differential) conductance oscillations. One can also define an equivalent visibility using current oscillations which is not used in general and would be labeled as ν_I in this thesis.

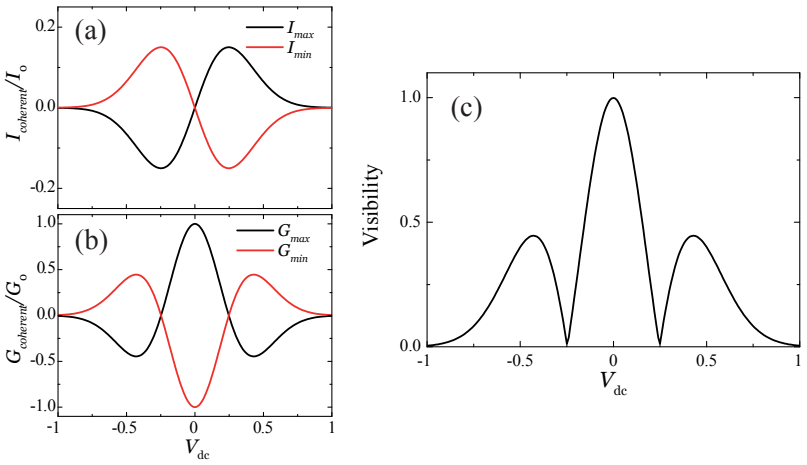

Figure 2.16.: (a) Ohmic coherent current $I_{coherent}$, which is suppressed for large bias. (b) The corresponding coherent differential conductance shows a central lobe and single side lobes, which also exhibits itself in (c) the (differential) visibility, as calculated from Eq. 2.72.

temperature or voltage. Here in the basic chapter only a very simple and introductive example of dephasing by an applied bias voltage $V_{\rm dc}$ that leads to phase noise inside the interferometer is presented. This noise can be assumed to be Gaussian with a variance $\langle\delta\varphi^2\rangle \propto V_{\rm dc}^2$. The visibility is defined by zero bias conductance, but this can be done as well with the differential conductance $G(V_{\rm dc}) = dI(V_{\rm dc})/dV_{\rm dc}$ to investigate the bias dependence[7]. The current can be split into an average part $I_{average}$ and a coherent part $I_{coherent}$ and the coherent part is ideally $I_{coherent} \propto I_0 \sin(\Delta\varphi)$, where I_0 is an amplitude that behaves ohmically with the voltage $V_{\rm dc}$. With the random phase distribution this becomes $I_{coherent} \propto I_0 \sin(\langle\Delta\varphi\rangle)e^{-\langle\delta\varphi^2\rangle/2}$ and with the proportionality $\langle\delta\varphi^2\rangle = V_{\rm dc}^2/V_0^2$ we see that the maximal current ($\langle\Delta\varphi\rangle = \frac{\pi}{2}, \frac{5\pi}{2}, \frac{9\pi}{2}, ...$) is

$$I_{max} = I_0 e^{-V_{\rm dc}^2/2V_0^2} = G_0 V_{\rm dc} e^{-V_{\rm dc}^2/2V_0^2}. \tag{2.74}$$

The minimal current is simply $I_{min} = -I_{max}$ and we see they are a combination of an ohmic part which is visible around $V_{\rm dc} = 0$ followed by an exponential decay illustrated in Fig. 2.16(a). Assuming ohmic behavior for $I_{average}$ we get a constant $G_{average} = I_{average}V_{\rm dc}$, which is true for $\mathcal{T}_1 = \mathcal{T}_2 = 0.5$, and the coherent conductance $G_{coherent}(V_{\rm dc}) = dI_{coherent}(V_{\rm dc})/dV_{\rm dc}$ [Fig. 2.16(b)]. Then we can simply use $\nu(V_{\rm dc}) = |G_{max/min}(V_{\rm dc})| = |dI_{max/min}(V_{\rm dc})/dV_{\rm dc}|$ [Fig. 2.16(c)]. The nodes appear at the voltage V_0 and this gives a characteristic energy[8] $\varepsilon_0 = 2eV_0$.

[7] The following is a free report of the explanation of the bias dependence from Ref. [62]

[8] This is one energy scale among others that will be introduced in this thesis. To keep track of all these energy scales in the course of this thesis, appendix B gives an overview of them.

In contrast, naively one would think, that the visibility should not change when the average conductance does not change. And even if one adds a certrain dephasing with bias, one would think the visibility follows this dephasing, rather, than developing lobes and nodes. However, the above shows that an ohmic coherent current that is exponentially suppressed for large bias voltages leads to a bias dependence with lobes and nodes in the conductance. An obvious reason for such a bias dependent suppression of coherence are simply the QPCs inside the interferometer which are set usually to a transmission close to 0.5 (between 1 and 0), so one expects shot noise.

As a short recall of this chapter, fundamental properties of a 2 dimensional electron gas in a semiconductor heterostructure, which is used for the following experiments, are presented. Next the development of one-dimensional edge channels in the quantum Hall regime at high magnetic fields are described and some of their transport properties. After looking at fluctuations produced by a QPC, a building block of a Mach-Zehnder interferometer, and how they can be theoretically investigated, Aharonov-Bohm interferometers are briefly presented. At last a short introduction to electronic Mach-Zehnder interferometer themselves is given. So now after this basic chapters we are well prepared to look at the actual experiments that are performed.

3. Measurement techniques

"It is impossible to get anywhere without sinning against reason."
Albert Einstein

The energy scale that destroys coherence in an electronic Mach-Zehnder interferometer, or other electronic interferometers in a 2DEG, is of the order of tens of micro-electron Volts. Converted to a temperature this means that at approximately 100 mK there will be no coherent effects anymore, which illustrates how sensitive these measurements are and what high demands this makes on the measurement equipment and setup.
This chapter deals with this topic. In the first section the refrigerator is described that ensures a minimal environmental influence. The following section presents the measurement setup and equipment that is used for high sensitive and non-invasive measurements in the quantum Hall regime.

3.1. Cryostat and devices

The samples to be measured are cooled down in a Minidil dilution refrigerator from Air Liquide with a base temperature of approximately 25 mK. The working principle of a dilution refrigerator lies in two properties of a liquid ^{3}He$-^4$He mixture. One is that a mixture with more than 6.6% of ^{3}He will develop two separate phases when cooled below ~ 870 mK. One is the ^{3}He rich phase which becomes pure at temperature $T = 0$. The other is the ^{4}He rich phase (^{3}He diluted phase) which has the peculiarity that even for $T = 0$ the ^{3}He concentration will not fall below 6.6%. The second property of a ^{3}He$-^4$He mixture is that in the two phase regime the enthalpy H of the diluted phase is larger than that of the pure phase, the *heat of mixture*.
In a ^{3}He cryostat pumping at the liquid ^{3}He results in a reduced vapor pressure and thus the evaporation cooling. Analogously in a dilution refrigerator the ^{3}He concentration in the diluted phase is reduced. Then ^{3}He from the pure phase will flow into the diluted phase to sustain the concentration of 6.6% which will lead to a cooling power due to the heat of mixture, which is larger than that of a ^{3}He refrigerator for $T < 350$ mK. [63]
In the mentioned dilution refrigerator this is realized as follows: In the mixing chamber, located in the inner vacuum chamber in a dewar with a liquid ^{4}He bath, are the two phases; the light pure ^{3}He phase on top and the diluted phase below at a base temperature

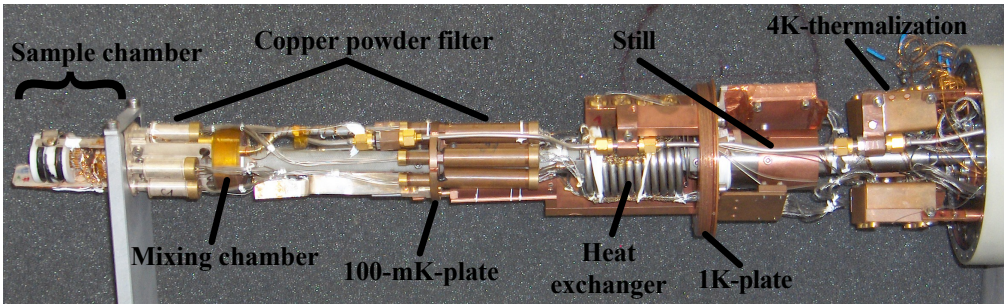

Figure 3.1.: Lower part of cryostat insert with copper powder filters, mixing chamber and sample holder.

of $T \approx 25\,\mathrm{mK}$. This diluted phase is connected by a tube with the still, which is at $T \approx 850\,\mathrm{mK}$. At this temperature the vapor pressure of ^{3}He above the mixture is typically 90%. It is pumped to decrease the ^{3}He concentration in the diluted phase. At room temperature it is led through the pump to a compressor and then, after cleaning the gas with a liquid nitrogen trap, re-injected into the cryostat. Precooled by the ^{4}He bath it is then cooled to $\sim 1.5\,\mathrm{K}$ with a Joule-Thomson expansion stage and condenses before the main flow impedance, which is needed to ensure a sufficiently high pressure to keep the ^{3}He condensed. Via heat exchangers starting from the still it is further pre-cooled by the upstream dilute phase into the still from the mixing chamber. Then separately it enters the mixing chamber on top into the pure phase from where it is sucked again into the diluted phase and the cycle can repeat.

The refrigerator is built in a massive copper chamber to shield electromagnetic fields and acoustic noise. Next to thermometry and heater cables, 20 lines are led into the cryostat's sample chamber. Each line contains π-filters at the copper chamber feed through and the cryostat socket to reduce high frequency signals in the line from the environment and the electronic equipment. Inside the cryostat copper powder filters (CPF) are placed at 100 mK and 25 mK (see Fig. 3.1). They serve as thermalization for the electrons in the lines and to prevent electron heating at low temperatures by blackbody radiation from hotter parts of the setup traveling through the lines. Eight of the lines are coaxial and are used in this experiment for the conductance measurements, i.e., applying voltage and detecting current or voltage. Remaining lines are twisted pair and with these the gates are operated. For this purpose additional 5 Hz low pass filters are attached to the cryostat socket to save the sensitive metallic top gates from ac peaks (see Fig. 3.3).

Next to the cryostat a superconducting magnet is set into the dewar to reach fields up to 8 T.

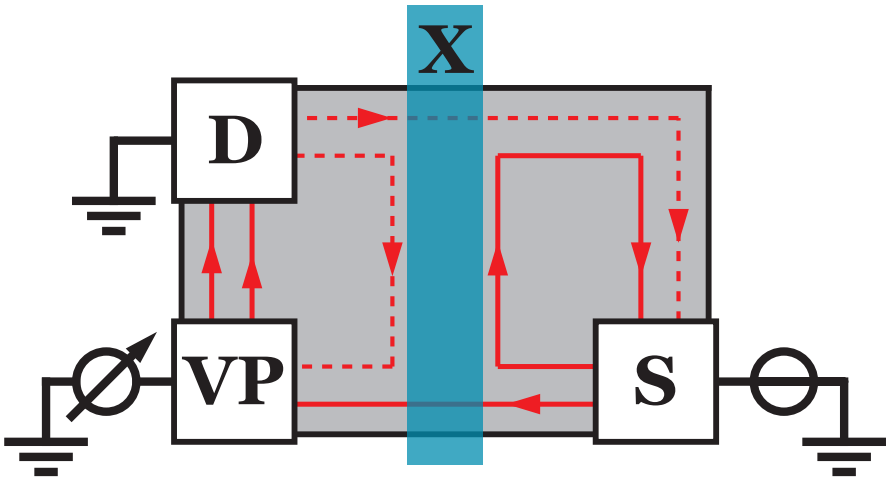

Figure 3.2.: Sketch to illustrate the employed current measurement. Voltage is applied at **S**, the structure **X** manipulates the conductance. Then the voltage probe **VP** measures the voltage that drops off at the available edge channels to the drain **D**.

3.2. Measurement approach

For measuring the conductance of QPCs or quantum dot (QD) systems a standard two point measurement is used. One applies a voltage by a voltage divider at room temperature to the measuring line that leads down into the cryostat to the sample. The current flowing out of the drain is led to room temperature again where it is fed into a current-voltage (IV) converter. The reservoirs of the electrons are at room temperature and they have to thermalize along the measurement lines. This contains several drawbacks. Voltages produced by the temperature difference between the inside and the outside of the cryostat are applied directly to the sample. These voltages drift uncontrolled in the μV range and are parasitic to the coherence of states with low energies.
Despite the thermalization of the lines, the electrons in the sample are heated by a ground drain at room temperature. Additionally every IV-converter produces current noise and an additional drifting voltage offset. These excitations do not strongly influence a QPC or QD state, but the electron coherence over long distances of a few micrometer in the Mach-Zehnder interferometer will be diminished if not even destroyed completely.
We overcome this by several means. First we build in a voltage divider 10^{-4} into the cryostat at low temperatures (green resistors R1 and R2 in Fig. 3.3). Thus any "warm" fluctuations and especially the thermoelectric voltage, reaching some few μV, is scaled down and almost negligible.
For the conductance measurement we exploit the perfectly known resistance of quan-

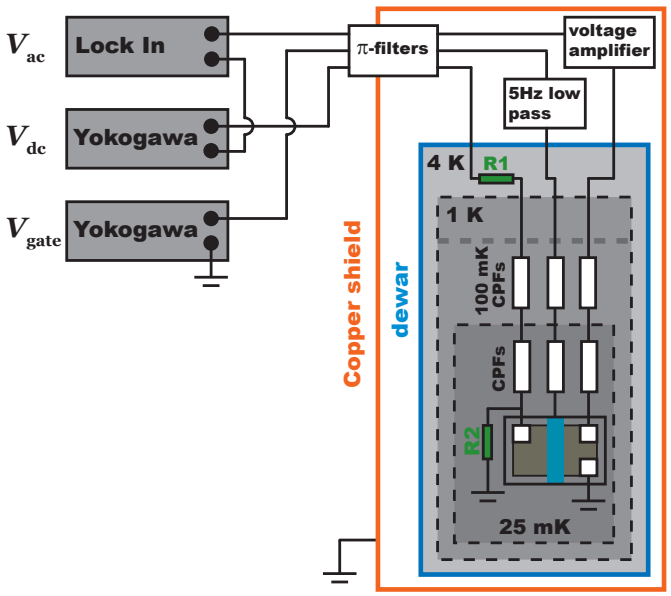

Figure 3.3.: Complete measurement setup containing wiring, grounding of the sample, the filters, shields and devices. The green resistors R1 and R2 are the additionally built in voltage divider. Low pass filters (5 Hz) are attached to lines with gates.

tum Hall edge channels, the von Klitzing constant R_{K}, as a shunt resistor R_{shunt} to record the current through the interferometer by measuring voltage. This has the advantage that voltage amplifers have a small, non-drifting input offset ($< 1\,\mu$V) compared to IV-converters ($\approx 10\,\mu$V). Fig. 3.2 shall illustrate this in the case for $ff = 2$. At the source contact **S** the voltage $V_{\mathbf{S}} = dV_{\mathrm{ac}} + V_{\mathrm{dc}}$ is applied, which leads to a current flow through the sample. The structure **X** modifes the current coming from the source contact **S**. This sample current $I_{\mathbf{X}} = dI_{\mathbf{X};\mathrm{ac}} + I_{\mathbf{X};\mathrm{dc}}$ passes the voltage probe contact **VP** and fows through the two present edge channels with the shunt resistance $R_{shunt} = R_{\mathrm{K}}/ff$ to the drain **D**. Measuring the voltage $dV_{\mathbf{VP};\mathrm{ac}}$ at **VP** we can deduce the current $dI_{\mathbf{X}} = dI_{\mathbf{D}} = \frac{dV_{\mathbf{VP};\mathrm{ac}}}{R_{shunt}}$ and thus the (differential) conductance $G_{\mathbf{X}} = \frac{dI_{\mathbf{X}}}{dV_{\mathrm{ac}}}$. As a small ac excitation dV_{ac} we use $1\,\mu$V to have linear response and a dc voltage V_{dc} up to $150\,\mu$V.

At last all the grounds at the sample (drain, voltage divider) are at cryogenic temperatures. This way we can avoid unnecessary contact to the environment outside the cryostat, that even a good filtered line can produce, and reach electron temperatures of $\approx 30\,$mK.

These methods enable us to perform a very non-perturbative measurement, which is crucial to have a long coherence time in the interferometer.

As equipment we used *Yokogawa DC power sources* for the gate voltages and the dc

bias voltages. Additionally for the gates a voltage source made by the electronic workshop of the physics faculty was utilized. To amplify the signal from the sample we used the differential preamplifier *LI-75 A* by *Arstec* for the described low-invasive current measurement. For few characterizations of the QPCs as described in Sec. 4.2.2 a *Variable Gain Sub Femto Ampere Current Amplifier DDPCA-S* of the company *Femto* was used. *Stanford Research Systems Lock-In Amplifiers SR830* were utilized to produce a small ac excitation voltage and detect the corresponding signal. The layout of the whole setup can be seen in Fig. 3.3.

4. Sample fabrication and characterization

"Quantum Mechanics can be seen as a rediscovery of Shiva, the Hindu god of chaos and destruction."

Gary Zukav

The sample fabrication of an electronic Mach-Zehnder interferometer contains some subtle points. Many succeeding lithography steps, small ohmic contacts and the gold air bridges lead to decreased statistics of successfull sample completion. Here I will give an overview of the recipe with highlighting these special problems. The second section covers the basic characterization of a sample.

4.1. Fabrication

4.1.1. Material

For the realization of an interferometer a large coherence length is favorable. As already mentioned, the momentum relaxation length l_m is almost infinite in a quantum Hall edge channel and the actual mobility of the wafer is of less importance. And one hopes, that the phase relaxation length l_φ behaves similarly, which is, unfortunately, not quite the case. Still, a large mobility is favorable. Since the background potential of the doping layer is responsible for the impurity potential one can increase the mobility by increasing the spacing layer. On the other hand we want to define a distinct electrical potential with the top gates, for this we need a small 2DEG depth. The usual compromise for high mobility 2DEG which is good to gate is a depth of $d_{\mathrm{2DEG}} = 90 - 100\,\mathrm{nm}$.
To easily reach a low filling factor with a low magnetic field it is also preferable to have a rather low electron density. In Tab. 4.1 all the important quantities of the two wafers which were used for this work are shown.

	Wafer no.	electron density (cm^{-2})	mobility (cm^2/Vs)	depth (nm)
Wafer A	D040203C	2.0×10^{11}	2.06×10^{6}	90
Wafer B	D061026B	2.12×10^{11}	2.8×10^{6}	90

Table 4.1.: Important parameters of the two wafer materials used in this work. Electron densities n and 2DEG depths d are (almost) identical, while the mobility is 30% larger in wafer B.

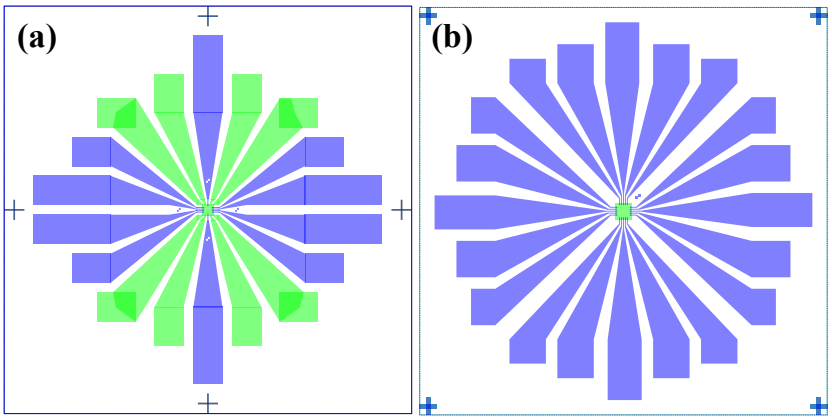

Figure 4.1.: Patterns of the optical masks. Remaining mesa displayed in green, the gold contact pads and leads are blue. (a) shows the old mask with the possibility to make ohmic contacts optically. In (b) all sample structuring is done with electron beam lithography in the remaining mesa island in the center.

4.1.2. Lithography

Standard optical and electron beam lithography (EBL) was used to structure the sample. Optically only a basis is patterned, the subsequent actual structuring is done solely with EBL. One starts with optically defining a square ($70\times70\ \mu m^2$) of mesa and etching with a mixture of sulfuric acid, hydrogen peroxide and water. The wet chemical etching with this composition is important to get a shallow slope ($\approx 45°$) of the mesa edges, which is crucial for the future evaporation of top gates, as described below. After that patterns of contact pads and leads are made optically and 5-10 nm chromium as adhesion layer and 150 nm gold are evaporated (see Fig. 4.1). These are used to later connect the Mach-Zehnder interferometer via bonding with the chip carrier.

The four following EBL steps have to be aligned with an accuracy of 100 nm or better (Fig. 4.2). After etching off the orange structures to define the sample mesa, the

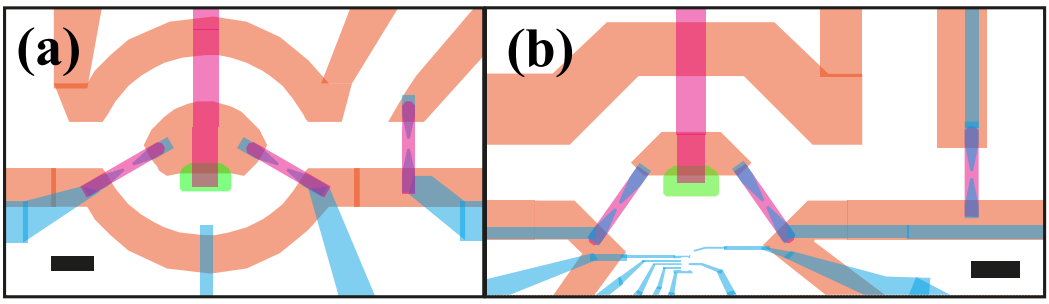

Figure 4.2.: Patterns of the EBL masks. Orange: mesa layer. Green: Ohmics. Blue: metallic gates. Pink: gold air bridges. The black scale bar represents 2 μm.

ohmic contacts are made. After exposure and developement an alloy of 220 nm AuGe in the eutectic ratio and an additional layer of 55 nm Ni are evaporated. The Ni reduces the surface tension of the melting AuGe during the following annealing and the AuGe diffuses homogeneously into the substrate without building droplets. The annealing is done at a temperature of $450°$C, the time of annealing should be checked for each wafer. The standard recipe suggests 2 min pre-heating at $350°$C and then annealing for 50 s [64]. This works fine for optically defined contacts (sizes $> 50 \times 50\,\mu$m^2), but with decreasing size the success becomes more and more statistical. This statistics can be improved by longer annealing times of up to approximately 2 min (similar to Ref. [65]). Further increasing times may lead to problems with diffusive gold on the surface of the already deposited leads. The next step are golden top gates to define the QPCs and for later samples also gates for a possible double quantum dot [Fig. 4.2(b)]. These gates are built up of 5 nm chromium and $40 - 45$ nm gold and have to lie on the etched surface without break. Here it is important that the mesa edges are shallow, otherwise a gate might be disconnected.

4.1.3. Gold air bridges

Due to the topology of the sample geometry it is not possible to connect both QPC tips and the ohmic contact in the inside of the ring shaped mesa directly to the leads. Thus, next to the standard lithography, a technique to produce air bridges is used. For this purpose we employ a double layer EBL resist consisting of a low sensitivity bottom layer of PMMA and a thick high sensitive top layer of the copolymer PMMA-MA (Fig. 4.3). The bridge part of the structure is exposed with half of the dose of the pillars, then the development washes off all the resist at the pillars and leaves the bottom layer PMMA where the bridge will be. With the recipe described in the appendix and bridge sizes of

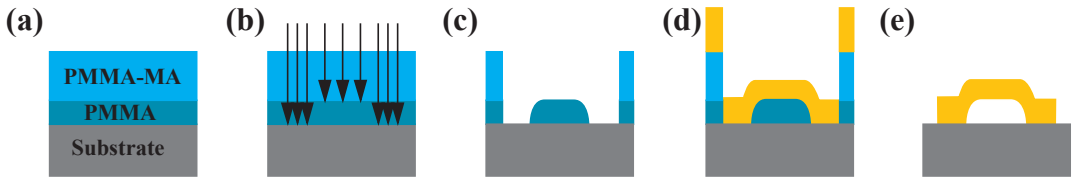

Figure 4.3.: Lithographical steps to fabricate gold air bridges: (a) shows the double layer resist on the substrate. (b) Exposure with double dose at the pillars. (c) Complete development only at pillars. (d) Evaporation of the metal. (e) After lift-off metal air bridges remain.

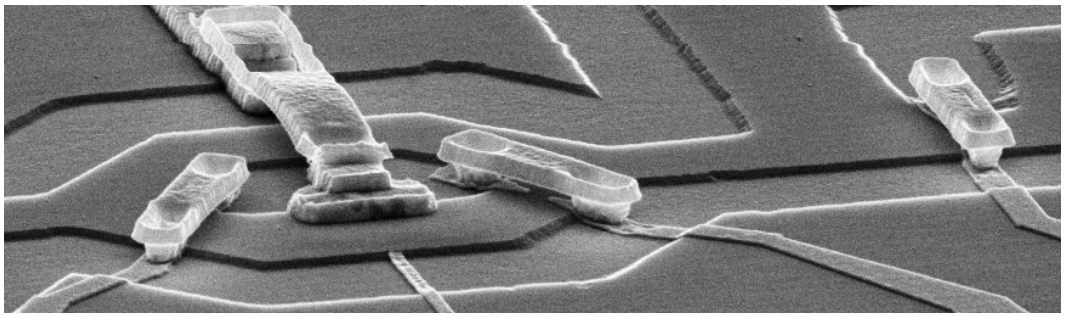

Figure 4.4.: Electron beam micrograph of a finished Mach-Zehnder interferometer. The etched mesa ring can be identified in the substrate. In the center of the ring the ohmic contact connected by a gold air bridge. Gates of thin gold that go smoothly across the mesa edges and different parts of a gate are connected by air bridges. Beneath these gates the tips of the QPCs can be recognized.

not much more than $1 - 2\,\mu$m and a width to length ratio close to one, approximately 90% of the air bridges survive the lift off.

4.1.4. Sample Design

After the described lithographic steps we end up with a sample as shown in Fig. 4.4. The etching is clean and homogeneous. The mesa edges are shallow enough, that the thin top gates continously lie over the step. The air bridges have heights of $\sim 300 - 400\,$nm and, when surviving the lift off, are very stable against mechanical stress. And all of the successive alignment steps have an accuracy below 100 nm.
There are two kinds of samples whose measurements are presented in this thesis. As shown in Fig. 4.1 and 4.2 samples of type A and B differ in geometry and gate structure. Samples of type A were fabricated by Leonid V. Litvin. The measurements were per-

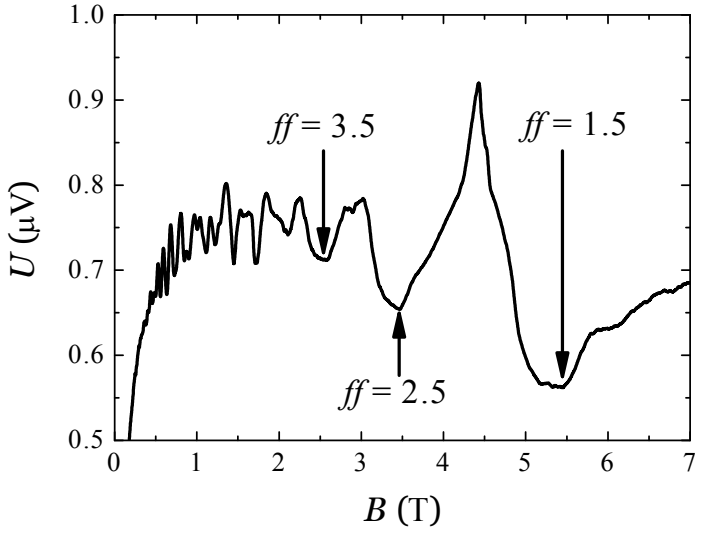

Figure 4.5.: The voltage U at the voltage probe **VP** versus the magnetic field B. Dips represent maximum scattering in the compressible bulk marking half-integer filling factors.

formed with my assistance and the analysis of data, which was not yet published, is done by me. Concerning samples of type B, fabrication, measurements and analysis were performed solely by me.

4.2. Characterization

After processing the sample it is glued into a chip carrier and mounted to the sample holder of the cryostat. When cooled down we need to characterize basic properties of the sample before the actual measurement. Here basically two things are important. One is the exact filling factor that we need to know for the experiment. As will be shown this has a strong effect on the coherence and behavior of the structure. Another point are the QPCs which are the building blocks of the Mach-Zehnder interferometer. Their characteristics are important for the functionality of the interferometer.

4.2.1. Filling factor

Identifying the filling factor works straightforward when measuring in a two-point or quantum Hall geometry. With the topology of the Mach-Zehnder interferometer and the measurement technique described in Chapter 3 the access to the overall conduc-

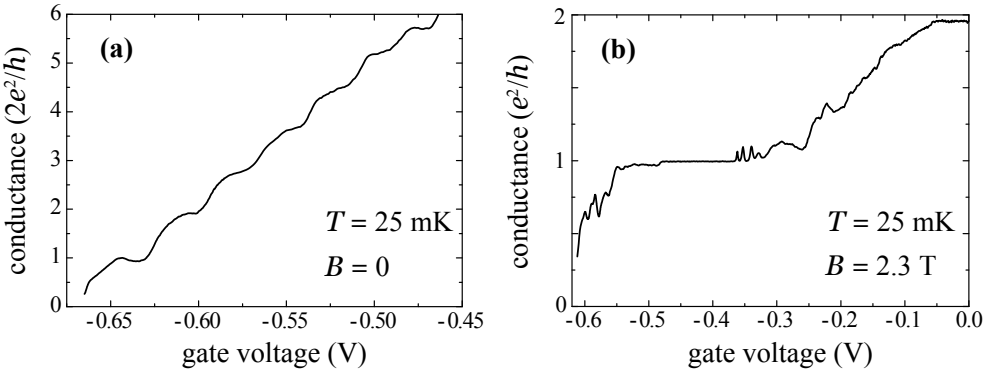

Figure 4.6.: Gate characteristics of a QPC at $T = 25\,\mathrm{mK}$ and $B = 0$ (a) and $B = 2.3\,\mathrm{T}$ (b). No resonances can be seen for zero field and many steps from the quantization inside the QPC are visible. For magnetic field at $ff \geq 2$ two plateaus from the two edge channels are visible, but the steps show various peaks and oscillations, indicating resonant states inside, or close to the QPC.

tance, Hall and longitudinal resistance is limited. The voltage we measure at the voltage probe **VP** is caused by the current flowing to the drain **D2** in distinct edge channels. At intermediate filling factors the scattering in the compressible bulk makes both drains available for electrons and we cannot determine the exact current from the measured voltage, because the exact resistance of the compressible bulk is unknown.

To find the filling factors and the exact electron density we apply a small ac excitation of $1\,\mu$V, leave all QPCs completely open (positive voltage of $\approx 300\,\mathrm{mV}$) and sweep the magnetic field. An example of how the voltage at **VP** develops with increasing magnetic field can be seen in Fig. 4.5. We see an oscillatory behavior similar to SdH oscillations. Here maxima correspond to integer filling factors, when scattering between counter propagating edge channels is minimal and almost all of the applied voltage drops between **VP** and **D2**. Minima occur when this scattering is maximal, indicating half-integer filling factors. This way we know the positions of certain filling factors and together with Eq. 2.12 we determine the electron density and thus the filling factors for any magnetic field. We find for a sample of wafer A an electron density of $1.97 \times 10^{11}\,\mathrm{cm}^{-2}$ and $1.84 \times 10^{11}\,\mathrm{cm}^{-2}$ for a structure of wafer B. This values are slightly smaller than for the unpatterned wafer, which is expected for structures of this size.

Most measurements in this work were performed at magnetic fields between the voltage minimum of $ff = 1.5$ and and the maximum of $ff = 2$.

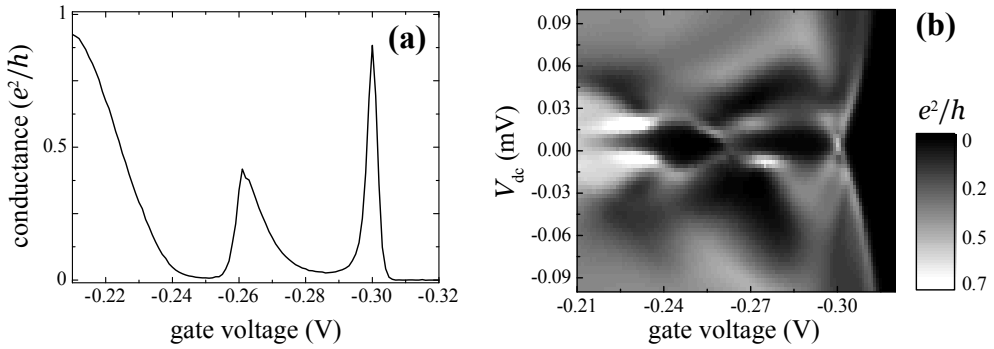

Figure 4.7.: A zero bias gate trace (a) and a 2D plot with the differential conductance (b) show the resonant states that can form close to a QPC while pinching off, and their bias dependence. The washed out Coulomb diamonds reveal a charging energy U_c which is typical for an antidot that can form due to an impurity.

4.2.2. Quantum point contacts

Next to the ohmic contacts and the sample edge itself, the quantum point contacts are the most important building blocks of the Mach-Zehnder interferometer. In this experiment we use them as *beam splitters* to partially reflect and transmit certain edge channels at one point. Naturally, the electron transport is already quantized by the quantum Hall effect. In the applied bias range the current-voltage characteristics are supposed to be linear and on varying the QPC gate voltage, we expect clean steps. Without magnetic field most QPCs with this high mobility wafer material show nicely developed steps without any resonances as in Fig. 4.6(a). At high magnetic field in the quantum Hall regime we see plateaus when a certain number of edge channels passes the QPC. When closing the QPC there are very often no nice steps between plateaus, but a series of dips and peaks [Fig. 4.6(b)].
We investigate the bias dependent differential conductance in Fig. 4.7(b) and find slightly distorted, but clearly visible Coulomb diamonds. The charging energy U_c estimated here is below 0.1 meV and a factor 10 smaller than expected for a localized state of the estimated small size of 100 nm between the QPC tips [66]. Antidots of a similar size and made of such materials in high magnetic field show this small charging energy and bias behavior [67]. Such inadvertent antidot can easily form at high magnetic fields. Impurities which induce only a small peak in the random background potential might not be recognized at $B = 0$, but at high magnetic fields in the quantum Hall regime these impurities can be encircled by a bound state similar to an antidot [68]. If this happens very close by or between the QPC tips the transport, while pinching off an edge channel, is governed by this bound state leading to dips and peaks around the conductance step. These resonances appear by accident and are sometimes unavoidable, but they have

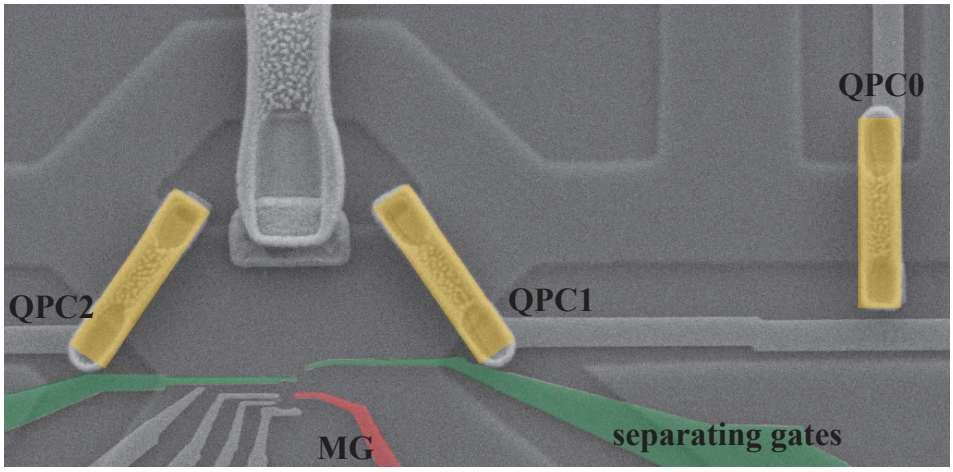

Figure 4.8.: Scanning electron micrograph of a sample of type B. Orange highlighted are QPCs $0-2$ to operate the Mach-Zehnder interferometer, red is the modulation gate and green separating gates to disconnect the interferometer from the lower circuit.

certain disadvantages for the interferometer. They distort the bias dependence of the interference because of their strong nonlinear differential conductance. And even at zero bias they alter the expected $\sqrt{\mathcal{T}(1-\mathcal{T})}$ behavior of the Mach-Zehnder interferometer visibility [69]. The effect on the interferometer is discussed in detail in Sec. 5.1.

4.2.3. Gate setting

A remark has to be made concerning samples of type B. As seen in Fig. 4.2(b) and 4.8, there are additional gates at the lower arm of the interferometer and ohmic contacts further below. These gates allow the formation of a double quantum dot coupled to the interferometer. For the experiments presented in this thesis, the lower circuit is not operated as such, but only the Mach-Zehnder interferometer alone. For this purpose the green highlighted separating gates in Fig. 4.8 are constantly charged by a voltage of $\sim -900\,\mathrm{mV}$ to ensure no electrical contact between the circuit of the Mach-Zehnder interferometer and the lower circuit. The red highlighted gate is used as the modulation gate which is still capacitively coupled to the lower interferometer arm with a minimum of $V_{\mathrm{mg}} = -250\,\mathrm{mV}$. This minimum voltage is necessary to avoid stray currents in the lower circuit that might disturb the coherence in the Mach-Zehnder interferometer. This is the basic setting whenever a sample of type B is mentioned below. Then the experimental situation is similar to that of a sample of type A.

5. Characteristics of an electronic Mach-Zehnder Interferometer

"If one has to stick to this damned quantum jumping, then I regret having become involved in this thing."

Erwin Schrödinger

In this chapter I will present basic characteristics of an electronic Mach-Zehnder interferometer. This is a neccesary foundation to understand the experiment in chapter 6 and to categorize it into previous experiments. The first section deals with basic measurements of conductance oscillations and how to obtain from these the most important parameter, the visibility ν, and its connection to QPC transmission. In the following section I describe the decoherence effects of temperature and of the size of the interferometer. The third section in this chapter covers the behavior of the Aharonov-Bohm oscillations at finite dc bias voltages. The appearance and number of lobes and nodes is still a matter of discussion and the core topic of the present work. In the final section I show how magnetic field and exact filling factor influence the coherence.
This chapter gives an overview of intrinsic properties of a Mach-Zehnder interferometer and its basis is a free, reorganized collection of former publications [69–72], and new data acquired in experiments during the course of my work.

5.1. Basic QPC adjustments and zero bias visibility

In the previous chapter I showed the sample preparation and the finished sample in Fig. 4.4. The exact experimental situation I want to explain according to the sample image and sketch in Fig. 5.1. All the measurements in this work are performed between $ff = 1$ and 2, meaning that in the sample not only one, but often two edge channels are present and contribute to the conductance. Accordingly two edge channels are sketched in Fig. 5.1(a) with the outer one black and the inner one light blue. The QPCs acting as beam splitters, QPC 1 and 2, and an additional QPC 0 are highlighted in orange. Fig. 5.1(b) shows the state of the interferometer as a simplified sketch without the actual mesa, only with the edge channels that make up the interferometer ring, omitting

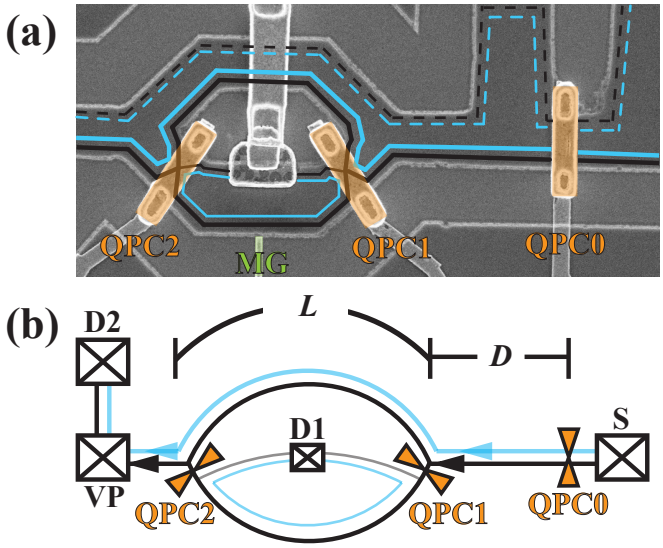

Figure 5.1.: Sample configuration and edge channels: (a) Scanning electron micrograph of a Mach-Zehnder interferometer together with a sketch of the edge channels at $ff = 2$. The outer channel is black, the inner is light blue. QPC (marked orange) settings here are: $\mathcal{T}_0 = 2$, $\mathcal{T}_1 = \mathcal{T}_2 = 0.5$. With the modulation gate (MG, light green) the active area and thus the phase difference can be varied. Most important edge channels are thick. (b) Simplified sketch illustrating the same situation in the interferometer displaying only ohmic contacts, QPCs and edge channels. Channels of the upper edge [dashed lines in (a)], the modulation gate and the mesa are neglected. The length of an interferometer arm is L and the distance between QPC 0 and QPC 1 is D. In the following the QPC setting is illustrated by this kind of sketch.

the dashed edge channels in the upper part in Fig. 5.1(a). The color code for edge channels and QPCs are the same. In the sketch also source contact **S**, voltage probe **VP**, and drains **D1** and **D2** are depicted. As explained in section 3 the current flowing into **D2** is measured via **VP**. The contacts **D1** and **D2** are connected directly to cold ground, but the current into **D1** is not being measured.

To become familiar with the topology of the sample with the edge channels, let us check the situation when all QPCs are open. Then all edge channels are biased from source **S**, go along the lower interferometer arm, and the maximum conductance is measured at **D2**. This is the situation when measuring the filling factor as in Fig. 4.5. Depending on the magnetic field, i.e., the filling factor, most of the current flows into **D2** and close to half-integer filling factors some part of the current goes into **D1** due to a Landau level in resonance with the Fermi energy and the resulting bulk resistivity. If $ff = 2$ and we start to close QPC 2, the same QPC gate trace as in Fig. 4.7(b) will be observed, i.e., the conductance to **D2** is reduced proportional to the transmission of QPC 2. What happens

is, that at first all edge channels are completely transmitted at the QPCs and go to **D2**. When the transmission of QPC 2 is reduced at first the inner edge channel is partially, and then completely reflected and the electrons travel into the inner ohmic contact **D1** and their conductance is lost for **D2**. When QPC 2 is fully closed, all edge channels coming from **S** are led into **D1**, the edge channels ending in **D2** originate then from **D1**, which is grounded and no net current can be detected at **D2**. The same happens when leaving QPC 2 open and closing QPC 1, only that the path of the net current is different. The electrons reflected at QPC 1 go along the upper interferometer arm, then are transmitted at QPC 2 and into **D1**. This has a small constraint, because for this **D1**, which is the inner ohmic contact, has to be perfect. However, due to its small size this is not the case. Due to a finite resistance between a contact and the 2DEG there is always a small (depending on the contact quality and size) current that passes the inner, small ohmic contact and moves on to the larger ohmic of **D2**. Thus, when closing one of the QPCs the conductance does not drop to completely zero, but stays at a very small value, which still can be resolved, but can be usually neglected. Worth mentioning is the fact, that the total conductance from source **S** to the drains **D1** and **D2** stays constant, only the distribution between the two drains varies. Operating only QPC 0 will also lead to its transmission characteristic, but in this case one changes the total conductance by disconnecting the source from the sample.
As explained before, QPCs 1 and 2 operate the Mach-Zehnder interferometer itself, here especially it is the transmission of QPC 1 that defines if the upper or lower interferometer arm is preferred, whereas QPC 0 determines whether and how strong the edge channels passing the interferometer are biased from the source. Adjusted to integer transmissions the number of biased edge channels is defined, at non-integer values one specific edge channel is transmitted only partially and will thus also introduce noise into the system. The latter will be subject in chapter 6. At filling factors larger than 1.5 more than one edge channel is present and one might think of doing interference experiments with either of these channels. Throughout this thesis only the outer edge channel is used for the interference. To my knowledge there is no report of a similar experiment operating an inner edge channel for the interference. So QPCs 1 and 2 are always set to transmissions between 0 and 1 and the inner channel is reflected completely.
With this knowledge of the operating mode of the Mach-Zehnder interferometer we can turn to the interference experiments. For this we start with the simplest situation, i.e., we adjust QPC 0 to only and fully transmit the outer edge channel at an arbitrary magnetic field with filling factor between 1 and 2. Then QPCs 1 and 2 are adjusted to a transmission between 0 and 1 and we measure the interference oscillations in the conductance by either varying the magnetic field, or the modulation gate voltage. At the source a small ac excitation voltage of 1 μV is applied, but no dc bias. Examples of this can be seen in Fig. 5.2(a) for a field sweep and (b) for a modulation gate sweep. In both cases we see a clear sinusoidal behavior as illustrated with the fit curve (red line). This is exceptional

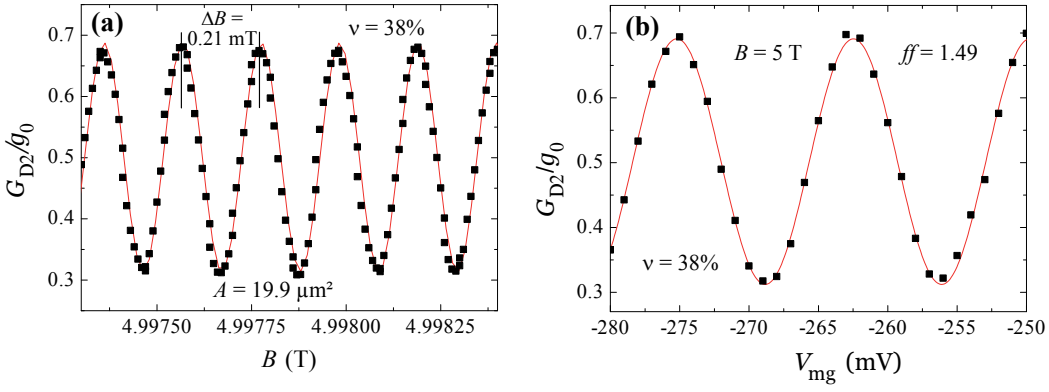

Figure 5.2.: Aharonov-Bohm oscillation in a MZI at $B \approx 5\,\mathrm{T}$ ($ff \approx 1.5$). In (a) the phase shift is realized by changing the magnetic field and in (b) by changing the modulation gate voltage V_{mg}. Additional to the visibility by taking maximum and minimum value, one can get another information from the B-sweep, that is the area of the interferometer using $\Delta\varphi = \frac{e}{\hbar}\Delta B A$. QPC setting: $\mathcal{T}_0 = 1$, $\mathcal{T}_1 = \mathcal{T}_2 = 0.5$.

for an Aharonov-Bohm interferometer, because usually each arm carries multiple electron modes, which results in a beating with higher harmonics. However, interferometers in the quantum Hall regime carry only a single mode because of the 1D character of the edge channels. From such kinds of curves one can get averaged maxima and minima and calculate the visibility using Eq. 2.72. Aharonov-Bohm oscillations pass through one period when the flux changes by h/e, this way one has experimental access to the area of the interferometer by looking at the period of the magnetic field oscillations via $\Delta\varphi = \frac{e}{\hbar} A \Delta B$. The data shown in Fig. 5.2 was recorded with a sample of type B and the calculated area of $\sim 20\,\mu\mathrm{m}^2$ fits the expected value very well. Varying the flux by changing the magnetic field has the disadvantage that it is hard to access experimentally such small B-field changes at an overall large field. Additionally, changing the magnetic field changes slightly the filling factor, i.e., the Landau levels and thus the barrier heights of the QPCs and the structure of resonances which might change transmission drastically. Usually, oscillations are recorded this way only to measure the active area of the interferometer, otherwise one changes the phase by sweeping the modulation gate voltage.

Dependence of the visibility on QPC transmission

A basic feature of the Mach-Zehnder interferometer is the $\sqrt{(\mathcal{T}(1-\mathcal{T}))}$ dependence of the visibility on the QPC transmission as predicted from relation Eq. 2.73, when the second QPC is set to half transmission. Fig. 5.3(a) shows a measurement of a sample

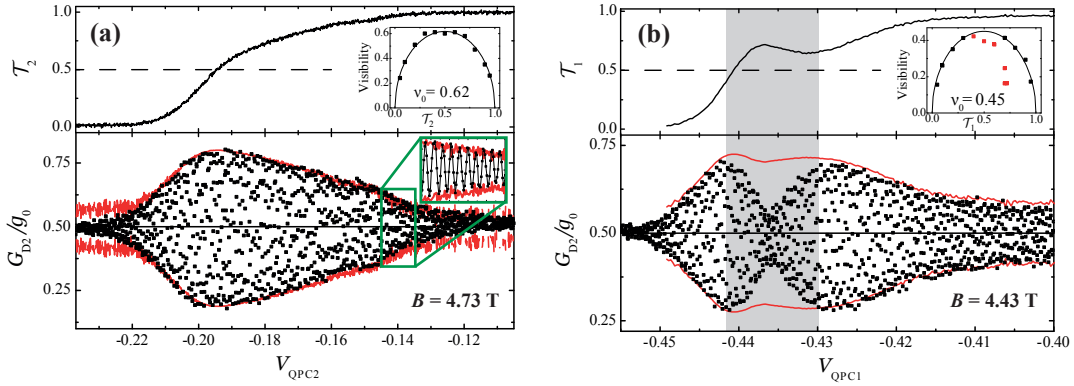

Figure 5.3.: (a) A QPC gate trace without resonances is depicted in the top panel. In the lower panel the (fast) oscillations vs. $V_{\mathrm{QPC}\,1}$ (black squares, see also zoom-in in green frame) are depicted, together with the expected amplitude (red line), calculated from the transmission. The inset shows the visibility vs. QPC transmission. This QPC shows the $\sqrt{(\mathcal{T}(1-\mathcal{T}))}$ dependence. In (b) the same is illustrated for the case where there is a resonance in the QPC characteristic. Here, we see a strong suppression of visibility far below its expected value, as calculated from the transmission (gray-shaded region). Corresponding points are red in the inset.

of type A, the top panel shows the gate trace of QPC 2, the lower panel a measurement of conductance when QPC 1 is set to half transmission and $V_{\mathrm{QPC}\,1}$ is varied. While sweeping slowly the QPC voltage, a fast oscillating, saw tooth voltage is applied to the modulation gate with a frequency generator. A series of fast oscillations around the average value $0.5g_0$ with an amplitude that depends on the QPC transmission is observed (Fig. 5.3(a), lower panel). The envelope of this set of points (so their maximum and minimum values) gives the visibility vs. QPC gate voltage. Fig. 5.3(a) shows clearly that the amplitude and thus the visibility is zero for $\mathcal{T}_2 = 1$ and 0 and there is a maximum around $\mathcal{T}_2 = 0.5$. Using the simplified version of Eq. 2.73

$$\nu = \nu_0 \cdot 2\sqrt{(\mathcal{T}(1-\mathcal{T}))}, \tag{5.1}$$

one can determine the theoretical expected envelope. Here, the factor $\nu_0 < 1$ is the maximum visibility at zero bias and accounts for some, yet, not mentioned dephasing and is the maximum visibility at $\mathcal{T} = 0.5$. The inset in Fig. 5.3(a) displays this $\nu(\mathcal{T})$, together with the experimental visibility extracted from the envelope in the lower panel of this figure. The red curve in the lower panel is the calculated value of maximum and minimum according to the QPC characteristic and Eq. 5.1. The small deviations from theory in Fig. 5.3(a) close to $\mathcal{T}_2 = 1$ and especially 0 arise, because here the visibility is very sensitive to the QPC transmission and thus noise and small offsets show up strongly. Apart from this unavoidable systematic limitations to the theory, there can also

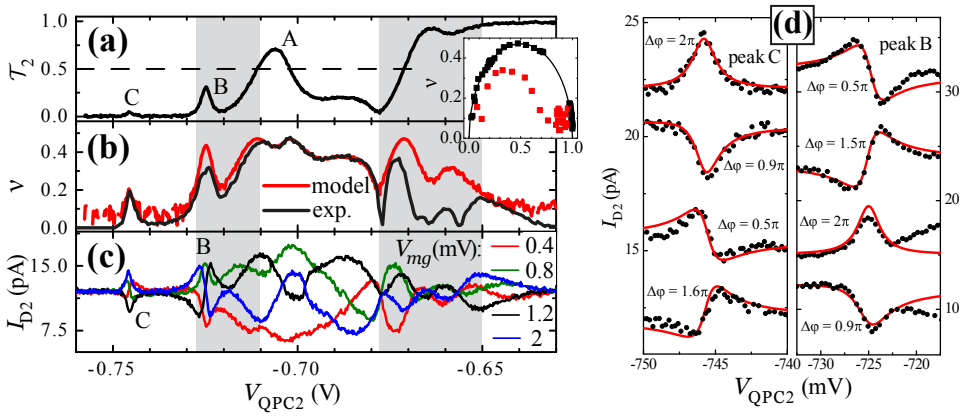

Figure 5.4.: Coherent transport through a localized state: The gate trace of QPC 2 shows a number of resonances in the zero bias transmission (a) at $B = 4.6$ T, marked with "A", "B" and "C". The corresponding visibility (b) mostly follows Eq. 5.1, except in the gray-shaded regions. The inset shows $\nu(\mathcal{T}_2)$ for theory and experiment, with the experimental points in red from the gray-shaded regions. The current I_{D2} vs. V_{QPC2} for fixed V_{mg} in (c) reveals the transmission phase behavior through the localized states, the so-called Fano resonances. A zoom-in on the Fano resonances of peaks "B" and "C" (dots) is depicted in (d), together with fits to Eq. 5.3 (red line).

be intrinsic ones. As mentioned above many QPC gate traces show resonances at high magnetic fields (see Fig. 4.7) and an emergence of these resonances due to localized states is very often accompanied by additional decrease or even break down of coherence as can be seen in Fig. 5.3(b). Here one can clearly see that the visibility decreases much more than changing the transmission of the QPC would suggest (highlighted with the gray shaded region). Red dots in the inset are visibility measurements in this region. There exists no extensive study to find the origin of this behavior. One simply tries to avoid such resonances as much as possible in most cases, also because of the in Sec. 4.2.2 stated strong bias dependence of these resonances.

Apart from the inconveniences that these resonances bring for measurements of the interferometer "alone", they give the possibility to investigate coherent transport through these localized states. This was investigated in detail in Ref. [72] (and the discrepancy to $\sqrt{(\mathcal{T}(1-\mathcal{T}))}$ in [69]). Here I only want to briefly review the basic experiment to learn more about the localized states. Aharonov-Bohm interferometers with a quantum dot embedded in one interferometer arm were already studied intensively before [48, 73–75]. In this experiment the localized state was produced inadvertently due to the random background potential of the semiconductor heterostructure between or near the tips of QPC 2 and, as already mentioned above, it is more likely an antidot than a usual quantum dot. Though close to the point where the two electron paths interfere,

this dot will belong to only one arm of the interferometer and thus lead to the known shift of the electron wave function phase $\theta(t_{\mathrm{QD}})$ of π. In previous works this was measured by recording many $G(B)$ curves of AB oscillations for different QD plunger gate voltages and then extracting the phase evolution from this. However, in this experiment it is possible to directly measure the phase change of the dot while crossing its resonance. In Fig. 5.4(a) the gate trace of QPC 2 is depicted. Clearly several resonances and dips can be seen implying a well developed resonant state. Three pronounced peaks are labeled "A", "B" and "C". In (b) the measured visibility $\nu(V_{\mathrm{QPC\,2}})$ (QPC 1 was set to half transmission) is compared to Eq. 5.1 and regions where the coherence is disturbed are highlighted in gray (inset shows $\nu(\mathcal{T}_2)$ with black squares following the model and red squares from the gray shaded regions). There is no direct connection between a deviation from Eq. 5.1 and a resonance, that means, not at every gate voltage where a resonance appears the visibility is diminished. However, one can say that whenever there are resonances in a QPC characteristic, there might be discrepancies to the simplified model. The curves in Fig. 5.4(c) were measured similar to the gate trace in (a), only with QPC 1 set to $\mathcal{T}_1 = 0.5$ and different constant V_{mg}. This represents the coherent part of the conductance while changing the QPC 2 gate voltage, which on one hand defines the visibility by the QPC transmission, but on the other hand also the shifting of the levels of the dot. Transport through a quantum dot can be described be the Breit-Wigner formula

$$t_{\mathrm{QD}} = |t_{\mathrm{QD}}|e^{i\theta} = \frac{i\Gamma/2}{E - E_n + i\Gamma/2}, \tag{5.2}$$

with E_n being the energy of the selected state. From this we also get $\theta(t_{\mathrm{QD}}) = \arctan\left(\frac{2}{\Gamma}(E - E_n)\right)$ and together with $|r_{\mathrm{QD}}|^2 = 1 - |t_{\mathrm{QD}}|^2$ we can rewrite Eq. 2.71 for the coherent current to

$$I_{\mathrm{D2}} \propto |t_{\mathrm{QD}}|^2 \cos(\Delta\varphi + \theta(t_{\mathrm{QD}})). \tag{5.3}$$

These are the so-called Fano resonances, which can be only seen for QPC resonances "B" and "C" where the QPC transmission changes slowly with energy ($V_{\mathrm{QPC\,2}}$). In this case Fano resonances describe the interference of the localized state with the continuum of the electrons which are scattered at it. The Fano resonances can be clearly seen in Fig. 5.4(c) at the positions of resonances "B" and "C". In Fig. 5.4(d) fits to Eq. 5.3 are shown as red lines. The only fitting parameter was the Aharonov-Bohm phase $\Delta\varphi$, the parameter Γ was determined by analyzing the width of the resonances in the QPC transmission.

With this experiment we could not find a reason for the visibility break down connected to the localized state, but we could show that a Mach-Zehnder interferometer is most suitable to investigate coherent transport through a quantum (anti-)dot and may be a good alternative for a non-dispersive read-out of the dot by its reflection phase instead of the usually used charge detection by a QPC.

5.2. Decoherence at finite temperatures

So far we introduced dephasing only by the prefactor ν_0 which is a constant for a given temperature, interferometer size, magnetic field and any connection to the environment at zero bias voltage. In this section we give priority to its dependence on temperature and its connection to the size L of the interferometer.
When investigating the temperature dependence at such low values ($20 - 50\,\mathrm{mK}$) one faces the difficulty to know the actual electron temperature only with limited accuracy. System thermometers of the cryostat (here rubidium oxide resistors) may show a different temperature than the electron temperature inside the sample. Since the visibility falls to below $1\,\%$ already at $T = 100 - 200\,\mathrm{mK}$ it is essential to know the electron temperature in order to verify the exact evolution below $T = 100\,\mathrm{mK}$.
One possibility to directly measure the electron temperature in the same measurement run is to measure the Johnson-Nyquist (thermal) noise. This was achieved with the noise measurement setup of the group of Prof. Kensuke Kobayashi at the chair of Prof. Teruo Ono, Institute for Chemical Research, Kyoto University, Japan. The setup is described in detail in Ref. [76] and is implemented in a dilution refrigerator (Kelvinox 400 from Oxford). It consists of special filters to decouple the sample from noise at room temperature, a resonant LC circuit ($f_0 = 3\,\mathrm{MHz}$), and a preamplifier at 1 K to amplify the noise signal. As shown in Fig. 5.5(a) it was possible, in this setup, to measure Aharonov-Bohm oscillations with a maximum visibility of $50\,\%$ in a Mach-Zehnder interferometer of type A with an arm length of $L \approx 7\,\mu\mathrm{m}$, whereas a sample of the same type and size reached $65\,\%$ in the setup up described in chapter 3. Additionally at a magnetic field of $B = 5\,\mathrm{T}$ the e^2/h plateau of a single QPC was used to measure thermal noise for different system temperatures to confirm the electron temperature [see Fig 5.5(b)]. After this callibration of system temperature to electron temperature the QPCs were adjusted to operate the Mach-Zehnder interferometer and for each temperature the visibility was recorded. The result of this measurement for the magnetic fields $B = 5\,\mathrm{T}$ and $B = 4.5\,\mathrm{T}$ can be seen in Fig. 5.5(c) in a semi-logarithmic scale. For temperature $T > 80\,\mathrm{mK}$ we see an exponantial decay that fits well $\exp(-T/T_0)$, where T_0 is a characteristic temperature describing the decay, as reported previously in Mach-Zehnder interferometers [69, 77, 78] and other Aharonov-Bohm interferometers [79–83].

However, on top of this asymptotic behavior for high temperatures a saturation for small T is found which follows

$$\nu_0(T) \propto \left(1 + \frac{T}{T_0}\right) e^{-T/T_0}. \tag{5.4}$$

This expression was already theoretically discussed in Ref. [85] in terms of the chiral Luttinger liquid, in this case for integer and fractional filling factors. One problem that occurred for the mere exponential decay in Mach-Zehnder interferometers is that

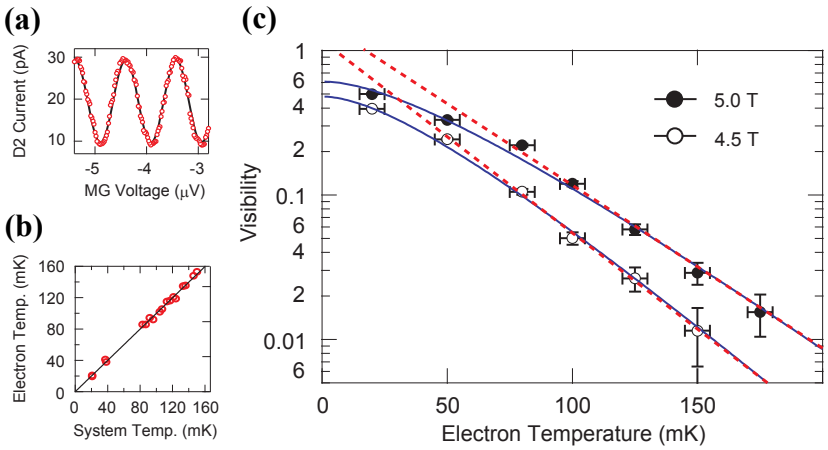

Figure 5.5.: (a) Conductance oscillations at 20 mK with sinusoidal fitting. (b) Calibration of system temperature with electron temperature determined by Johnson-Nyquist noise. (c) Visibility for various temperatures and two magnetic fields with exponential fit (dashed red line) for the high bias regime and $(1 + T/T_0)\exp(-T/T_0)$ behavior (blue line) fitting the whole curve. The characteristic temperature for $B = 5\,\mathrm{T}$ is $T_0 \sim 30mK$. (Reproduced from Ref. [84])

an extrapolation to $T = 0$ would lead to a visibility larger than 100 %, in contrast to Eq. 5.4 which leads to reasonable values for the highest visibility. This can be seen in Fig. 5.5(c) and 5.6. Fig. 5.6 shows measurements performed in the cryostat described in chapter 3, where there is no possibility to cross-check the electron temperature, for Mach-Zehnder interferometers of three different sizes L. Also here a saturation for low T can be seen, but cannot be fully explained by Eq. 5.4. The fitting to this formula was done only by the high T points. The reason for this is that it was not possible to verify the electron temperature and the system temperature undershoots the electron temperature. Relying on the validity of Eq. 5.4 we can thus estimate the electron base temperature in this cryostat to be $T \approx 30 - 33\,\mathrm{mK}$.

The characteristic temperature T_0 of the asymptotic exponential decay is related to the arm length of the interferometer [77]. This is true for any interferometer operated in the integer quantum Hall regime [79]. In Ref. [77] a reciprocal relation between T_0 and L was found and theoretically discussed in Ref. [31]. This is also found in our experiment and shown in the inset of Fig. 5.6 for three Mach-Zehnder interferometers with arm lengths $L = 6$, 9 and $14\,\mu\mathrm{m}$ close to $ff = 1.5$. This way one can relate T_0 with a dephasing length l_φ via

$$\nu_0 = \nu_0' e^{-2L/l_\varphi(T)} = \nu_0' e^{-T/T_0(L)} \quad \text{with} \quad l_\varphi(T) \propto 2LT_0T^{-1}. \tag{5.5}$$

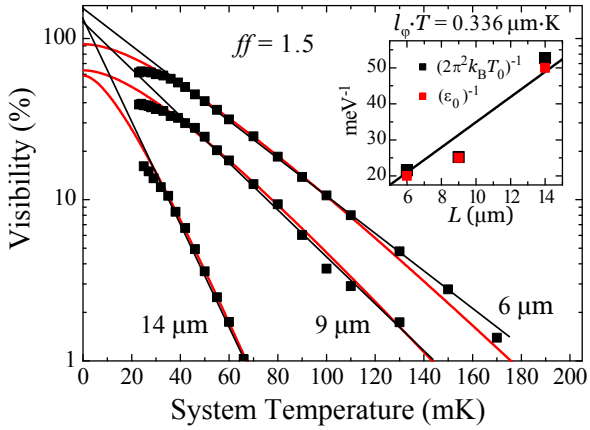

Figure 5.6.: Visibility decay with temperature for interferometers of different sizes $L = 6\,\mu$m, $9\,\mu$m and $14\,\mu$m at $ff = 1.5$. Black lines are high temperature exponential decay asymptotics, red lines are fits with Eq. 5.4. The inset shows the inverse of the characteristic temperature $(2\pi^2 k_B T_0)^{-1}$ and of the characteristic energy ε_0^{-1}. The latter is the characteristic energy $\varepsilon_0 = 2eV_0$ of Eq. 2.74 and its connection to T_0 and L will be described in the next section. Both parameters change linear with interferometer size L. The coherence length is estimated to be $l_\varphi \approx 11\,\mu$m at $T = 30\,$mK. It decreases with increasing temperature.

Here, ν_0' is the visibility for $T \to 0$, which means $l_\varphi \to \infty$. Thus, from the slope of the curve in the inset of Fig. 5.6 one can deduce a coherence length $l_\varphi \approx 11\,\mu$m at $T = 30\,$mK.

In Ref. [60] and [86] a temperature dependence $(\pi k_B T/E_c)/\sinh(\pi k_B T/E_c)$ is proposed with E_c being an asymmetry energy with $E_c = \hbar v/\Delta L$ where ΔL is the length difference between the two interferometer arms. Fits with this formula resemble the experimental curves. The extracted fitting parameter E_c would then imply a arm length difference of a few pikometer. Though the interferometers are built to have identical arm lengths, it is rather likely that they show a ΔL of nanometers, up to a micrometer. In addition, this theory does not explain the experimentally observed relation of the characteristic parameter (in this case E_c and not T_0) to the total size of the interferometer L and thus to a coherence length l_φ.

The characteristic temperature T_0 and thus the coherence length l_φ depend also on the magnetic field as can be seen in Fig. 5.5(c). The discussion of this topic will be covered in Sec. 5.4.

5.3. Finite bias visibility

After the previous section explained dephasing at zero bias I now will show the effect of a finite dc bias voltage on the coherent differential conductance and the visibility. In Sec. 2.6 a simple example of Gaussian phase noise and how this leads to a central lobe and single side lobes in the differential conductance and visibility was shown. In the first part of this section experimental results of this kind of lobe structure are presented. The second part deals with the phenomenon of a lobe structure with multiple side lobes. This result was puzzling in the beginning and will be clarified in the course of this chapter.

5.3.1. Filling factor one - single side lobes

A situation, where one expects least influence on the coherence of other effects and a bias behavior es described in Sec. 2.6, is when there is only one edge channel present. This is the case at a magnetic field with $ff \leq 1.5$, although close to $ff = 1.5$ there is partly a resistive bulk inside the sample which will influence somehow the response of the Mach-Zehnder interferometer when also this part is biased. To avoid this we use again QPC 0 to transmit only and fully the outer edge channel which we use for the interference. The experimental situation in the following is $\mathcal{T}_0 = 1$ and $\mathcal{T}_1 = \mathcal{T}_2 = 0.5$ and the temperature is set to the base temperature of the cryostat, i.e., $T_{electron} \approx 30\,\mathrm{mK}$. To record the coherent transport for finite dc bias we set to a magnetic field, i.e., filling factor $1.5 > ff > 1$, and add to the small ac excitation voltage dV_{ac}, used for the (differential) conductance measurement dI/dV_{ac}, a dc voltage V_{dc}. Then this dc voltage is swept and the conductance recorded for a variety of fixed modulation gate voltages. The collected raw data for a sample of type B at $B = 5\,\mathrm{T}$ ($ff = 1.49$) is depicted in Fig. 5.7(a) as a gray scale 2D plot and in (b) as an overlay of all the V_{dc} traces. Fig. 5.7(a) reveals a chess pattern of three columns of squares representing the lobes. For larger dc voltages any oscillations are fading. The visibility is extracted by defining an envelope to a plot as in Fig. 5.7(b). From this we get $G_{max}(V_{\mathrm{dc}})$ and $G_{min}(V_{\mathrm{dc}})$ and thus arrive at $\nu(V_{\mathrm{dc}})$ according to Eq. 2.72. This is shown in Fig. 5.7(d) top panel. For a lobe structure not only the bare amplitude or visibility is important, but additional information lies in the relative phase evolution, which can already be guessed in Fig. 5.7(a). To exactly evaluate the phase evolution, especially in cases where oscillations are small in the raw data and the detailed behavior is hard to recognize, we look at modulation gate traces in the raw data [Fig. 5.7(c)], which are AB oscillations for a fixed dc bias voltage. These are then fitted with a sine function $G(V_{\mathrm{mg}}) = G_{average} + G_{osc}\sin(2\pi V_{\mathrm{mg}}/V_P + \Delta\varphi)$. This is done at first at zero bias as in Fig. 5.2(b). Fitting parameters, apart from the average of the oscillations $G_{average}$ and the amplitude G_{osc}, are especially the period of the oscillations V_P and the phase $\Delta\varphi(V_{\mathrm{dc}}) = \varphi(0) - \varphi(V_{\mathrm{dc}})$. The period V_P is only fitted

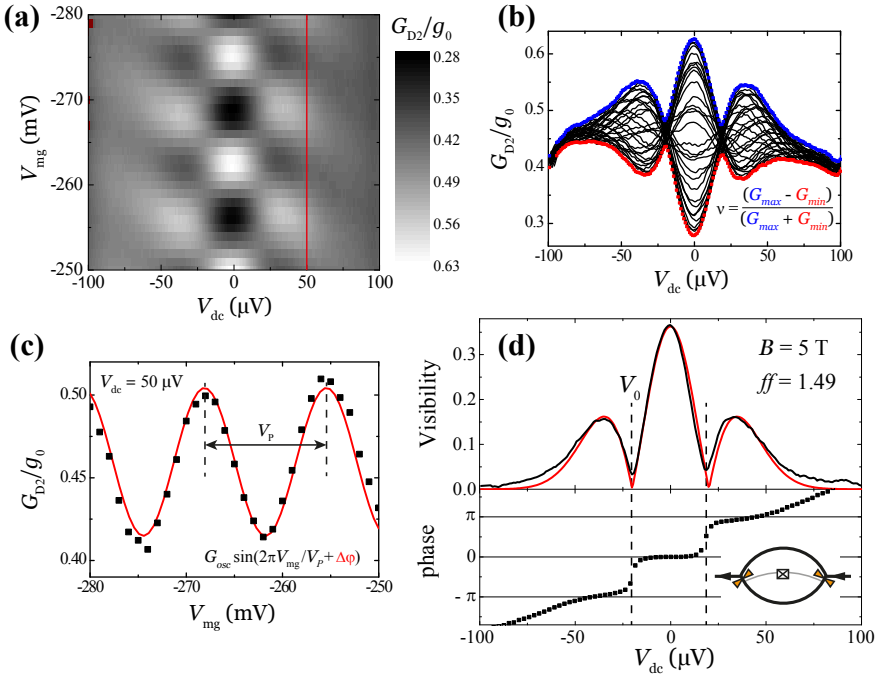

Figure 5.7.: Data for a sample of type B at $T \approx 33\,\mathrm{mK}$ and $B = 5\,\mathrm{T}$ ($ff = 1.49$). Differential conductance traces are measured for various modulation gate voltages. (a) Shows raw data as a gray scale 2D plot. (b) Raw data traces plotted vs. V_{dc}. Envelope (blue: maximum; red: minimum) yields the visibility in (d) top panel. (c) A modulation gate trace [red line in (a)] with sinusoidal fitting. The phase $\Delta\varphi$ for certain V_{dc} is plotted in (d) bottom panel. The inset shows a sketch of the interferometer edge channel (black) and QPCs (orange). In (d) top panel is the resulting visibility vs. V_{dc}, the red line shows a fit of the model used in Fig. 2.16.

for zero bias and then kept constant to lock in to this frequency and avoid any distortion of noise when the oscillations are small for larger bias, which will also alter the relative phase. The extracted $\Delta\varphi(V_{\mathrm{dc}})$ is shown in Fig. 5.7(d) bottom panel.
Actually, Fig. 5.7(a) and (d) contain the same information, but in (d) the information for amplitude and phase are apportioned. We see a central lobe with a node at V_0 accompanied be a single lobe on each side. As expected for such a lobe structure the phase is constant inside the lobes and shifts by π at the nodes. A phase drift for large bias as seen here can happen sometimes and the exact origin is unclear, but might be due to the nonlinearity which can also be seen in (b) by the average conductance at larger bias.
This single side lobe behavior was seen in previous works on Mach-Zehnder interferometers [62,69,87], mainly close to $ff = 1$, and can be explained with a phenomenological model as discussed in Sec. 2.6. A fit to this model is displayed in Fig. 5.7(d) as red line.

The only fitting parameters are ν_0 and the characteristic energy $\varepsilon_0 = 2eV_0$, which is the width of the central lobe. The first is controlled by temperature and size L as explained in the previous section. As we can see in the inset of Fig. 5.6 the characteristic energy ε_0 is proportional to the characteristic thermal energy $k_\mathrm{B}T_0$ and thus also dependent on the interferometer size as $\varepsilon_0 \propto 1/L$. We can assume that the mechanism of dephasing is the same in both cases. Though there is so far no excepted microscopic theory to explain this dephasing, yet, one can imagine any inelastic scattering, that increases with temperature, size and bias voltage. Most theories propose that $\varepsilon_0 \approx \hbar v'/L$ [31, 86, 88, 89], where v' is the velocity of the propagating excitation in the interferometer. Its behavior for a variety of samples and interferometers was investigated and compared in Ref. [79]. Since the mentioned theories deal with the subject to explain multiple side lobes with different approaches, I will discuss this bias dependence in the following sections and will give in this context a short comparison of the theories in Sec. 5.4. Thus, I will not go into detail here and go on with a rather phenomenological discussion.
In all theories the velocity v' is the Fermi velocity v_F, which is only slightly modified by the particular electron-electron interaction of the theory. Thus, each theory gives a reasonable magnitude of order of the characteristic energy $\varepsilon_0 \approx 10 - 20\,\mu$eV. The proportionallity factor between ε_0 and $k_\mathrm{B}T_0$ is close to $2\pi^2$, which is expected from Levkivskyi et al. [85]. As an overview of the energy scales and the connection between ε_0 and $k_\mathrm{B}T_0$ see also App. B.

5.3.2. Filling factor two

The finite bias behavior changes significantly when operating the Mach-Zehnder interferometer at $2 > ff > 1.5$. In that case also an inner edge channel is developed and an edge channel situation as described in Sec. 2.3.3 arises. The first part of this subsection deals with $\mathcal{T}_0 = 1$, and the second with $\mathcal{T}_0 = 2$, while the other QPCs are set to half transmission. The cryostat is set to base temperature.

Applying bias to one channel - multiple side lobes

The filling factor and the setting of QPC 0 leads to the state, that there are two present edge channels developed in the sample, but the inner edge channel is cut from bias and grounded when passing the interferometer arm and the voltage V_dc is only applied to the outer edge channel [see inset of Fig. 5.8(c)].
We collect data as in the previous section and an example for a sample of type B at a filling factor of ≈ 1.75 ($B = 4.3\,$T) is shown in Fig. 5.8(a) as raw data and (c) as the extracted visibility and phase evolution. A chess pattern shows up as in the case for one edge channel, with the difference that not only three columns of squares can be seen, but

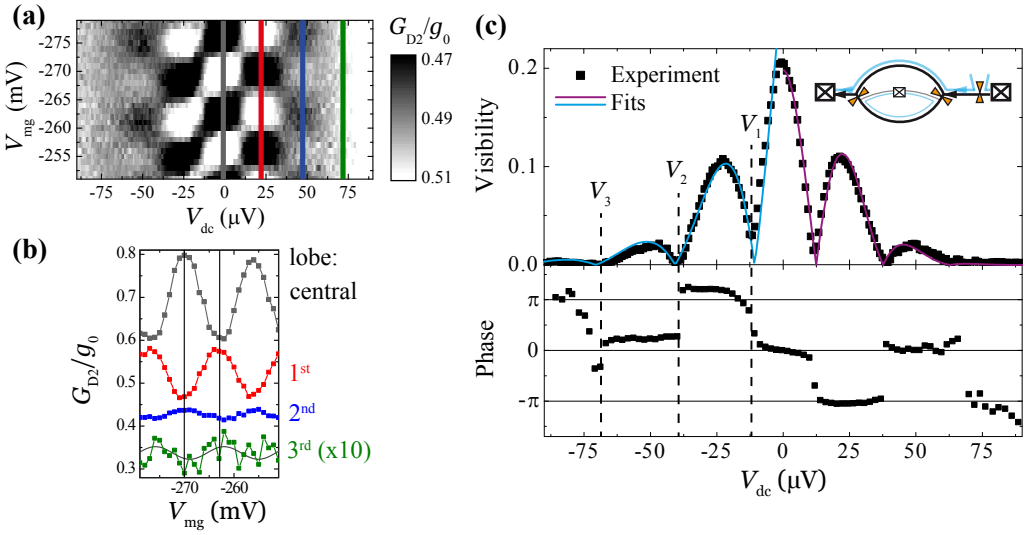

Figure 5.8.: Data for sample B at $T \approx 33\,\mathrm{mK}$ and $B = 4.3\,\mathrm{T}$ ($ff = 1.75$). (a) shows raw data as a gray scale 2D plot. The chess board pattern reveals multiple side lobes. (b) depicts modulation gate traces of maximal oscillations of each lobe [colored lines in (a)]. Residual oscillations of a third lobe can be fitted with a sinus with fixed frequency of zero bias oscillations. In (c) top panel is the resulting visibility vs. V_{dc}, the purple line shows a fit of Eq. 5.6, cyan line to Eq. 5.8. Node positions are marked as V_1, V_2 and V_3. Energy scales from fits are: $\varepsilon_L \approx 27\,\mu\mathrm{eV}$ and $\varepsilon_0 \approx 21\,\mu\mathrm{eV}$

an additional column on each side indicating an additional side lobe before the overall visibility decays to very small values for larger bias voltages V_{dc}. This can again be seen in the phase evolution with roughly constant phase inside lobes and slips by π at nodes. Furthermore, the exact analysis by sinusoidal fitting of modulation gate traces to gain phase information reveals an additional jump at $V_{\mathrm{dc}} \approx 70\,\mu\mathrm{V}$, i.e., an additional lobe which is buried in noise in the visibility. Fig. 5.8(b) depicts AB oscillations at lobe maxima. It nicely shows how the maximum amplitude is decreasing for higher order lobes and the phase difference of π between succeeding lobes. The bottom green curve shows a ten times increased signal of a modulation gate trace at $V_{\mathrm{dc}} = 73\,\mu\mathrm{V}$. The residual AB oscillations in the measurement noise can still be extracted and analyzed by the mentioned sinusoidal fitting with the fixed frequency of the zero bias oscillations. This clearly shows that there are multiple side lobes, i.e., multiple oscillations vs. V_{dc}, that are suppressed approximately exponentially for large bias. The widths of the side lobes are the same and are usually in the range of $20 - 50\,\mu\mathrm{V}$. The width of the central lobe is often slightly smaller than that of the side lobes ($0 - 30\,\%$). This behavior with multiple side lobes was first shown in Ref. [87] and theoretical explanations are still under discussion. As I will further elucidate in this chapter, experimental facts point

towards one theory. In the case of a lobe structure with a single node, the node voltage was denoted as V_0 and was related to a characteristic energy ε_0. Important energies in the case of multiple nodes, i.e., multiple side lobes shall be discussed in the following. For this purpose the positions of the mth node will be denoted as V_m, so $m \geq 1$.
Since explanations and theories are still unclear for the lobe structure with multiple side lobes and there are no analytical formulas to fit and analyze the experimental data, two phenomenological formulas are now discussed. A formula which was already used in previous works [71, 79, 84] is

$$\nu(V_{\mathrm{dc}}) = \nu_0 |\cos(\pi e V_{\mathrm{dc}}/\varepsilon_L)| \exp\left[-(eV_{\mathrm{dc}})^2/2\varepsilon_0^2\right]. \tag{5.6}$$

This formula is based on two assumptions. One is that the dephasing due to inelastic scattering along the interferometer arms leads to the envelope of $exp(-\alpha V^2)$ with a certain characteristic energy ε_0 similar to Eq. 2.74. The second one is that there is a perfectly sinusoidal conductance oscillation with a maximum at $V_{\mathrm{dc}} = 0$, which results in the cosine term and ε_L is the energy scale defining the periodicity. In Fig. 5.8(c) a fit to this formula is shown as purple line. The matching is sufficient, especially for small voltage bias, only at larger bias the node positions are not perfectly correct, because the central lobe can be up to 30% smaller in width than the side lobes.
Another phenomenological formula for the visibility starts with the coherent current

$$I_{coherent,max} \propto \exp\left(-\frac{e}{\varepsilon_0}V_{\mathrm{dc}}\right) \sin\left(\frac{\pi e}{\varepsilon_L}V_{\mathrm{dc}}\right). \tag{5.7}$$

The pure exponential decay is also described by a characteristic energy ε_0. However, it is only valid for large bias voltages $eV_{\mathrm{dc}} > k_{\mathrm{B}}T \sim 3\,\mu$eV, when the energy introduced by the voltage exceeds the thermal energy. In this case we start with the assumption of a sinusoidal coherent current. Thus, to get the visibility ν in dI/dV we need to differentiate and arrive at

$$G_{coherent,max} \propto \exp\left(-\frac{e}{\varepsilon_0}V_{\mathrm{dc}}\right)\left[\frac{\pi e}{\varepsilon_L}\cos\left(\frac{\pi e}{\varepsilon_L}V_{\mathrm{dc}}\right) - \frac{e}{\varepsilon_0}\sin\left(\frac{\pi e}{\varepsilon_L}V_{\mathrm{dc}}\right)\right]. \tag{5.8}$$

When converting this to a visibility $\nu = |G_{coherent,max}|$, this looks almost as Eq. 5.6 with an exponential decay, despite the fact that there is no single cosine term, but a sum of trigonometric functions with the same argument. Effectively this leads to an oscillating function with the same period, but all zeros are shifted by a constant value to smaller voltages, i.e., the lobe widths of all side lobes are the same, only the central lobe width is reduced. In Fig. 5.8(c) the fit to Eq. 5.8 is shown as cyan line. For this purpose the points at low voltage bias $V_{\mathrm{dc}} < k_{\mathrm{B}}T/e$ are neglected. Then the agreement is reasonable, especially the node positions are perfectly reproduced. The poor fitting for small voltages might be even expected, because here dephasing should be dominated by thermal fluctuations.

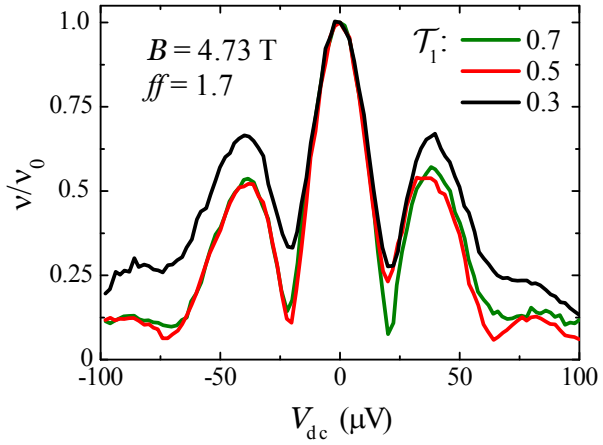

Figure 5.9.: Lobe structure for sample A at $T \approx 33\,\mathrm{mK}$ and $B = 4.73\,\mathrm{T}$ ($ff = 1.7$). The visibility is normalized to the zero bias value ν_0 to omit the effect of the $\sqrt{\mathcal{T}(1-\mathcal{T})}$ behavior. Lobe structures are displayed for three different transmission of QPC 1, which defines preference of upper or lower arm. Apart from the maximum visibility the lobe structure stays the same. Important parameters: $V_1 = 22\,\mu\mathrm{V}$, $V_L = 48\,\mu\mathrm{V}$.

Until now, there is no full theory, that can reproduce the lobe structure in all details and in all its various characteristics, which I will continue to describe below. Thus, it is hard to decide which phenomenological formula is more adequate. While Eq. 5.6 gives a nice overall fit it fails to reproduce the node positions at larger bias accurately and to account for the fact, that the central lobe can be slightly smaller. On the other hand Eq. 5.8 recreates nicely the node positions, especially at large voltage bias, but cannot be applied close to zero bias. To conclude, Eq. 5.6 is used whenever the central lobe has (almost) the same width as the side lobes and a comparison of both energy scales ε_0 and ε_L is needed (as in the next section). Both formulas have in common, that the width of the side lobes gives the energy scale ε_L, thus apart from fitting to any formula this energy is in most other cases obtained by the voltage $V_L = V_{m+1} - V_m = \varepsilon_L/e$. Unfortunately a similar method cannot be applied to determine the second energy scale ε_0, which is responsible for the dephasing with V_{dc}.
These energy scales do not depend on the transmission of QPC 1 $\mathcal{T}_1$, i.e., whether the upper or lower interferometer arm is preferred. Fig. 5.9 shows that the lobe structures for different $\mathcal{T}_1$ coincide very good, after normalization to the corresponding ν_0, which is governed by Eq. 2.73.
Although there is no ascertained theory to express the exact characteristic of the multiple lobe structure, I want to give a short overview of the basic theories on this topic with an emphasis on the most promising theory.
In a fermionic picture, i.e. where it is neglected that electrons form a Luttinger liquid,

multiple lobes are explained with the increasing number of electrons in an interferometer arm due to the applied voltage [88, 89]. Intra-channel Coulomb interaction of these non-equilibrium electrons leads to a phase shift with bias voltage, which then leads to the multiple side lobes. The shot noise of these electrons, being partially transmitted/reflected at QPC 1, leads to the decaying envelope. In Ref. [90] the bosonization of the Luttinger liquid is used, together with three possible intra-channel interaction potentials between pairs of electrons (at coordinates x and x'). These are: (I) a constant charging energy $U(x, x') = g$, as in a quantum dot; or potentials which vary with electron distance, being either of an (II) exponential dependence $U(x - x') = ge^{-\alpha|x-x'|}$, or of (III) Coulomb type $U(x-x') = g_c/\sqrt{(x - x')^2 + a_c^2}$. Here, the constants are the interaction strengths $g_{(c)}$, which is scaled with $\gamma_{(c)} = g_{(c)}/2\pi\hbar v_\mathrm{F}$; the interaction range $1/\alpha$ in case (II), and a short-distance cutoff $a_c \ll L$ in case (III). When there are two electrons in the same interferometer arm at the same time for the time τ, an additional, potential dependent phase $e^{-iU\tau/\hbar}$ is accumulated. Regardless of the exact interaction, any of them leads to a lobe structure with multiple side lobes, which decay for large bias, with constant phase evolution inside the lobes and jumps by π at nodes. Only the exact shapes of these lobe structures, their height and width, are influenced by the potential U and the length difference of the interferometer arms. The lobe width is inversely proportional to the interaction strength and is minimum $\varepsilon_L \geq 2\pi\hbar v_\mathrm{F}/L$ for strong interactions and the same energy scale controls the dephasing $\varepsilon_0 = \varepsilon_L$. This lower bound of ε_L is set by the fact, that there need to be at least two electrons at the same time in the interferometer. Up to this energy the visibility is supposed to be constant. Additionally it was found for medium and strong interactions, which give energy scales closer to the experiments [71, 77, 87], that the first side lobe has a similar height, or even larger, than the central lobe, which is not observed in the experiment.[1]

All theories of the previous paragraph predict multiple side lobes at any filling factor, since they regard only intra-channel interaction. However, so far multiple side lobes are only reported for $ff > 1.5$, i.e., two co-propagating edge channels. In contrast, a theory based on the bosonization in a chiral Luttinger liquid with two capacitively coupled channels, as introduced in Sec. 2.3.3, can explain multiple side lobes only for two edge channels [31]. As a reminder, the plasmon spectrum collapses into two modes, a (fast) charge mode with velocity u and a (slow) dipole mode with velocity v. The probability amplitudes of each mode carry bias dependent phase factors $\exp(ieV_\mathrm{dc}L/\hbar u)$ and $\exp(ieV_\mathrm{dc}L/\hbar v)$. These phase factors cannot be recognized in a usual conductance measurement, unless one performs a phase sensitive measurement as with a Mach-Zehnder interferometer. Close to $ff = 2$ one can assume, that $u \gg v$ and the phase factor of the charge mode becomes negligible. This situation is already illustrated in Fig. 2.9 and a

[1] Another, here neglected theory also using bosonization in chiral 1D channels gives a power law dependence of the coherence for very large voltages which is not accessible in the experiment and it is not able to reproduce the experimental findings [91].

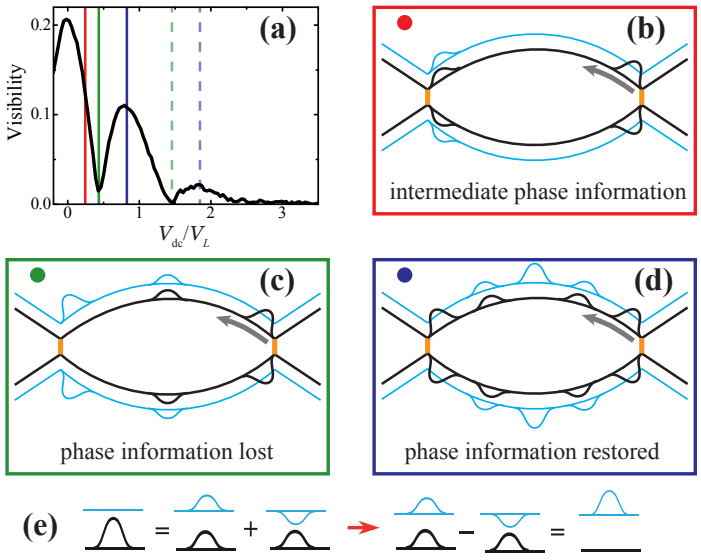

Figure 5.10.: (a) Visibility vs. V_{dc}, x-axis normalized to V_L. (b)-(d) Sketches of plasmons traveling inside the Mach-Zehnder interferometer for three V_{dc}. The plasmon wave packets are snap shots every $\pi/2$ of the plasmon oscillation between edge channels. For low voltages the plasmon excited at QPC 1 starts to oscillate to the inner edge channel and is partially lost at QPC 2 (b, red). For increasing voltage the plasmon oscillates completely to the inner channel and the phase information is lost for the interference and a node is observed in the visibility (c, green). Further increasing the voltage leads to a even faster oscillation of the plasmon and the phase information with the plasmon is recollected at the second QPC (d, blue). (e) Reminder sketch of Fig. 2.9 displaying plasmon oscillation due to charge and dipole mode.

reminding sketch is shown in Fig. 5.10(e) and we see how the superposition of charge and dipole mode oscillates between inner and outer edge channel. The entire product of the original state of the tunneling electron, i.e., electron state and plasmonic excitation, carries the Aharonov-Bohm phase information of the Mach-Zehnder interferometer. However, since the probability amplitude of the plasmon excitation can oscillate to the inner edge channel, which does not take part in the interference at the second QPC, the phase information is lost for the interference and passes by the 2nd QPC. This is illustrated in Fig. 5.10(b)-(d), the sketches show a further simplified Mach-Zehnder interferometer, similar to Fig. 5.1(b), but still with the correct topology of the edge channels, yellow bars represent the tunneling between outer edge channels inside the QPCs. The plasmons are snapshots every $\pi/2$ of the plasmon oscillation. Plot (a) shows a lobe structure with lines color-coded to the sketches of the according plasmon situation. When at small applied dc voltage a plasmon is excited at QPC 1, its dynamical phase

factor starts to oscillate along the interferometer arms and when the wave packet arrives at the second QPC, a part of the Aharonov-Bohm phase information is lost in the inner edge channel as seen in sketch (b). At this point the visibility starts to decrease towards the first node. Increasing the dc voltage leads to a faster oscillation of the plasmon phase factor and will cause the phase information to be completely in the inner edge channel at QPC 2. It is then lost for the interference in the outer channel and the first node is observed, as seen in Fig. 5.1(c). However, with even larger voltages and faster phase factor oscillation the phase information will be recollected in the outer edge channel and the first side lobe shows up [Fig. 5.1(d)]. Depending on the dc voltage the phase information can oscillate several times forth and back between the edge channels leading to multiple side lobes. The faded, dashed colored lines in Fig. 5.1(a) represent the same plasmon situation at QPC 2, but with one more plasmon oscillation along the interferometer arms.
An analogy are neutrino oscillations in high energy physics. A neutrino created in one flavor is a superposition of three mass eigenstates whose phases advance at slightly different rates. Thus after some time and traveled distance the mixture of mass eigenstates has changed and a different mixture of mass eigenstates corresponds to a different superposition of flavor eigenstates. Here an edge excitation is created in one channel by tunneling, but is a superposition of quantum Hall edge eigenstates, i.e., charge and dipole mode, which change phases at different rates. However, neutrino oscillations are just one famous example and the basic physics can be found in any system of coupled harmonic oscillators, e.g., two pendulums connected by a soft spring.
After this very figurative description, I also want to show a simplified version of the theory by Levkivskyi et al. [31] as introduced in Sec. 2.3.3 and similar to Ref. [32]: An electron tunneling to an edge channel through QPC 1 for example, will change the edge state as

$$|N\rangle \rightarrow |N+1\rangle |plasmon\rangle. \tag{5.9}$$

This plasmon in one of the edge channels is not an eigenstate of the edge Hamiltonian and due to the strong Coulomb interaction of the channels it splits into a superposition of charge ($|u\rangle$) and dipole ($|v\rangle$) mode (described by the first sum in Eq. 2.47)

$$|plasmon\rangle = \frac{1}{\sqrt{2}} \left(|u\rangle + |v\rangle \right). \tag{5.10}$$

With applied voltage and the traveled distance the modes acquire phase factors according to their velocities u and v. With a strong interaction, as close to $ff = 2$, we can assume $u \gg v$ and the plasmon state evolves to the second QPC as

$$|plasmon'\rangle = \frac{1}{\sqrt{2}} \left(|u\rangle + e^{ieV_{\mathrm{dc}}L/\hbar v} |v\rangle \right). \tag{5.11}$$

However, the interference experiment is only sensitive to a state in the outer edge channel, so only to the original plasmon state

$$\langle plasmon|plasmon'\rangle = \frac{1}{2}\left(1 + e^{ieV_{\rm dc}L/\hbar v}\right). \tag{5.12}$$

This result from plasmon oscillation contains a real and an imaginary part. The imaginary part would add up to the AB phase in the interference, leading to a linear phase change with bias voltage which is not present in this kind of experiments. The first factor on the right-hand side of Eq. 5.9 represents the electron number in an interferometer arm of length L. Here, by applying voltage to only one edge channel ($\mathcal{T}_0 = 1$), it is charged like a capacitor. In theory this is represented by the number of particles N_α in Eq. 2.40 and it is a uniform charge distribution $q = e^2V_{\rm dc}/4\pi\hbar v$, which can be seen as the sum of single charge excitation $e/2$ along the length L of number $N = eV_{\rm dc}L/2\pi\hbar v$ (see Eq. 2.40), so that $q = N(e/2)/L$. This leads to an additional electrostatic phase shift due to the excess electrons in the edge channel

$$\langle N+1|N+1'\rangle = e^{-i\pi N}. \tag{5.13}$$

Combining these two phase factors one gets

$$\begin{aligned}\langle N+1|N+1'\rangle\langle plasmon|plasmon'\rangle &= \left(e^{i\pi N} + e^{-i\pi N}\right)/2 \\ = \cos(\pi N) &= \cos(eV_{\rm dc}L/2\hbar v)\end{aligned} \tag{5.14}$$

This does describe the oscillating cosine part of the phenomenological formula Eq. 5.6, with $\varepsilon_L = 2\pi\hbar v/L$, and since it is a real number it does not lead to an additional (linear) AB phase, but to the π jumps occurring at the nodes. The lobe structure here is a combined effect of plasmon oscillations and the zero mode charging by applying voltage to only one edge channel and leaving the other grounded.
In general, the energy related to the lobes according to this theory [31] is given by

$$\varepsilon = \frac{2\hbar uv}{(u-v)(L_U + L_D)}, \tag{5.15}$$

which becomes[2] $\varepsilon = \hbar v/L$ in the limit that $L_U = L_D = L$ and $u \gg v$, assuming a long-range interaction as decribed in Eq. 2.45. Taking the explanation for $ff = 1$ with one side lobe into account it is natural to think that the same energy scale is responsible for the exponential decay of the visibility with bias voltage what is usually seen in experiment (see Sec. 5.4). This theoretically predicted energy is proportional to the lobe width as $\varepsilon_L = 2\pi\varepsilon \approx 2\pi\hbar v/L$. This enables us to estimate the velocity of the

[2]This implies that the periodicity of the lobe structure behaves like the characteristic temperature T_0 and the characteristic energy eV_0 for single side lobe behavior with $1/L$.

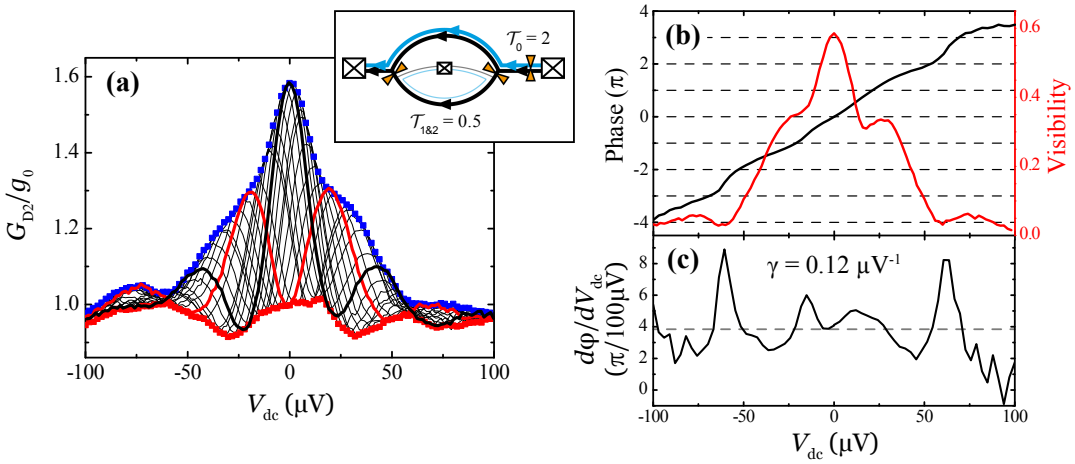

Figure 5.11.: (a) Raw data: conductance traces vs. V_{dc} for different V_{mg}. Inset shows a sketch of the QPC setting and resulting edge channels. (b) Visibility (red) and phase evolution (black) as evaluated from the envelope in (a). (c) Numerical derivative of the phase evolution for detailed study of the phase fluctuations.

dipole mode v for a given lobe structure from the lobe width when close to $ff = 2$. For the lobe structure in Fig. 5.8 we obtain $v = 57\,\mathrm{km/s}$ at $ff = 1.75$, which is in the expected range[3] similar to the Fermi velocity v_{F}.
Also the here introduced energy scales ε_L and ε can be found in the overview of App. B.

Applying bias to two channels

Previously the transmission of QPC 0 was set to transmit only the outer edge channel and cut the inner from bias so that the inner edge channel in the upper arm of the interferometer is grounded, in the same way as is the inner channel in the lower arm (see Fig. 5.8(c) inset). This leads to a lobe structure with several side lobes and nodes. As seen in Eq. 5.13 the charging by the zero modes is a significant contribution to the bias behavior. Thus, it is natural to expect, that the lobe structure will change drastically when QPC 0 is opened to transmit the inner edge channel, too, and both edge channels in the upper interferometer arm are biased, i.e., charged with N zero modes.
As one can see in the sketches in Fig. 5.1(b) and the inset in Fig. 5.11, the inner edge channel is biased only along one interferometer arm, the upper arm. QPCs 1 and 2 are still adjusted to partial transmission of the outer channel, thus the inner is blocked and the inner edge channel in the lower arm remains grounded by the inner ohmic contact.

[3] A galaxy in a distance of 0.77 Mpc moves away from ours with this velocity.

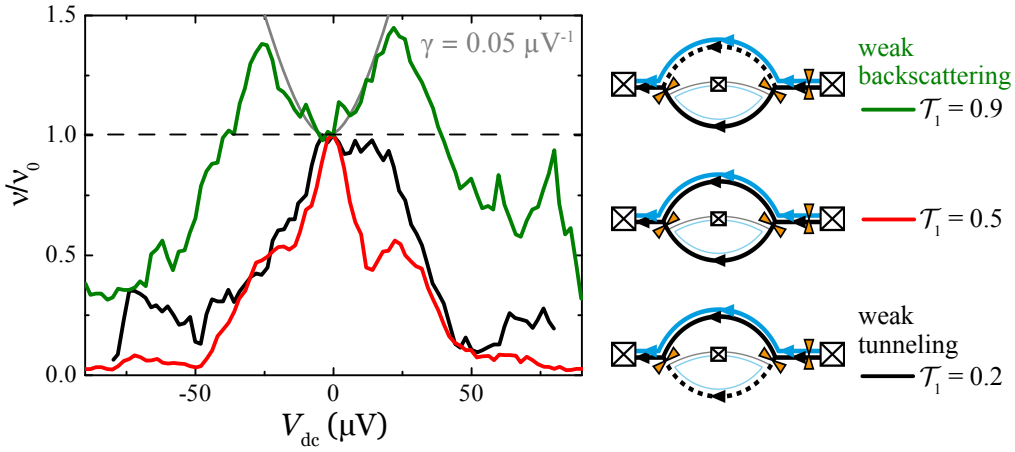

Figure 5.12.: At $ff = 2$ and with both edge channels biased the behavior of the lobe structure is no more comparable for different $\mathcal{T}_1$, i.e., preferred transport in upper or lower interferometer arm. This is shown for three transmissions $\mathcal{T}_1 = 0.9$ (weak backscattering), 0.5 and 0.2 (weak tunneling), accompanied by sketches of the according edge channel configuration. Prominent is the increasing visibility with V_{dc} in the weak backscattering regime. The low bias curvature is fitted with Eq. 5.16 and yields a coupling $\gamma = 0.05\,\mu\mathrm{V}^{-1}$.

Data recorded on a sample of type A at a filling factor of 1.7, the same *ff* as in Fig. 5.9, is shown in Fig. 5.11(a) and the extracted visibility and phase evolution in (b). In this QPC setting a wide central lobe ($V_1 \approx 60\,\mu$V) appears and a small lobe at large bias (lobe width $V_L \approx 40\,\mu$V). The big central lobe shows bumps at voltages similar to the first node in the case for one biased channel, which resemble residues of the previous nodes. The phase, previously constant inside lobes and displaying jumps by π at nodes, shows an almost linear dependence on bias voltage V_{dc}. Very pronounced slips, which appear to by of the height of π at the nodes, and additional small fluctuations inside the central lobe are present [black line in Fig. 5.11(b)]. A powerful tool to further investigate the phase evolution, shown in Fig. 5.11(c), is to plot the numerical derivative $d\varphi/dV_{\mathrm{dc}}$. In the derivative the average value gives the linear background and the slips by π at the nodes are pronounced peaks (at $\approx \pm 60\,\mu$V). Furthermore, one can see that the small wiggles in the phase at $\approx \pm 20\,\mu$V correlate with the superimposed oscillations in the visibility. Thus we see that the phase evolution carries most of the information of the bare visibility and provides the possibility to verify more precisely and cross-check certain parameters as for example V_1.

In Fig. 5.9 it is clear that the lobe structure does not change its shape, when changing transmission of QPC 1 for $\mathcal{T}_0 = 1$. When QPC 0 is open completely and the inner edge channel also is biased, then there is a striking discrepancy between large and small $\mathcal{T}_1$. The visibility, normalized to the zero bias value ν_0, is depicted in Fig. 5.12 for three dif-

ferent transmissions of QPC 1. The legend also illustrates the according edge channel situation in the Mach-Zehnder interferometer. The red curve for $\mathcal{T}_1 = 0.5$ is the same as in Fig. 5.11(b). For small transmission $\mathcal{T}_1$ (weak tunneling) the lobe structure looks similar as for half transmission, only the bumps in the central lobe have vanished and it decreases smoothly to the nodes. The side lobes seem to keep their size.
In contrast, the lobe structure changes significantly when setting to larger transmissions $\mathcal{T}_1 \approx 1$, the so-called weak backscattering regime, when electrons are mostly transmitted to the lower interferometer arm. Then the visibility is increasing for small bias voltages until it changes to a decay for large voltages. This behavior of the lobe structure at $\mathit{ff} \approx 2$ and both edge channels biased was studied in detail by Bieri et al. [78]. There already a model was introduced to describe the basic features. In this model the inner edge channel along the upper arm was described as an additional modulation gate at which the bias voltage $V_{\rm dc}$ is applied and thus electrostatically influences the outer channel which is part of the interference. This view is obvious because of the geometry and the linear phase evolution. Basically this assumption leads to an additional part in the interference term of the modulation gate $\sin(\varphi_{\rm dc} + \varphi_{\rm mg}) = \sin(\gamma V_{\rm dc} + \varphi_{\rm mg})$, where γ is the coupling of the outer to the inner edge channel. The coupling can be deduced from the linear part of the phase evolution [gray dashed line in Fig. 5.11(c)] and in the experiment presented here at filling factor 1.7 couplings of $\gamma = 0.11 - 0.15\,\mu\mathrm{V}^{-1}$ are found. With this gating effect also the increase of the visibility with bias voltage can be explained. In Ref. [78] a formula is developed to fit the curvature at zero bias for the visibility increase

$$\nu(V_{\rm dc})/\nu_0 = 2\hat{\mathcal{T}}_{mzi}\sqrt{1 + (\gamma V_{\rm dc})^2}, \tag{5.16}$$

where $\hat{\mathcal{T}}_{mzi}$ is the average transmission of the outer edge channel in the Mach-Zehnder interferometer. This is used to fit the curve for $\mathcal{T}_1 = 0.9$ and shows a coupling $\gamma = 0.05$, which is roughly half of the value extracted from the bias dependent phase shift. This is a similar discrepancy as in Ref. [78].
Another way to check whether the influence of the inner edge channel can be understood as an additional modulation gate controlled by $V_{\rm dc}$ is by using the phenomenological model of Eq. 2.74 and adding a bias dependent phase to the coherent current vs. $V_{\rm dc}$

$$\begin{aligned} I_{coh}(V_{\rm dc}) &= I_0 e^{-V_{\rm dc}^2/2V_0^2}\sin(\gamma V_{\rm dc} + \varphi_{\rm mg}) \\ &= G_0 V_{\rm dc} e^{-V_{\rm dc}^2/2V_0^2}\sin(\gamma V_{\rm dc} + \varphi_{\rm mg}). \end{aligned} \tag{5.17}$$

Then the coherent conductance becomes

$$\begin{aligned} G_{coh}(V_{\rm dc}) &= G_0 e^{-V_{\rm dc}^2/2V_0^2}\left[\left(1 - V^2/V_0^2\right)\sin(\gamma V_{\rm dc} + \varphi_{\rm mg})\right. \\ &+ \left.\gamma V_{\rm dc}\cos(\gamma V_{\rm dc} + \varphi_{\rm mg})\right]. \end{aligned} \tag{5.18}$$

An example of this for various $\varphi_{\rm mg}$ can be seen in Fig. 5.13(a) for $\gamma = 0.04$ and the according visibility in (b) together with the visibility for $\gamma = 0.1$, where a clear

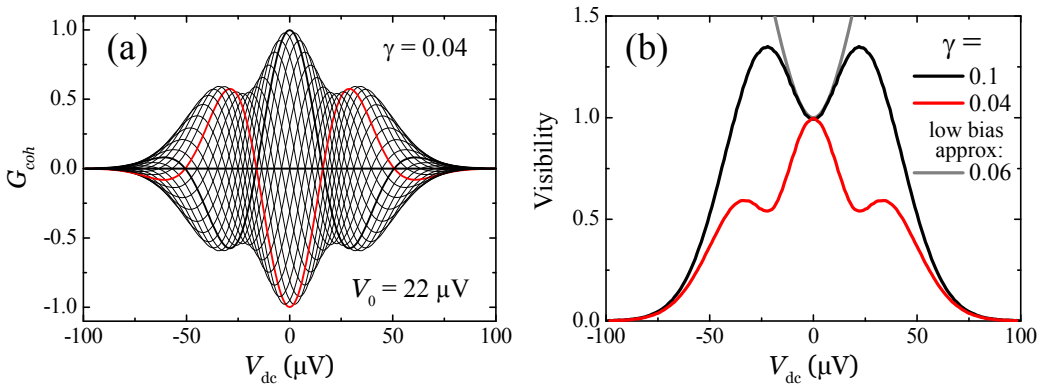

Figure 5.13.: (a) Calculated traces of $G_{coh}(V_{\rm dc})$ for several $V_{\rm mg}$ of Eq. 5.18 with a characteristic energy of $eV_0 = 22\,\mu$eV and a coupling of $\gamma = 0.04$. (b) Evaluated visibility from calculated curves as in (a) for couplings $\gamma = 0.1$ and 0.04. The low bias approximation of Eq. 5.16 for the calculated visibility with $\gamma = 0.1$ giving an approximated coupling of 0.06 instead.

increase of visibility with voltage can be seen. To illustrate the distinctiveness of this situation we look at the maximum coherent conductance $[G_{coh}(0)]_{max} = G_0$ and $[G_{coh}(V_0)]_{max} = G_0\gamma V_0/\sqrt{e}$ and see easily that one can have an increase of visibility if $\gamma V_0 > \sqrt{e} \approx 1.65$. The factor $\gamma V_{\rm dc}$ is the prefactor of the cosine term and represents the fact that the maximum coherent current appears at $V_{\rm dc} = V_0$, if the coupling is strong enough, i.e., fast oscillations of I_{coh} with $V_{\rm dc}$, then one can choose a phase $\varphi_{\rm mg}$ so that the conductance $G_{coh} > G_0$ at this voltage.

Fig. 5.13 shows that curves of this model with appropriate choice of γ and V_0, γ from Fig. 5.11 and $V_0 = V_1$ from Fig. 5.9, resemble very nicely the central lobe of the measurements in Fig 5.12. That is, the increase of visibility with $V_{\rm dc}$ with maxima at $V_{\rm dc} \approx V_1$ and a height of $\approx 1.3 \cdot \nu_0$. And that the central lobe can show the mentioned bumps as seen in Fig. 5.11.

Eq. 5.16 from Ref. [78] is a low bias approximation of the presented model, which regards the inner edge channel as an additional modulation gate. Nevertheless, when applying this approximation to a model curve with $\gamma = 0.1$, as seen in Fig. 5.13(b), it leads to a $\gamma = 0.06$, which is smaller by roughly a factor of two. This is almost the same discrepancy between couplings γ gained from the phase evolution and Eq. 5.16. Thus, this approximation can only describe qualitatively the increase of visibility with bias voltage, but not quantitatively.

There are also limitations to the described phenomenological model. Comparing calculated lobe structures for different couplings in Fig. 5.13(b) with measured ones of different transmissions $\mathcal{T}_1$ in Fig. 5.12, we see that the model curve with $\gamma = 0.1$ looks like the experimental curve with $\mathcal{T}_1 = 0.9$, and the model curve with $\gamma = 0.04$ like

$u \gg v$	$N_{1,D}$	$N_{1,U}$	$N_{2,D}$	$N_{2,U}$
weak tunneling	≈ 0	$eV_{\mathrm{dc}}L/2\pi\hbar u$	0	$eV_{\mathrm{dc}}L/2\pi\hbar u$
weak backscattering	$eV_{\mathrm{dc}}L/4\pi\hbar v$	$\approx -eV_{\mathrm{dc}}L/4\pi\hbar v$	0	$eV_{\mathrm{dc}}L/2\pi\hbar u$

Table 5.1.: Number of charges in the 4 different channels (upper U and lower D arm, outer and inner channel) in the limit $u \gg v$. The different situation of the zero mode $N_{\alpha,j}$ between weak tunneling ($\mathcal{T}_1 \approx 0$) and weak backscattering ($\mathcal{T}_1 \approx 1$) leads to the discrepancies between these regimes seen in the visibility bias dependence.

the experiment with $\mathcal{T}_1 = 0.5$. This might suggest that there is a change of coupling between different $\mathcal{T}_1$, but the coupling evaluated from the phase evolution stays roughly constant. Also the model cannot describe the side lobes, it can only give a more phenomenological insight of how the capacitive coupling alone can alter the lobe structure, especially the central lobe.

As in the case when only one edge channel is biased, i.e., $\mathcal{T}_0 = 1$, the theory of plasmonic excitations [31] can also explain more phenomena for $\mathcal{T}_0 = 2$. Next to the plasmon excitations u and v, the zero mode N_α is of importance in this theory. This zero mode also accounts for the charging effect between inner and outer edge channel, i.e. the capacitive coupling. Now not only the outer channel carries excess charges N_1, but also the inner, N_2, due to the applied voltage V_{dc} to both channels. As one can see in the sketches of Fig. 5.12 this is completely different for the regimes of weak backscattering and weak tunneling. Numbers of charges $N_{\alpha,j}$, where $j = U, D$ denotes upper (U) and lower (D, down) interferometer arm are displayed in Tab. 5.1 in the limit $u \gg v$ as given by equations 2.43 and 2.44. In the weak tunneling regime there are practically no zero charges $N_{\alpha,D}$ in the lower arm, because both have no bias, only in the upper arm, where both channels carry the same number of charges. According to Ref. [31] the visibility is governed by the Bessel function J_0 in this case. This defines a new energy scale $\varepsilon' = \hbar v/\Delta L$, where ΔL is the length difference between upper and lower arm. It is this energy scale that describes the increased width of the central lobe, compared to the side lobes of smaller width. Inside lobes the phase should grow linear. This describes the shape of the measured lobe structure. Estimating from SEM pictures the Mach-Zehnder interferometer of this measurement is almost completely symmetric corresponding to a very small ΔL. Thus we would expect an even wider central lobe. The theory explains qualitatively the increased lobe width and the asymmetry between weak tunneling and weak backscattering regime, but not the new energy scale $eV_1 \propto \varepsilon'$. We attribute this to the limit of both weak tunneling and $u \gg v$, so this ε' is only valid for $\mathcal{T}_1 \to 0$ and $ff = 2$. Another reason for the disagreement might be that V_1 is strongly depending on the dephasing described by ε_0, which is not described by this theory.

The second extreme case is the weak backscattering regime where $\mathcal{T}_1 \to 1$. In this

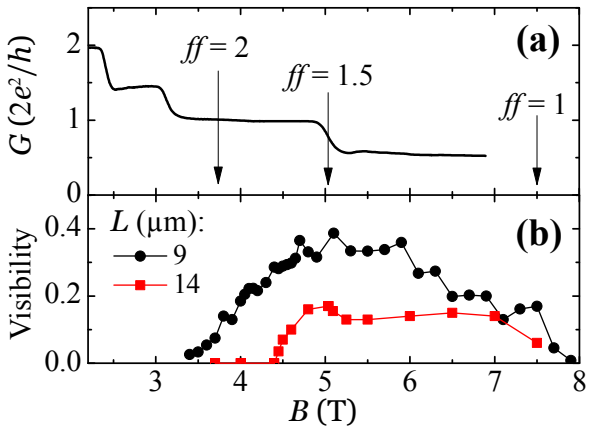

Figure 5.14.: (a) Two-point conductance vs. magnetic field with conductance steps due to the quantum Hall effect. (b) Maximum visibility at base temperature in the same range of magnetic field for two Mach-Zehnder interferometers of different size. (Reproduced from Ref. [71])

regime in the upper arm the inner edge channel is biased, but not the outer, and in the lower arm the outer and not the inner. However, due to the Coulomb interaction a charge density develops also in the outer edge channel in the upper arm (see Tab. 5.1, $N_{1,U}$ weak backscattering). Then an increase of visibility with bias around $V_{\mathrm{dc}} = 0$ is expected.
The theory also predicts the bias dependent phase shift, which is simply the capacitive coupling $\gamma = \partial\varphi/\partial V_{\mathrm{dc}} = (e/\hbar)(L/v)$. Then we can cross-check the velocitiy v, that one can calculate from the ε_L from Fig. 5.9 ($\mathcal{T}_0 = 1$) with that from the γ deduced from Fig. 5.11 ($\mathcal{T}_0 = 2$), both at the same filling factor $ff \approx 1.7$. One gets a velocity $v \approx 75\,\mathrm{km/s}$ from the lobe periodicity ε_L and $v \approx 82\,\mathrm{km/s}$ from the linear phase shift γ, which is a difference of below 10 %, and supports the validity of the described microscopic theory of Levkivskyi et al. [31].
Thus, with the theory of plasmonic excitations we can explain the discrepancy between weak tunneling and weak backscattering, the linear background phase and the possible increase of visibility for small, increasing bias voltage.

5.4. Coherence controlled by filling factor

In the sections above, the measurement of the visibility and its dependence on temperature as well as the various behaviors for different QPC settings in the bias characteristic is introduced. With this arise important energy scales, such as the characteristic temper-

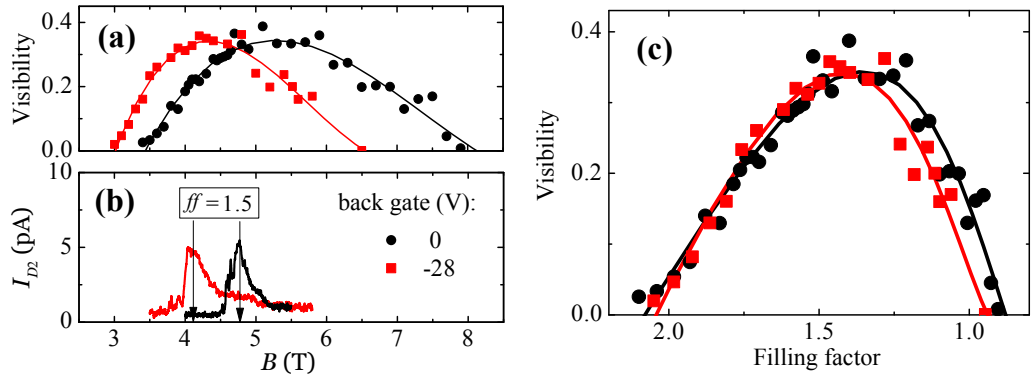

Figure 5.15.: (a) Visibility vs. B for $V_{backgate} = 0$ and -28 V. (b) Back scattering current of **D2** when only QPC 2 is closed. The maximum defines $ff = 1.5$. (c) Visibility as in (a), but vs. filling factor. Curves for different $V_{backgate}$ coincide. (Reproduced from Ref. [71])

ature $k_B T_0$ (which is connected to the coherence length l_φ via Eq. 5.5) or lobe sizes ε_0 and ε_L.[4] The magnetic field, and with it the filling factor, was mentioned as an external parameter, that only defines the number of edge channels. In fact, the magnetic field and the exact filling factor have a pronounced effect on all the measurements I showed before and actually interconnects them.

In the following the Mach-Zehnder interferometer is of type A and the QPC setting is always such that QPCs 1 and 2 are set to half transmission ($\mathcal{T}_1 = \mathcal{T}_2 = 0.5$) and QPC 0 to transmit only one, namely the outer edge channel ($\mathcal{T}_0 = 1$).

The two-point conductance of the sample vs. magnetic field showing the quantized steps of the integer quantum Hall effect is depicted in Fig. 5.14(a). This is compared to the zero bias visibility at base temperature for interferometers of arm lengths 9 and 14 μm for the same range of magnetic field in (b). Both samples show a non-monotonic behavior of the maximum zero bias visibility. A measurable visibility shows up at $B \approx 3.5 - 4$ T, increasing to a maximum at 5 T, then decreasing and vanishing at 8 T. Comparing the visibility with the two-point conductance suggests that any coherence is present only between filling factors 1 and 2 with the maximum at $ff \approx 1.5$. To verify this assumption a backgate was used to change filling factors for the same magnetic fields. Charged negative to the fixed value $V_{backgate} = -28$ V in the sample with $L = 9\,\mu$m to reduce the electron density it has the effect of larger filling factors for the same magnetic field. Then the zero bias visibility vs. B was measured again in this setting and the results for both $V_{backgate}$ are depicted in Fig. 5.15(a). The change of filling factor was checked by sweeping the magnetic field, leaving QPCs 0 and 1 open and having

[4] These are the important energy scales. As another reminder, App. B gives an overview over them, together with their interconnection.

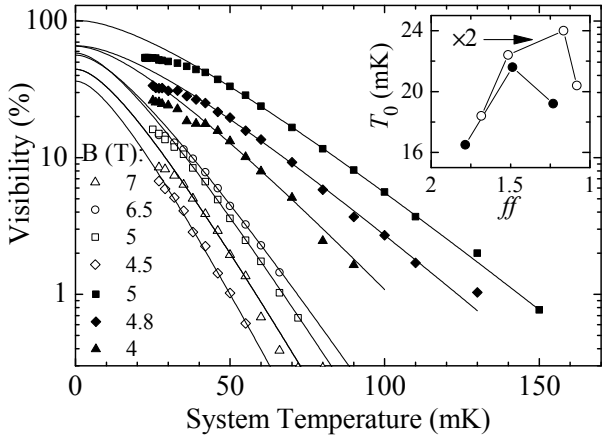

Figure 5.16.: Visibility is displayed vs. temperature for Mach-Zehnder interferometers with $L = 14\,\mu$m (open symbols) and $L = 9\,\mu$m (full symbols) for different magnetic fields. The inset shows the characteristic temperature T_0 (from fits to Eq. 5.4) for these two samples (times two for the larger sample with smaller T_0) vs. filling factor. (Reproduced from Ref. [71])

QPC 2 closed while measuring the current at **D2**. For fully developed edge channels all the current is deflected by QPC 2 into **D1**, the inner ohmic contact, and no current flows into **D2**. When the magnetic field is swept and a Landau level passes the Fermi energy, back scattering occurs in the bulk of the sample and a part of the current can flow into **D2** with a maximum at $ff = 1.5$. Fig. 5.15(b) shows how the filling factor is shifted when a negative backgate voltage is applied. With this it is verified, that the shifted visibility in Fig. 5.15(a) originates from a shifted filling factor. With the exact knowledge of $ff = 1.5$ the behavior of $\nu(B)$ can be converted to $\nu(ff)$ [Fig. 5.15(c)]. After this conversion both curves for the visibility coincide and we clearly see that the maximum visibility is governed by the filling factor.

Next we look at the temperature dependence of the visibility for different magnetic fields in Fig. 5.16 and see that the exponential decay, i.e. the slope in the log scale plot, is changing with magnetic field, not only with arm length L. This means that also T_0, extracted from fits to Eq. 5.4, changes with magnetic field, i.e., filling factor, as seen in the inset of Fig. 5.16. Also here we see a similar nonmonotonic behavior as for the visibility, which was investigated more detailed in another work [77].

Other important energy scales show up in the lobe structure of the bias dependence. The lobe structures for various magnetic fields are illustrated in Fig. 5.17. Next to the variation of the zero bias visibility a change of the lobe width can be recognized. As mentioned above, no multiple side lobes appear at $ff < 1.5$, only for larger filling factors, and even then not always. To study the lobe behavior consistently for all magnetic

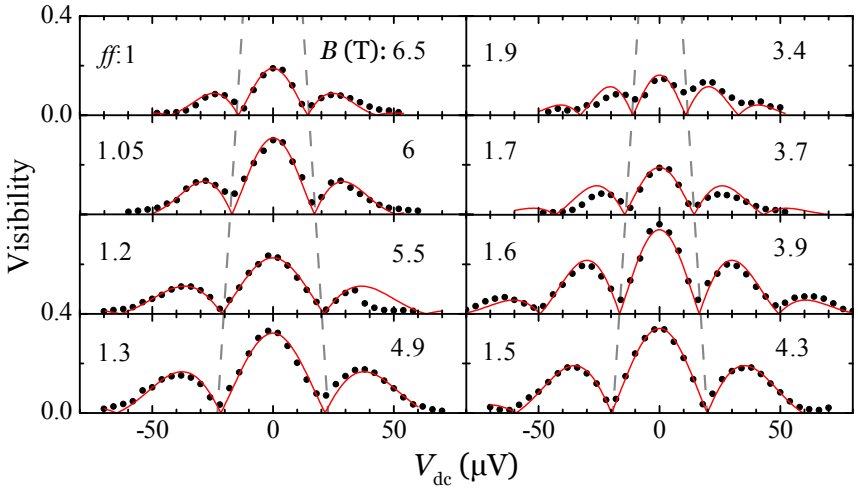

Figure 5.17.: Lobe structure for different magnetic fields of a sample of type A ($L = 9\,\mu$m) at base temperature. The variation of the energy scales (dashed lines) and maximum visibility can be seen. (Reproduced from Ref. [71])

fields and filling factors, Eq. 5.6 was used to fit all curves, although curves with only single side lobes may be more accurately fitted with Eq. 2.74. By this we gain from each curve the energies ε_0 and ε_L.

These characteristic energies of the lobe structure show also a behavior of a maximum around $ff \approx 1.5$ and decreasing towards filling factors 1 and 2. Now we can look at all the characteristics for changing filling factor in Fig. 5.18. All the characteristic energies follow the evolution of the zero bias visibility. The energies of the lobe structure, ε_0 and ε_L, have almost the same value, especially at $ff > 1.5$ when Eq. 5.6 is more appropriate. Comparison of these energies with the characteristic temperature $k_\mathrm{B}T_0$ shows that with a factor of $\sim 2\pi^2$ we reach similar values.

All this suggests that there is an underlying energy scale, that is controlled by the filling factor, which governs the characteristic energies and to some extent the visibility. For the maximum zero bias visibility not only the interferometer size L might be important, also the width of the edge channels. Theory of self-consistent edge reconstruction [27] suggests that when increasing the filling factor, the edge channels are pushed closely together and towards the edge and may result in a complete collapse of the outermost edge channel if it becomes too narrow. On the other hand, when the filling factor decreases, edge channels are pushed away from the edge and their width increases. This might lead to a not well defined area between the interferometer arms, because the area defined by inner and outer boundaries of the edge channels differ too much and thus a smearing of coherence due to too much phase averaging. A further influence in the zero bias visibility is the characteristic temperature T_0, since ν_0 is measured at the base temperature of

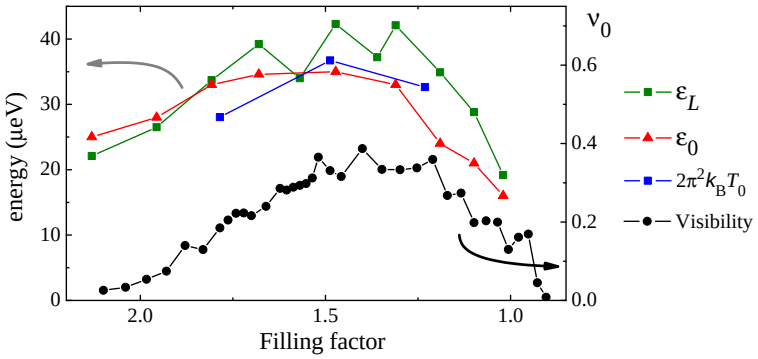

Figure 5.18.: The energy scales ε_L, ε_0 and $2\pi k_\mathrm{B}T_0$ of a sample of type A ($L = 9\,\mu$m) are display as a function of the filling factor (colored symbols, left axis). They follow the evolution of the zero bias visibility (black symbols, right axis) with minima close to integer filling factors 1 and 2 and a maximum at $ff = 1.5$. (Reproduced from Ref. [71])

the cryostat ($\sim 30\,$mK) and not $T = 0$, thus the zero bias visibility vs. magnetic field varies together with T_0.
The important energy in the theory of plasmonic excitations $\varepsilon \approx \hbar v/L$ is depending on the velocity of the plasmons and the size of the interferometer L (see Eq. 5.15). This energy not only controls the lobe width, i.e., periodicity $\varepsilon_L = 2\pi\varepsilon$, but also the temperature dependence and thus $k_\mathrm{B}T_0 = \varepsilon/\pi$ [31]. The plasmon mode velocities u and v are results of size and Coulomb interaction of the present edge channels, i.e., width and distance between them. Qualitatively, the change of u and v as it is expected when going from $ff = 2$ to 1 leads precisely to a variation of the characteristic energy, such that it starts to increase when decreasing filling factor from 2 ($u \gg v$) reaching a maximum when $u \approx v$ and decrease towards $ff = 1$ when there is only the charged mode u [31].
Theories that take intra-channel Coulomb interaction into account [88–90] lead to characteristic energies which depend, next to the interaction strength U, on the number of non-equilibrium electrons in a interferometer arm at a time, which is defined by the electron drift velocity v_F. These theories can explain a lobe structure with multiple side lobes in the bias depending visibility and an decaying envelope. Additionally, they can be applied for any QPC 1 and 2 transmission, unlike as the theory provided by Levkivskyi et al. [31], where QPCs are regarded only as perturbations in the weak tunneling and weak backscattering regime. However, the disadvantages of the mere intra-channel interaction is that they would imply multiple side lobes also for filling factors close to one, which is not seen in our experiments and was not reported so far in the literature. An explanation for this behavior within the theory of intra-channel interaction is, that the screening properties change from $ff > 1.5$ to $ff < 1.5$ due to the disappearence

of the inner channel. In consequence, the variation of the screening changes the intra-channel Coulomb interaction, by accident, such that either multiple or single side lobes appear. That reasoning, that "by accident" the screening changes in the according way is a bit unsatisfying. In addition, what one sees in the experiment is a non-monotonic behavior of the energy scales with a maxumum at $ff \approx 1.5$ and thus the energies are approximately the same, e.g., for $ff \approx 1.75$ and $ff \approx 1.25$. Then if $\varepsilon_L = \varepsilon_0$, one would have to observe almost the same lobe structure with multiple side lobes for both filling factors, which is not the case in the experiment, where we see a change from multiple side lobes to single. That suggests, that for $ff < 1.5$ we cannot distinguish ε_L from ε_0, since there appears a kind of dephasing which can be phenomenologically described as in Sec. 2.6, which leads to a single side lobe.
In contrast to these theories, where interaction is only regarded inside one edge channel, the theory presented by Levkivskyi and Sukhorukov [31], which highlights the interaction between co-propagating channels, can better explain all the present features of coherence. The dependence on temperature and interferometer size L with a coherence length $l_\varphi \propto T^{-1}$, the lobe structure with multiple side lobes, whose energy $\varepsilon \propto L^{-1}$ is proportional to the characteristic thermal energy $k_\mathrm{B}T_0$, with the experimentally observed proportionallity factor $\approx 2\pi^2$, all these properties are correctly described. Also, it represents the changing behaviors for different QPC settings. That is, at $\mathcal{T}_0 = 1$ the "usual" lobe structure with multiple side lobes, at $\mathcal{T}_0 = 2$ and $\mathcal{T}_1 \to 1$ the visibility can increase with V_dc, and at $\mathcal{T}_0 = 2$ and $\mathcal{T}_1 \to 0$ the lobe structure with the widened central lobe. Furthermore, the non-monotonic behavior of the visibility and energy scales with magnetic field can be explained by the changing widths of compressible and incompressible strips and the resulting modified edge velocities u and v.
Objections to this theory according to Ref. [90] are, e.g., that QPCs 1 and 2 are treated only perturbatively, which is a limitation of the applied technique, but should not impede its overall validity within this limitation; and second that this theory does not describe the decaying envelope of the lobe pattern. To explain this general dephasing the assumption of a second, separate physical process, such as dispersion of the edge modes, is required. In the experiments the energy scales that define the lobe periodicity and envelope for $ff > 1.5$ are approximately the same ($\varepsilon_L \approx \varepsilon_0$). And a smooth evolution of the energy scales from the single side lobe behavior for $ff < 1.5$ to a multiple side lobe behavior for $ff > 1.5$ is seen in the experiment. The criticism is, that this would be a "surprising coincidence" if two separate mechanisms gave the same energy scale. However, even different theories with different mechanisms involved (intra-channel interaction versus inter-channel interaction) lead to the same energy scale of $\approx \hbar v_\mathrm{F}/L$. One always deals with energies, that are $\approx \hbar v_\mathrm{F}/L$, slightly modified by the interaction. Regarding all this I conclude, that the theory based on inter-channel interaction by Levkivskyi et al. is the most favorable theory so far to explain the majority of the experimental results.

6. Noise-induced phase transition

"God does not play dice with the universe."

Albert Einstein

In the previous chapter I presented measurements to describe important characteristics of a Mach-Zehnder interferometer as a function of different parameters, such as temperature, bias voltage and magnetic field. Another interesting aspect is to use the Mach-Zehnder interferometer as a detector. Here it is used as a detector of the state of a QPC, i.e., the noise it produces. To be precise, in this case we are looking at QPC 0 and its effect for $\mathcal{T}_0 < 1$, as opposed to $\mathcal{T}_0 = 1$ or 2 studied before. It is still under debate, whether the non-Gaussian nature of the non-equilibrium noise produced by a QPC, described by Levitov et al. [34], can be detected with a Mach-Zehnder interferometer [92], or if a mere Gaussian description is sufficient [93]. For this it is crucial to have a measurement method, which is sensitive to higher order cumulants, otherwise this can not be decided. The Mach-Zehnder interferometer is a detector which is not only sensitive to mere charge and current fluctuations, but also highly perceptive to the phase of the involved particles. This feature makes the electronic Mach-Zehnder interferometer a promising tool to investigate the topic of non-Gaussian noise produced by a QPC.
For the following experiment QPC 0 is set to $\mathcal{T}_0 = 0-1$ and the Mach-Zehnder interferometer acts as a phase sensitive detector of the non-equilibrium noise originating from QPC 0.

6.1. Description of the experiment

6.1.1. Characterization of the samples

Two samples are investigated, one of type A and one of type B, in the following referred to only as sample A and B. As mentioned before, sample A was fabricated and measured by Leonid V. Litvin. Sample B was fabricated and measured in the course of my work, together with the analysis and data evaluation for both samples.
To illustrate the situation of the edge channels in this experiment, Fig. 6.1 shows an electron scanning micrograph with sketched edge channels in panel (a) and the according sketch of only the edge channels in panel (b). Sample A has an estimated interferometer

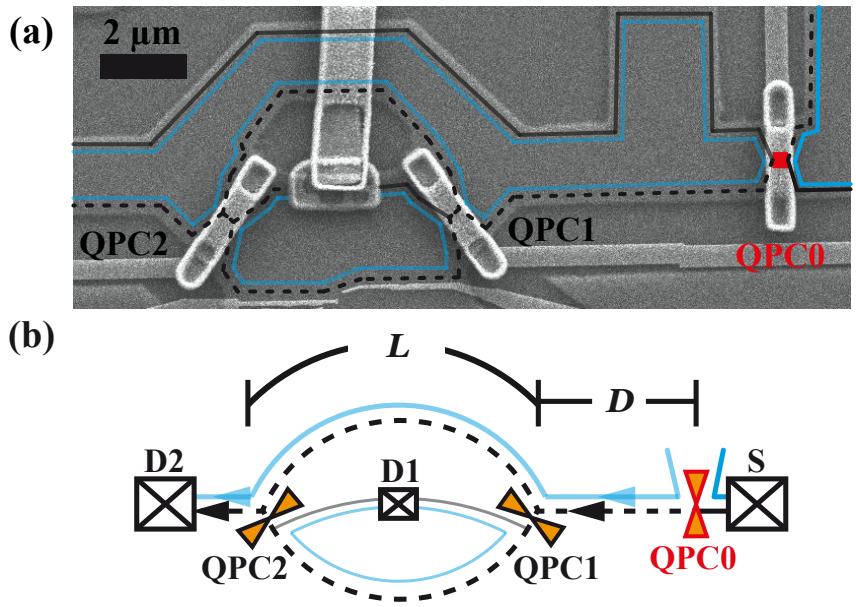

Figure 6.1.: (a) Shows a scanning electron micrograph of a Mach-Zehnder interferometer together with edge channels at $ff = 2$. The outer channel is black, the inner is light blue. QPC (marked orange, and QPC 0 additionally highlighted red) settings here are: $\mathcal{T}_0 < 1$, $\mathcal{T}_1 = \mathcal{T}_2 = 0.5$. In (b) a simplified sketch illustrates the same situation in the interferometer displaying only ohmic contacts, QPCs and edge channels. Channels of the upper edge and the mesa are neglected. The length of an interferometer arm is L and the distance between QPC 0 and QPC 1 is D.

size of $L = 6.5\,\mu$m and a distance between QPC 0 and QPC 1 of $D = 5\,\mu$m, in sample B the values are $L = 8.7\,\mu$m and $D = 8\,\mu$m. We adjust the magnetic field to a filling factor between 2 and 1.5 to have two well defined edge channels and a large zero bias visibility at the same time. To be precise, we have filling factor 1.7 for sample A and 1.8 for sample B. Both samples are kept at the cryostat's base temperature of $T \approx 30\,$mK. QPCs 1 and 2 are set to half transmission and their current voltage characteristic shows no nonlinearities. In this setting we investigate dephasing properties and the quality of noise (whether it is Gaussian or non Gaussian) introduced by QPC 0 (marked red in Fig. 6.1) for transmissions $\mathcal{T}_0 = 0 - 1$.

The *point of reference* for any investigated properties is the situation at $\mathcal{T}_0 = 1$ and we get characteristic energies of the Mach-Zehnder interferometer from its bias dependence as introduced in chapter 5. The maximum zero bias visibility in this state is $\nu_{0,A} = 0.65$ in sample A and $\nu_{0,B} = 0.335$ in sample B. This difference is mostly due to the size difference with which the visibility decreases exponentially at finite temperatures as shown in Eq. 5.5. The small difference in filling factor has a minor effect. Another important

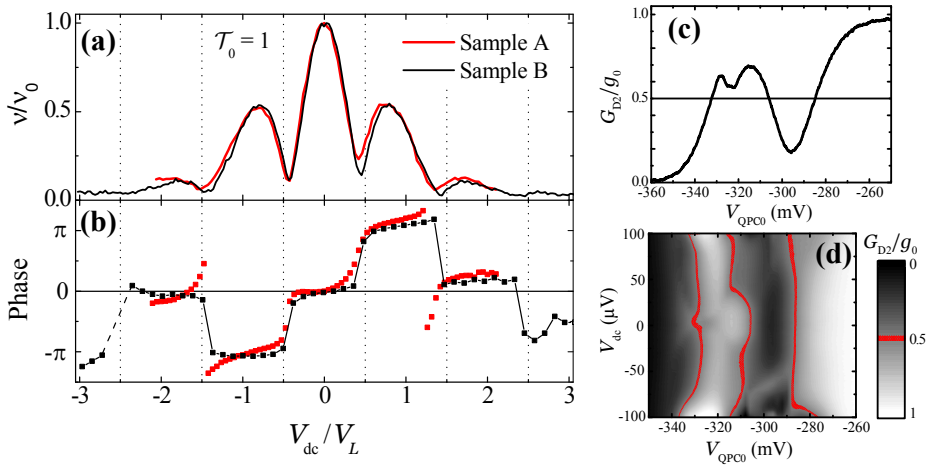

Figure 6.2.: Lobe structure in visibility (a) and phase evolution (b) for QPCs 1 and 2 set to $\mathcal{T}_1 = \mathcal{T}_2 = 0.5$ and $\mathcal{T}_0 = 1$ for samples A and B with the visibility scaled to ν_0 and the dc bias voltage to V_L. The scaling cancels the effect of the different interferometer sizes and the two curves agree very well. Characteristic of QPC 0 in sample B: (c) Zero bias gate trace of the conductance with peaks and dips. (d) Differential conductance as a function of V_{dc} and V_{QPC0}. Conductance around $0.5g_0$ is shaded red. To cover all QPC 0 transmissions with as little nonlinearities in the IV characteristic as possible, gate voltages $V_{\mathrm{QPC0}} < -335\,\mathrm{mV}$ and $V_{\mathrm{QPC0}} > -285\,\mathrm{mV}$ are used.

parameter is the width of a side lobes V_L, which is 47.5 μV for sample A and 32.4 μV for sample B. With the approximation of Eq. 5.15, $eV_L/2\pi = \varepsilon = \hbar v/L$, we can check if this difference is solely due to the size difference L. Thereby we attain velocities of the plasmon mode of $v = 75$ km/s and 68 km/s for sample A and B respectively. This is in a range which is expected [77] and the slight difference might be explained by the different filling factors [31], but is of no importance and is neglected. Fig. 6.2 shows the lobe structure (visibility and phase evolution) for both samples at $\mathcal{T}_0 = 1$ with the voltage scaled to V_L of each sample and the visibility to the zero bias value ν_0. With this scaling the curves for the two samples coincide perfectly, suggesting that the lobe structure and dephasing is a general behavior of this kind of interferometers and differences in the maximum visibility and energy can be overcome by scaling regarding their size difference L, i.e. with ν_0 and V_L. This also means that these two samples are comparable for any following experiment on bias dependent dephasing.

With this the bias behavior of the interferometers alone is characterized. The next important part is QPC 0 as the noise source. As mentioned above QPC characteristics at such large magnetic fields can show resonances, due to a localozed state at the QPC tips, which can lead to strong nonlinearities in current voltage characteristics. This would

make it impossible to asign a certain fixed transmission to QPC 0 for bias voltages up to $\pm 100\,\mu$V. The zero bias gate trace and a 2D gray scale plot of the differential conductance of QPC 0 for the case of sample B and the important bias voltage and gate voltage range is depicted in Fig. 6.2(c) and (d). Clearly, resonances are present which lead to certain nonlinearities for applied bias voltage, but we can choose gate voltages where these nonlinearities are minimal. This is either for large voltages $V_{\mathrm{QPC0}} > -285\,\mathrm{mV}$ or small ones $V_{\mathrm{QPC0}} < -335\,\mathrm{mV}$. For medium voltages where the peak and dip appear, the nonlinearities are too strong and an infuence on the experiment cannot be excluded. However, with the available gate range it is possible to cover all transmissions of QPC 0. In the following I will only refer to the transmission of QPC 0 and treat this transmission as energy indipendent.

6.1.2. Experiments on noise detection with a Mach-Zehnder interferometer

"Quantum weirdness is not only real - it is observable."

John Gribbin

After characterizing the Mach-Zehnder interferometers for $\mathcal{T}_0 = 1$, they are now investigated for different transmissions $\mathcal{T}_0$ of QPC 0. The result for the visibility is depicted in Fig. 6.3(a) for sample B. Important parameters are marked in the plot for $\mathcal{T}_0 = 0.88$. Those are the zero bias visibility ν_0, the maxima of the side lobes ν_{1st} and ν_{2nd}, and their positions as V_{1st} and V_{2nd}. The left column of the figure shows larger transmissions down to $\mathcal{T}_0 = 0.5$ with the dashed line marking the position of V_1 for $\mathcal{T}_0 = 1$. One can see that the positions of the lobes and nodes do almost not change, only the dephasing for large voltages seems to increase. This is visible from the decrease in the value of ν_{1st} and especially ν_{2nd}. The right column shows the behavior for smaller transmissions starting with $\mathcal{T}_0 = 0.5$ as a reference. For $\mathcal{T}_0 = 0.5$ the width of the lobes, i.e. the distance between nodes, seems to be comparable to the larger transmissions and the case for $\mathcal{T}_0 = 1$. For transmission $\mathcal{T}_0 < 0.4$ the central lobe width $2V_1$ increases slightly and the first side lobes are stretched over double the width as before. Additional (multiple) side lobes cannot be seen. For $\mathcal{T}_0 = 0.2$, the node position V_1 increases even more and the side lobes are stretched further to larger bias voltages, implying again a weaker dephasing. This means the lobe structure undergoes a drastic change; from a behavior with multiple side lobes for $\mathcal{T}_0 > 0.5$, which can be explained with the plasmon oscillations at $ff = 2$, to one with only single side lobes, where the oscillatory component ε_L vanishes and the bias dependent suppression of the coherent current leads to the side lobe (similar as explained in Sec. 2.6). This change appears around $\mathcal{T}_0 = 0.5$ and is the same for both samples that were investigated.

As seen in previous chapters another important signature of the lobe structure is its

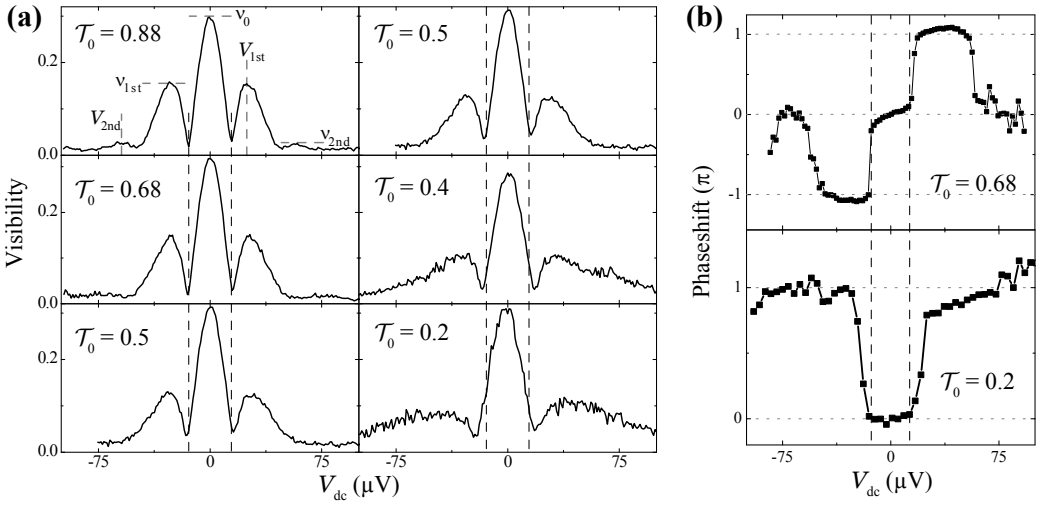

Figure 6.3.: (a) Lobe structure in the visibility for sample B for 5 different $\mathcal{T}_0$. $\mathcal{T}_0 = 0.5$ appears twice (bottom left and top right) as a reference for both larger (left) and lower transmissions (right). With decreasing $\mathcal{T}_0$ the height of the side lobes shrinks, while the positions stay constant, until the second side lobe cannot be discerned for $\mathcal{T}_0 = 0.5$. Even lower transmissions show only single, stretched side lobes and V_1 is gradually increasing. (b) Phase evolutions for two transmissions, $\mathcal{T}_0 = 0.68$ and 0.2, to cross-check the lobe structure in the visibility. Though barely discernible in the visibility, the phase evolution for $\mathcal{T}_0 = 0.68$ display clear jumps of a second node, indicating a second side lobe, unlike for $\mathcal{T}_0 = 0.2$.

phase behavior. Fig. 6.3(b) displays the AB-phaseshift of the lobe structure of sample B for two transmissions, $\mathcal{T}_0 = 0.68$ and 0.2. Especially for $\mathcal{T}_0 = 0.68$ we see that the second side lobes in (a) are barely visible, while they are still well descernible in the phase evolution in (b) due to the phase jump at the second nodes that clearly indicate V_2. Figs. 6.4(a) and (b) show the phase evolution for different $\mathcal{T}_0$ for sample A. The color plot of the phase shift as a function of $V_{\rm dc}$ and $\mathcal{T}_0$ shown in (b) nicely depicts several steps as a function of $V_{\rm dc}$ in the phase evolution for $\mathcal{T}_0 > 0.5$ indicated by the stepwise change of colors. The situation at $\mathcal{T}_0 = 0.5$ is ambiguous, primarily in sample A, as I will explain more explicitly in Sec. 6.3. For smaller transmissions of QPC 0 only one step of the phase, corresponding to only a single side lobe can be seen. This illustrates the usefulness of the phase evolution to identify a change from a multiple side lobe behavior to a single side lobe one. While in the visibility a second side lobe might be barely visible, even with a signal almost buried in noise, a jump by π is very apparent in the phaseshift.

Naively one would expect two effects when reducing the transmission of QPC 0. One is that the dephasing from the noise of QPC 0 should be highest at $\mathcal{T}_0 = 0.5$ and zero towards transmissions 1 and 0. This effect can be seen qualitatively in Fig. 6.3, namely

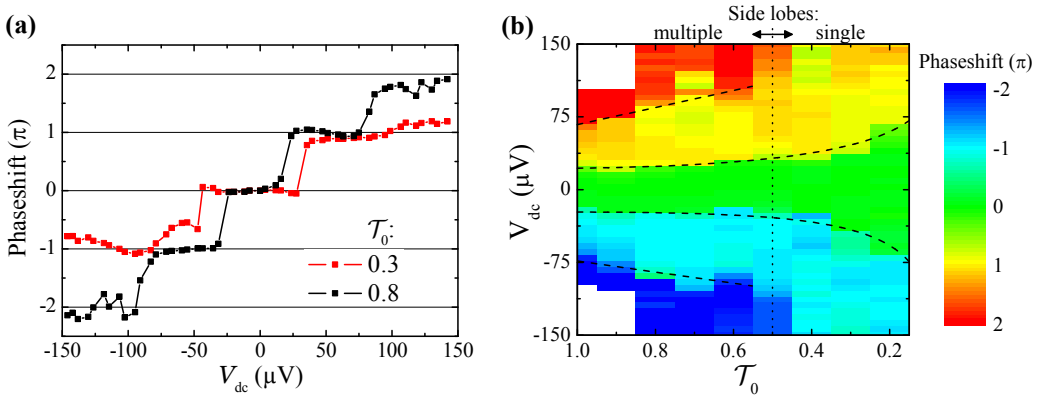

Figure 6.4.: Lobe structure in terms of the phase evolution for sample A. (a) Phase shifts for $\mathcal{T}_0 = 0.8$ and $\mathcal{T}_0 = 0.3$. Multiple steps, i.e., multiple side lobes for large transmissions and single steps, single side lobes for low transmissions are observed. (b) Phase evolution for different $\mathcal{T}_0$ in a 2D color scale plot. Dashed lines are guides to the eye to visualize the evolution of the nodes, i.e., the side lobes. The dotted line marks the transition at $\mathcal{T}_0 = 0.5$ from a behavior with multiple side lobes to one with single side lobes.

by the suppression of the visibility being strongest for $\mathcal{T}_0 = 0.5$, so that it is already zero at approximately 75 μV, where it is still finite for larger and smaller transmissions. Secondly, closing QPC 0 leads to a dilution of the edge channel, which might lead to a less effective bias voltage, because QPC 0 reduces the number of non-equilibrium electrons from N to an average number of $\langle n \rangle = \mathcal{T}_0 N$. This should then lead correspondingly to a stretching of the lobe structure, as seen in Eq. 5.14 when exchanging N with $\langle n \rangle$,[1] i.e., a movement of the nodes V_m to larger bias voltages, proportional to $\mathcal{T}_0$. However, the lobe structure behaves completely unexpected. At first the node positions stay almost constant until $\mathcal{T}_0 = 0.5$ and then abruptly the second nodes (and the second side lobe) disappear and the single side lobe structure gets more and more extended.

To illustrate the disappearance of multiple side lobes, the maximum of the second side lobe ν_{2nd} is depicted in Fig. 6.5(a) as a function of $\mathcal{T}_0$. The curve is normalized to the value of ν_{2nd} at $\mathcal{T}_0 = 1$. One clearly sees an almost linear decrease of ν_{2nd} towards $\mathcal{T}_0 = 0.5$. To precisely get ν_{2nd} for the small values close to $\mathcal{T}_0 = 0.5$ a sinusoidal fitting was used as described in Section 5.3.2 and shown in Fig. 5.8. For $\mathcal{T}_0 < 0.5$ only oscillations of one side lobe are seen at voltages larger than the first node and the height of the second side lobe is then taken as zero. From the investigation of the node height it seems as if the second side lobe vanishes smoothly. Another possibility to investigate this is to look at the presence of nodes. For the case of multiple side lobes, there are multiple nodes. If only one side lobe is present, only a single node is observed. Fig. 6.5(b)

[1] $\cos(\pi N) \to \cos(\pi \langle n \rangle) = \cos(\pi \mathcal{T}_0 N) = \cos(e\mathcal{T}_0 V_{\mathrm{dc}} L / 2\hbar v)$

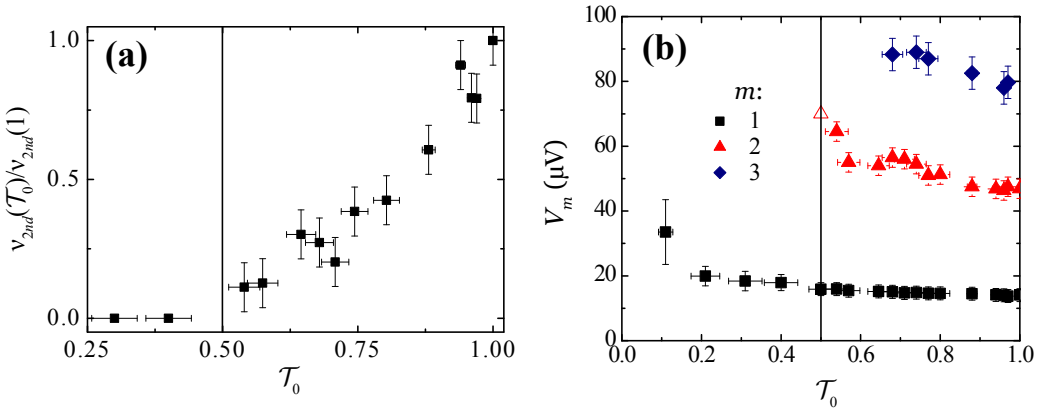

Figure 6.5.: (a) Height of the second side lobe for various transmissions of QPC 0 (black squares) for sample B. It decreases gradually towards $\mathcal{T}_0 = 0.5$ and is zero below (no second side lobe present). (b) Node positions V_m vs. QPC 0 transmission for sample B. The first node (V_1, black squares) stays constant for transmissions bigger 0.5 and gradually moves to larger V_{dc} for decreasing $\mathcal{T}_0$ below 0.5. The second (red triangles) and third (blue diamonds) node shift slowly and disappear completely for $\mathcal{T}_0 < 0.5$.

shows the positions in terms of voltage V_m at which nodes are present. This is evaluated both from visibility and phase evolution, where nodes are clearly discernible even for small visibilities. The first node V_1, stays almost constant for $\mathcal{T}_0 > 0.5$ when there are several nodes present. Only for transmissions $\mathcal{T}_0 < 0.5$, when there is just a single side lobe, the node at first slowly then faster with further decreasing transmission moves to higher energies. The second (and third) nodes move slowly to larger energies when decreasing the transmission down to $\mathcal{T}_0 = 0.5$ where they disappear abruptly. This sudden vanishing of the additional nodes indicates a defined transition.

6.2. Theoretical model of a noise-induced phase transition

"Not only is the Universe stranger than we think - it is stranger than we can think."

Werner Heisenberg

In similar experiments noise was introduced in the inner edge channel, which runs parallel to one interferometer channel of one arm, by setting QPC 0 to $1 < \mathcal{T}_0 < 2$ [92,93]. Though the experiments were the same in both cases, the results were quite different. The experiment in Ref. [93] showed an exponential suppression of visibility with V_{dc}

and could be explained by a Gaussian noise distribution of QPC 0. On the contrary, Ref. [92] reported a lobe structure in the dependence on bias voltage, leading to a particular V-shaped dependence for $\nu(\mathcal{T}_0)$ for certain voltages. This was attributed to the contribution of higher moments of a binomial, i.e., non-Gaussian distribution, which can only be detected, when the coupling λ to the detector, the interferometer, is strong enough ($\lambda \geq \pi$) [94]. However, the situation in the experiment discussed here, where noise is directly introduced into the interferometer channel itself, is different and we need a theory that accounts for that in order to explain the extraordinary behavior of the present experiment.

In this section I will describe a simplified picture of the theoretical model by I. Levkivskyi and E. Sukhorukov of Ref. [35] that describes our experiment. It is based on the theory of plasmonic excitations that can explain multiple side lobes in the bias dependence of the visibility at $\mathit{ff} = 2$ [31] (see Sec. 5.3.2), but with an additional QPC 0 at a distance D upstream of the Mach-Zehnder interferometer QPC 1. This QPC 0 produces non-equilibrium noise as described in Sec. 2.4. In the case of $\mathcal{T}_0 = 1$ the number of electron wave packets in an interferometer arm due to a voltage V_{dc} was given by the zero mode $N = eV_{\mathrm{dc}}L/2\pi v$ (see Sec. 5.3.2). This changes for transmissions $\mathcal{T}_0 < 1$ and the number of wave-packets, n in the edge channel fluctuates between 0 and $N = eV_{\mathrm{dc}}L/2\pi v$ with probabilities $P(n)$ and can be investigated by means of the full counting statistics (FCS).

In this system with two edge channels $\alpha = 1,\ 2$ and the two interferometer arms $s = U,\ D$ the current fluctuations flowing out of QPC 0 can be described with a generator of the FCS similar to Eq. 2.56

$$\chi_{s\alpha}(\lambda,\ t) = \sum_{n=0}^{N} P(n,t)e^{i\lambda n} = \langle e^{i\lambda N_{s\alpha}(t)} e^{-i\lambda N_{s\alpha}(0)} \rangle \tag{6.1}$$

through which the moments of the current can be expressed as $\partial_{i\lambda}^n \ln(\chi_{s\alpha})/t = \langle I_{s\alpha}^n \rangle$. As mentioned in Sec. 2.4, the connection between the current $I(t)$ and boson fields can be deduced from the charge density $\rho(t)$ and the continuity equation and leads to the boundary condition

$$\partial_t \Phi_{s\alpha}(t) = 2\pi I_{s\alpha}(t). \tag{6.2}$$

With this one can express the correlation function for the boson fields $\Phi_{s\alpha}$ in terms of the moments of the current fluctuations, $\langle I_{s\alpha}^n \rangle$, and thus by the generator Eq. 6.1. The counting field λ, which also plays the role of the coupling to the detector, has a large value of $\pm\pi$ due to the long-range Coulomb interaction in the case of a quantum Hall edge state at $\mathit{ff} = 2$. Thus, higher order cumulants cannot be neglected.

The voltage bias behavior of the Mach-Zehnder interferometer is influenced by the current fluctuation originating from QPC 0. In recent publications both effectively Gaussian and non-Gaussian noise distribution were reported [92, 93]. Levkivskyi et al. give

analytic expressions for the Mach-Zehnder interferometer visibility in the asymptotic regime of large bias voltage for both noise distributions. For a noise distribution, where higher moments from the QPC current fluctuations are truncated, and thus becomes effectively *Gaussian*, this is

$$\nu(V_{\mathrm{dc}}) = \nu_0 \left| \frac{\partial}{\partial V_{\mathrm{dc}}} sin\left(\frac{\pi e V_{\mathrm{dc}}}{\varepsilon_L}\right) e^{-eV_{\mathrm{dc}}/\varepsilon_D} \right|, \tag{6.3}$$

$$\text{with} \quad \varepsilon_L = \frac{2\pi\hbar v}{\mathcal{T}_0 L}, \quad \varepsilon_D = \frac{4\hbar v}{\pi L \mathcal{T}_0(1-\mathcal{T}_0)}. \tag{6.4}$$

Here ε_L is again the characteristic energy of the lobe periodicity which now depends on the transmission $\mathcal{T}_0$ of QPC 0. The energy ε_D is a characteristic energy, that describes the decaying envelope of the lobe pattern, similar to what was previously expressed by ε_0. I choose a different notation, because ε_0 describes a dephasing arising from inelastic scattering inside the Mach-Zehnder interferometer itself, while ε_D is a dephasing originating from QPC 0. Eq. 6.3 is similar to the phenomenological formulas Eq. 5.7 and Eq. 5.8, with the energy scales of Eq. 6.4. This reflects our naive picture of how a variation of $\mathcal{T}_0$ influences the Mach-Zehnder interferometer. The dilution of the edge channel reduces the bias effectivity proportional to the transmission[2] and the lobe pattern gets stretched with decreasing transmission by $\varepsilon_L(\mathcal{T}_0)$ in Eq. 6.4. The dephasing is the known "$\mathcal{T}(1-\mathcal{T})-$behavior" as shown, e.g., in Ref. [93].

After this consideration of the effect of a Gaussian noise distribution on the Mach-Zehnder interferometer, now *all cumulants* of the current fluctuations are taken into account. As reported in Ref. [34] the non-equilibrium noise from a QPC has a *binomial distribution* $P(n) = C_N^n \mathcal{T}^n (1-\mathcal{T})^{N-n}$ with a generating function $\chi_{U1}(\lambda, t) = (\mathcal{R}_0 + \mathcal{T}_0 e^{i\lambda})^N$, where $N = eV_{\mathrm{dc}}t/2\pi = eV_{\mathrm{dc}}L/2\pi v$. For $\lambda = \pi$, one arrives at

$$\ln\left[\chi_{U1}(\pi, t)\right] = \frac{eV_{\mathrm{dc}}t}{2\pi\hbar}\left[\ln|\mathcal{T}_0 - \mathcal{R}_0| + i\pi\theta(\mathcal{T}_0 - \mathcal{R}_0)\right]. \tag{6.5}$$

The imaginary part is responsible for the lobe periodicity ε_L and the real part describes the dephasing ε_D. This becomes clearer when we look at the resulting visibility vs. dc bias. Still the Eq. 6.3 is valid, but with new energy scales

$$\varepsilon_L = \frac{2\pi\hbar v}{L\theta(\mathcal{T}_0 - \mathcal{R}_0)}, \quad \varepsilon_D = \frac{2\pi\hbar v}{L|\ln|\mathcal{T}_0 - \mathcal{R}_0||}. \tag{6.6}$$

For $\mathcal{T}_0 < 0.5$ the characteristic energy of the lobes $\varepsilon_L \to \infty$, because the step function θ switches zu zero, and Eq. 6.3 becomes

$$\nu(V_{\mathrm{dc}}) = \nu_0 |(1 - eV_{\mathrm{dc}}/\varepsilon_D) e^{-eV_{\mathrm{dc}}/\varepsilon_D}|. \tag{6.7}$$

The result can be seen in Fig. 6.6. For large transmissions $\mathcal{T}_0 > 0.5$ a multiple side lobe

[2] The argument of the circular function changes from $eV_{\mathrm{dc}}L/2\hbar v$ to $e\mathcal{T}_0 V_{\mathrm{dc}}L/2\hbar v$.

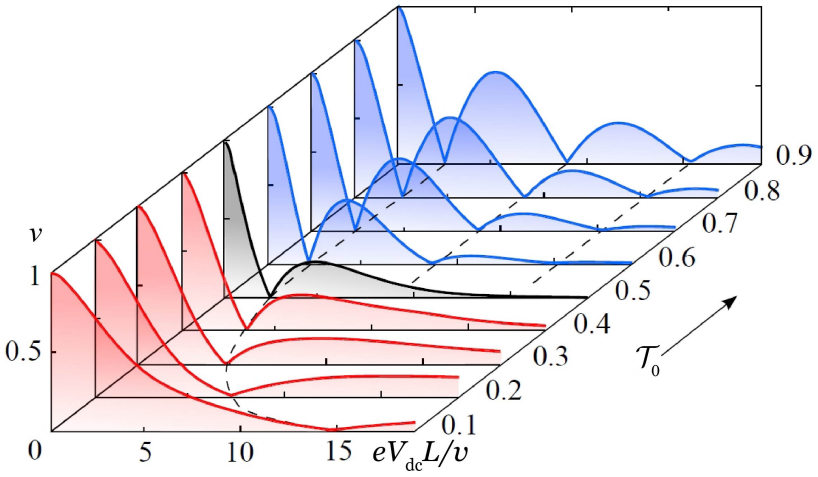

Figure 6.6.: The visibility of AB oscillations shown as a function of the normalized voltage bias for different transmissions $\mathcal{T}_0$. It is evaluated numerically using the Gaussian approximation at low bias, and FCS at large bias. The visibility shows several lobes for $\mathcal{T}_0 > 0.5$, while it has only one side lobe for $\mathcal{T}_0 < 0.5$. The black curve shows the visibility at the critical point of the phase transition. Dashed lines indicate the position of the nodes. (Reproduced from Ref. [35])

structure is expected with the same ε_L as for $\mathcal{T}_0 = 1$ and some additional dephasing given by ε_D. Below $\mathcal{T}_0 = 0.5$, only single side lobes are predicted (described by the switching of the step function in ε_L, see Eq. 6.7) and the remaining node is depending on the dephasing, i.e., ε_D. This change of behavior happens abruptly at a critical point $\mathcal{T}_0 = 0.5$, for large voltage bias, i.e., many particles and is induced by fluctuations, thus it has the characteristics of a phase transitions.
Simplifying the above equations even further will show more clearly how this phase transition works and what are the important parameters. Continuing with the model to explain multiple side lobes given in Eq. 5.14, now with n instead of N, and summing over all possible n weighted by their probabilities $P(n)$ of the binomial process we can write the visibility as

$$\begin{aligned}\nu(V_{\mathrm{dc}}) = \nu_0 \left| \sum_{n=0}^{N} P(n) \cos(\pi n) \right| = |Re\,\chi(\pi))| = \\ = \left|\cos(eV_{\mathrm{dc}}\theta(\mathcal{T}_0 - \mathcal{R}_0)L/2\hbar v)\right| e^{-eV_{\mathrm{dc}} \ln|\mathcal{T}_0 - \mathcal{R}_0| L/2\pi\hbar v}.\end{aligned} \tag{6.8}$$

Here, the sum over all possible configurations in the Mach-Zehnder interferometer, that contribute to the visibility, is identified as the real part of the FCS generator χ from Eq. 6.1 with $\lambda = \pi$. This is a direct connection between the FCS of the non-equilibrium noise produced in QPC 0 and the Mach-Zehnder interferometer visibility, which ana-

lytically leads to the described behavior of the lobe structure as a function of $\mathcal{T}_0$. In Eq. 6.8 the step function, in a manner of speaking, weights the bias voltage $V_{\rm dc}$ for different transmission. This can be regarded as the effectivity of the bias voltage $V_{\rm dc}$, which would be in the case for Gaussian noise, as seen in Eq. 6.4, simply the transmission $\mathcal{T}_0$. For $\mathcal{T}_0 > 0.5$, when only few electrons are reflected at QPC 0, the higher order cumulants, which are responsible for the step function, cancel the dilution effect as if the edge channel was still fully occupied and the oscillating bias voltage behavior is persistent. On the other hand for $\mathcal{T}_0 < 0.5$, when only few electrons are transmitted, it cancels the effect of the remaining electrons and the oscillatory component in $V_{\rm dc}$ is completely lost. In terms of a phase transition the step function can be regarded as the order parameter. The second effect of the non-Gaussian distribution concerns the dephasing at large voltage bias. The smooth $\mathcal{T}_0(\mathcal{T}_0 - 1)$ behavior is lost, instead there is a logarithmic characteristic leading to a divergence of the dephasing at the critical transmission $\mathcal{T}_0 = 0.5$. This represents a perfect quantum measurement, i.e., perfect entanglement between the non-equilibrium electrons originating from QPC 0 and those that contribute to the oscillations in the interferometer.[3]
The analytic formulas described here, which are only valid asymptotically for large $V_{\rm dc}$, imply a perfectly sharp transition. However, quantum corrections and the finite size of the electron wave packets lead to a smearing out of this transition. To go beyond the asymptotic behavior shown above, numerical calculations are required and all the following comparisons of experiment and theory are done with the numerical data produced by Ivan P. Levkivskyi as described in Ref. [32].

To verify whether the experiment shows this phase transition, the effectivity of the bias ($\propto 1/\varepsilon_L$), i.e., the order parameter, and the dephasing ($\propto 1/\varepsilon_D$) are extracted from the data in the following way. The effectivity of the bias manifests in the period of the oscillating visibility, i.e. in the inverse of $\varepsilon_L(\mathcal{T}_0)$ (see Eq. 6.6). The simplest way to extract this from the experiment is the distance between adjacent nodes as in Fig. 6.5, $\varepsilon_L = e(V_{m+1} - V_m)$. Then we obtain the effectivity of the bias by the fraction $\varepsilon_L(1)/\varepsilon_L(\mathcal{T}_0)$, which would be ideally the step function [see dotted line in Fig. 6.7(a)]. In the case of Gaussian noise, when no phase transition occurs, this would be equal to the transmission, $\mathcal{T}_0 = \varepsilon_L(1)/\varepsilon_L(\mathcal{T}_0)$ [see dashed line in Fig. 6.7(a)]. Fig. 6.7(a) shows the exact theoretical expectations together with experimental data points. The data from the experiment lie slightly closer to the non-Gaussian theoretical prediction, but with the large error bars this statement alone would not be very strong. On the other hand, more important is actually the fact, that there are no data points for $\mathcal{T}_0 < 0.5$. The dashed line in Fig. 6.7(a) is the expected evolution of this parameter for Gaussian noise and the gray shaded region marks the limits of the accessible bias range. As one can see, there is a range of $\mathcal{T}_0 < 0.5$, where one still would be able to measure point, that follow the Gaussian prediction, which were experimentally not found. This is also clearly

[3] *Entanglement* is the third of the seven wonders of the quantum world [44] in this thesis.

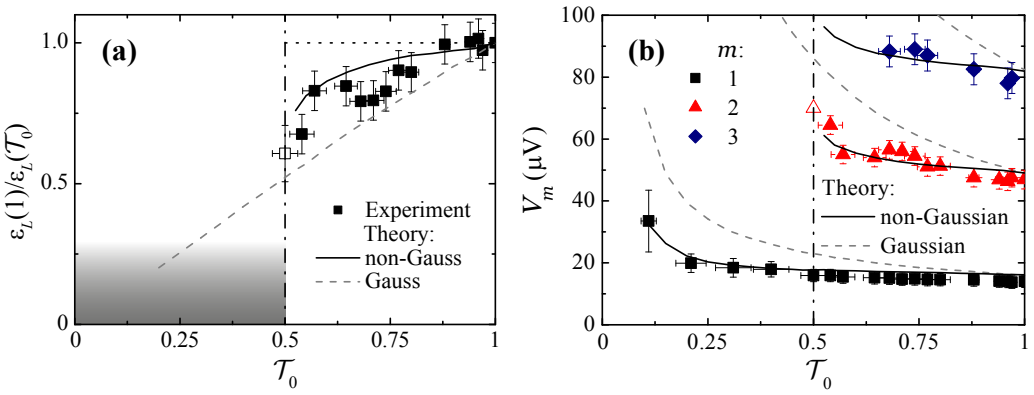

Figure 6.7.: (a) The order parameter of the phase transition $\varepsilon_L(1)/\varepsilon_L(\mathcal{T}_0)$ vs. $\mathcal{T}_0$. The experiment (black squares) resembles the non-Gaussian prediction (numerics: solid line, Eq. 6.6: dotted line), especially for $\mathcal{T}_0 < 0.5$, where Gaussian prediction (gray dashed line) is still finite. The gray region displays the not accessed bias voltage. (b) Node positions as in Fig. 6.5(b) together with the according numerical calculations for Gaussian (dashed) and non-Gaussian noise. Theoretical curves are scaled with the voltage V_L at $\mathcal{T}_0 = 1$. The open symbols in (a) and (b) are the according experimental values for $\mathcal{T}_0 \approx 0.5$.

visible in Fig. 6.7(b), where the node positions V_m are depicted as a function of $\mathcal{T}_0$ as in Fig. 6.5(b) (symbols), together with their calculated values for non-Gaussian (straight line) and Gaussian noise (dashed line). This reveals clearly the agreement between the experiment and the non-Gaussian prediction.
The second parameter, the dephasing $1/\varepsilon_D = 1/eV_D$, is more difficult to gain from the data. While node positions can be seen very precisely in visibility and phase evolution, the diverging dephasing can only be obtained from the visibility at certain points for large bias voltages. However, there the visibility is very small and the signal to noise ratio is bad, especially for small transmissions $\mathcal{T}_0$ where the relative noise in the visibility increases due to the small measured conductance of the raw data. For $\mathcal{T}_0 > 0.5$ the dephasing parameter is obtained via $\nu_{2nd}(\mathcal{T}_0)/\nu_{2nd}(1)$. At a lobe maximum the oscillatory component is ~ 1 and the relative lobe height is mainly determined by the dephasing ε_D. Exploiting the exponential characteristic of the asymptotic form Eq. 6.8, one takes the negative logarithm and divides by the voltage of the maximum position V_{2nd}:

$$\nu_{2nd}(\mathcal{T}_0)/\nu_{2nd}(1) = e^{-V_{2nd}/V_D} \Rightarrow 1/V_D(\mathcal{T}_0) = -\ln(\nu_{2nd}(\mathcal{T}_0)/\nu_{2nd}(1))/V_{2nd} \qquad (6.9)$$

For $\mathcal{T}_0 < 0.5$ there are two alternatives to approximately determine the dephasing parameter. One is to fit the high bias regime of the visibility curves exponentially and thus get $1/V_D(\mathcal{T}_0)$. The advantage of this method is that here we expect the divergence at $\mathcal{T}_0 = 0.5$, the disadvantage is that the fitting parameter V_D is very sensitive to small offsets and the noise of the visibility in this bias range. The second method is based on

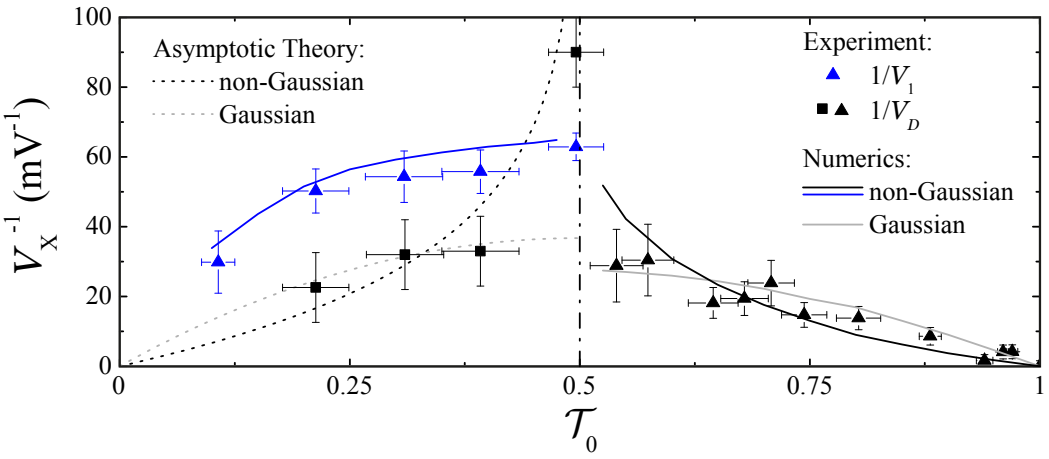

Figure 6.8.: The dephasing is evaluated as the prefactor $e/\varepsilon_L = 1/V_D$ of the argument of an assumed exponential decay at large $V_{\rm dc}$ as in Eq. 6.6 and 6.8. For $\mathcal{T}_0 > 0.5$ this is evaluated from the height of the second side lobe ν_{2nd}. This is done the same way for experimental (black triangles) and numerical Gaussian (gray line) and non-Gaussian (black line) curves. For $\mathcal{T}_0 \leq 0.5$ the dephasing is gained in two different ways: $1/V_1$ represents the low bias dephasing in the case of single side lobes; experiment (blue squares) and numerics fit nicely (blue line). From curves with a single side lobe $1/V_D$ can be obtained from an exponential fit at large bias of the visibility. Here we see a pronounced peak close to $\mathcal{T}_0 = 0.5$ which follows the asymptotic behavior of Eq. 6.6 (black dashed line). Gray line is the asymptotic for Gaussian noise.

the asymptotic form of Eq. 6.7 which implies that the node position V_1 is equal to V_D. The benefit here is that node positions can be determined very accurately, but on the other hand at low voltages as V_1 the divergence of the dephasing at $\mathcal{T}_0 = 0.5$ cannot be seen. Additionally both ways to obtain the dephasing parameter for $\mathcal{T}_0 < 0.5$ already imply that there is only a single side lobe.

Fig. 6.8 illustrates the discussed dephasing. For $\mathcal{T}_0 > 0.5$ the experimental data is compared with the theoretical predictions of Gaussian and non-Gaussian noise. The numerical curves for $\nu(V_{\rm dc})$ are evaluated concerning ν_{2nd} in the same way as the experimental curves. In this transmission range it is not obvious within the error bars whether Gaussian or non-Gaussian prediction fits the data better. For $\mathcal{T}_0 < 0.5$ the blue symbols and curve display the data and the numerical prediction for non-Gaussian noise for V_1. The agreement is very good and the dephasing is considerable larger than the Gaussian prediction from Eq. 6.4 (gray dotted line in Fig. 6.8). However, there cannot be a sensible comparison with Gaussian predictions, because striclty speaking Eq. 6.4 is only valid for large bias voltages, whereas V_1 appears at small voltages. In addition to V_1, the dephasing parameter V_D is extrapolated from exponential fitting. The mentioned

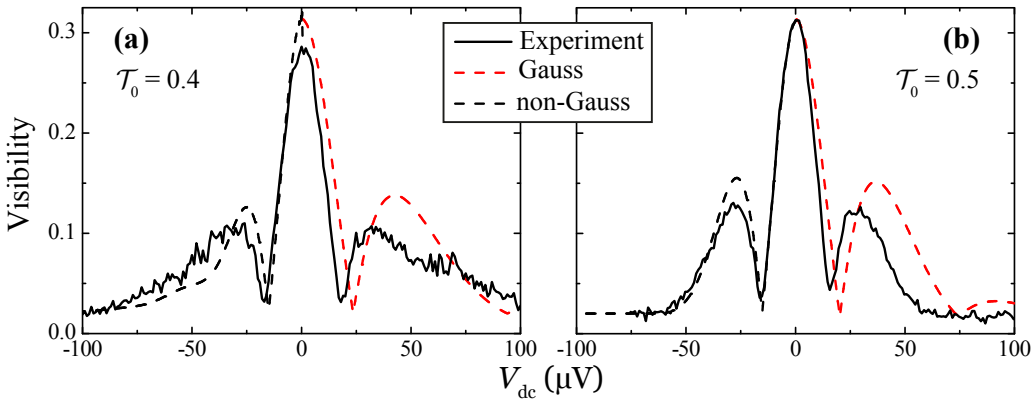

Figure 6.9.: Lobe structure of the visibility of sample B for $\mathcal{T}_0 = 0.5$ (a) and $\mathcal{T}_0 = 0.4$ (b) (black straight lines). Dashed black line represents the expected curve for non-Gaussian dephasing and red dashed line for Gaussian. The theoretical curves are fitted to $\nu_0(\mathcal{T}_0 = 1)$ and $V_L(\mathcal{T}_0 = 1)$. Comparison of $\mathcal{T}_0 = 0.5$ and 0.4 shows the drastical change of lobe structure at $\mathcal{T}_0 = 0.5$. Comparison with theory shows that the measured lobe structure can be fitted best by curves for non-Gaussian noise.

sensitivity of the fits to noise and offsets results in large error bars (black squares in Fig. 6.8). The dotted lines in Fig. 6.8 represent $1/V_D = e/\varepsilon_D$ from Eqs. 6.4 and 6.6 with the experimentally determined v and L. Thus, without any free fitting parameter the aggreement is very good, and the experiment shows the divergence of the dephasing for large bias voltages $V_{\rm dc}$.

To further illustrate the agreement to the non-Gaussian predictions and the phase transition, Fig. 6.9 shows numerical and experimental curves of $\nu(V_{\rm dc})$ for $\mathcal{T}_0 = 0.4$ (a) and 0.5 (b). The fitting parameters to scale the curves are $\nu_0(\mathcal{T}_0 = 1)$ and $V_L(\mathcal{T}_0 = 1)$ together with the theoretical evolution $V_1(\mathcal{T}_0)$. On the one hand we see the distinct difference of the side lobe in the experiment between the transition $\mathcal{T}_0 \approx 0.5$ and a slightly smaller transmission $\mathcal{T}_0 = 0.4$, indicating the change of characteristics. And on the other hand Fig. 6.9 clearly shows how this difference in the fundamental shape can also be seen in the non-Gaussian prediction, but not in the Gaussian one and how well the non-Gaussian prediction resembles the experiment. It is especially the node position V_1, that coincides extremely well for the experiment and the theoretical prediction of the noise induced phase transition. Additionally, the shape of the side lobe changes from narrow, with higher lobe maximum ($\mathcal{T}_0 \geq 0.5$), to a rather flat, but wide side lobe. With only two fitting parameters [$\nu_0(\mathcal{T}_0 = 1)$ and $V_L(\mathcal{T}_0 = 1)$] one can describe a set of $\nu(V_{\rm dc})$ for various $\mathcal{T}_0$.

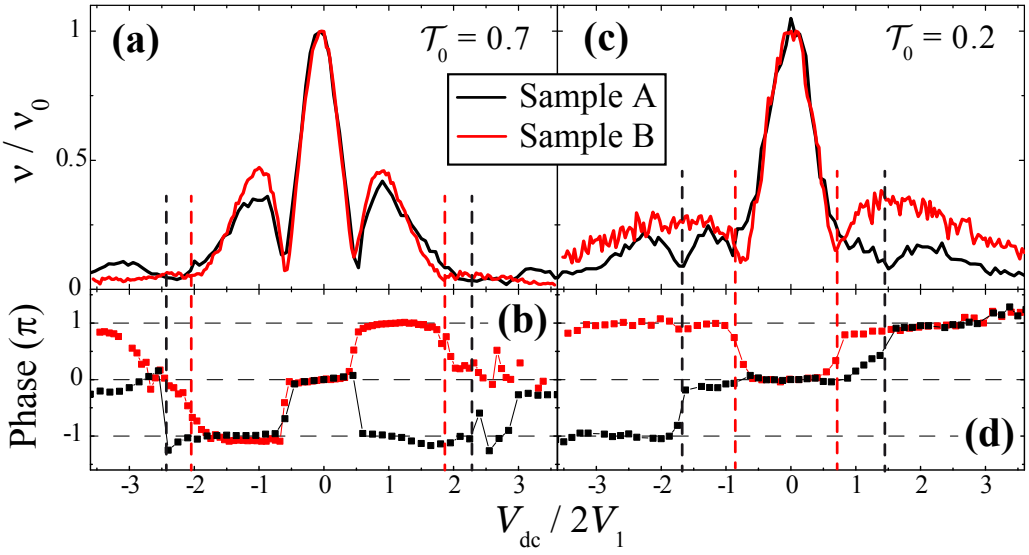

Figure 6.10.: Lobe structure for $\mathcal{T}_0 = 0.7$ (a) and $\mathcal{T}_0 = 0.2$ (c) for sample A (black line) and sample B (red line) and corresponding phase evolution in (b) and (d). To be able to compare the curves the visibility is scaled to ν_0 of each sample and the voltage to $V_1(1)$. Dashed lines mark V_2 in (a) and (b) and V_1 in (c) and (d) to highlight discrepancies between the samples.

6.3. Discussion

As seen above, the experiment was conducted for two samples and qualitatively both showed the same result. Though exact comparisons and fittings to theory are only carried out for sample B. I want to discuss this further and have a closer look at sample A. As Fig. 6.2 shows, the bias behavior of the two samples scales perfectly with respect to ν_0 and V_L for $\mathcal{T}_0 = 1$. That means that the intrinsic mechanisms that lead to the multiple lobe structure and the dephasing are the same despite their different interferometer sizes L. In contrast to that, the comparability is lost when QPC 0 is detuned from $\mathcal{T}_0 = 1$ as illustrated in Fig. 6.10. For large transmissions $\mathcal{T}_0 = 0.7$ the curves still coincide for small bias voltages, i.e., first node and lobe. However, the transmission dependent shifting of the second node $V_2(\mathcal{T}_0)$ is much stronger for sample A, indicated by the red and black dashed lins. The discrepancy is even stronger for $\mathcal{T}_0 = 0.2$. Although single side lobes can be seen in both samples at this transmissions, their shape is very different. Here even the first node in sample A appears at much larger voltages, implying smaller dephasing. In contrast to that, the side lobe decays much faster in sample A than in sample B, indicating differences in the dephasing properties.

A detailed study for all transmissions $\mathcal{T}_0$ reveals more ambiguities of sample A (see

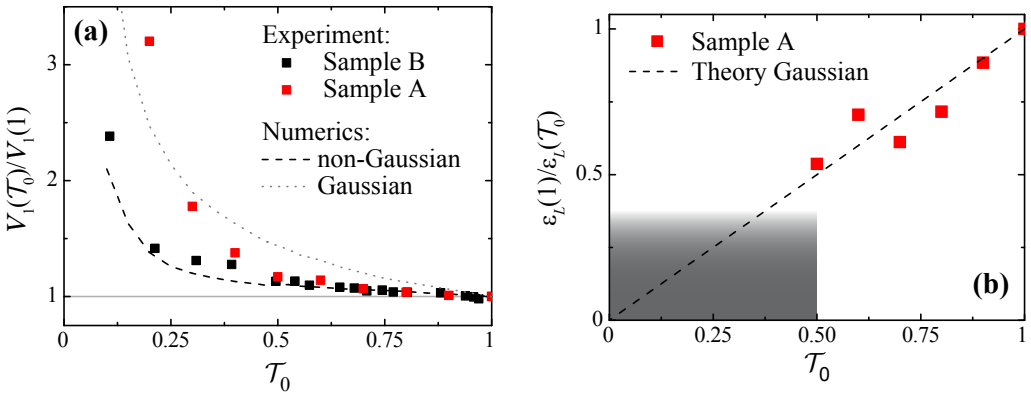

Figure 6.11.: (a) Evolution of V_1 for samples A and B together with the numerical calculations for Gaussian and non-Gaussian noise. Sample A resembles non-Gaussian behavior for large transmissions $\mathcal{T}_0 > 0.5$, but approaches Gaussian at low transmissions when it increases exceedingly. (b) The order parameter $\varepsilon_L(1)/\varepsilon_L(\mathcal{T}_0)$ of sample A follows the Gaussian prediction.

Fig. 6.11). Whereas $V_1(\mathcal{T}_0)$ for both samples agrees very well with the non-Gaussian prediction for $\mathcal{T}_0 > 0.5$, the data of sample A gets detached for further decreasing $\mathcal{T}_0$ and approaches the Gaussian prediction. It seems as if there is a cross-over from non-Gaussian to Gaussian behavior. The evolution for the bias effectivity [Fig. 6.11(b)], which is related to V_2 that occurs at large voltages[4], shows an agreement with the Gaussian prediction. However, there is still a qualitative agreement to non-Gaussian behavior, because additional side lobes are not observed for $\mathcal{T}_0 > 0.5$, which is also reflected in the fact that a effectivity of the bias cannot be determined here. Though, as the gray shaded region in Fig. 6.11(b) illustrates, the second node V_2 for a possible Gaussian behavior would be at very large bias voltages and on the border of the accessed bias range, which further complicates to classify whether sample A show rather Gaussian or non-Gaussian behavior.

Another very good example for the ambiguity of sample A is a fit of a lobe structure with theory curves as shown in Fig. 6.12 for $\mathcal{T}_0 = 0.4$. Node position V_1 and side lobe height does neither fit well to the non-Gaussian nor Gaussian prediction. Note that the same kind of plot was done in Fig. 6.9(a) for sample B, which showed excellent aggreement for non-Gaussian noise.

Although the behavior with $\mathcal{T}_0$ seems qualitatively similar for both samples it is quite puzzling to find this clear deviations from the non-Gaussian prediction for sample A.

[4]The effectivity of the bias is defined as the inverse of the bias oscillation period, scaled to its value at $\mathcal{T}_0 = 1$, $\varepsilon_L(1)/\varepsilon_L(\mathcal{T}_0)$ and $\varepsilon_L = e(V_2 - V_1)$. Since $V_1 \approx$ const. for $\mathcal{T}_0 > 0.5$, $\varepsilon_L(\mathcal{T}_0)$ is mostly determined by V_2, and this shows pronounced discrepancies between the samples.

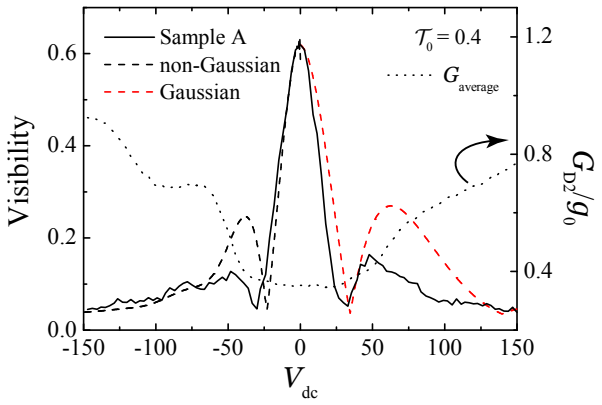

Figure 6.12.: Visibility vs. V_{dc} for $\mathcal{T}_0 = 0.4$ of sample A (solid black line) together with the results of numeric calculation. Both predictions for Gaussian (red dashed line) and non-Gaussian (black dashed line) distribution do not reproduce the lobe structure, indicating an intermediate state where higher order cumulants are already reduced, but not yet completely suppressed to be effectively Gaussian. The dotted curve is the average conductance $G_{average}$, which shows the strong nonlinearities of the IV characteristic at larger bias voltages.

From the fact that the lobe structures are so comparable for $\mathcal{T}_0 = 1$ we can conclude that the noise source QPC 0 is the origin of this discrepancy.
As mentioned in the first section of this chapter for sample B it was carefully checked to work QPC 0 only at gate voltages V_{QPC0}, where nonlinearities due to the resonant states seen in the gate characteristic are negligible in the applied bias voltage range V_{dc}. In contrast, sample A shows strong nonlinear current voltage characteristics and this is shown in the average conductance displayed in Fig. 6.12, dotted line. This nonlinearities have several consequences. One possible consequence on the plasmon spectrum is discussed in the following paragraph. Apart from that, these nonlinearities influence the extracted visibility, which is defined as the amplitude, which seems to be less affected, devided by the average, which is directly connected to the nonlinear IV-characteristic. Thus the exact value of the visibility at large bias cannot be perfectly trusted. Next to the visibility, also the transmission is directly linked to the average conductance and becomes bias dependent $\mathcal{T}_0(V_{\mathrm{dc}})$, which complicates the task to identify a curve for a fixed gate voltage V_{QPC0} with a fixed transmission. This fact can be made clear, e.g., with the phase evolution at $\mathcal{T}_0 = 0.5$ as depicted for both samples in Fig. 6.13. At this transmission it is not expected from Ref. [35], that multiple side lobes appear. On the contrary, traces of second side lobes can be seen in the experimental results for $\mathcal{T}_0 = 0.5$. Especially for sample A, where they are fully developed. We see in Fig 6.13 a jump from 0 to π at the visibility node V_1. For larger voltages the phase shows an additional gradual

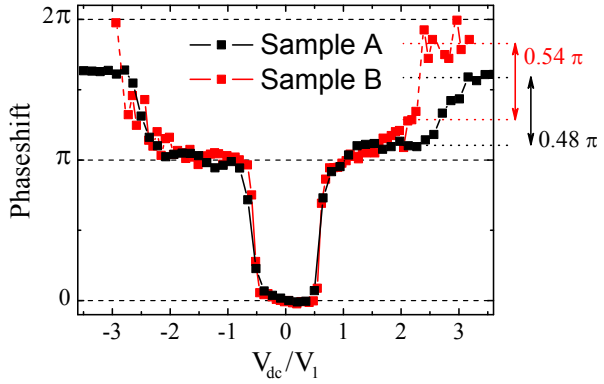

Figure 6.13.: For $\mathcal{T}_0 = 0.5$ (measured for $V_{\rm dc} = 0$) multiple side lobes are observed for sample A. In sample B only single side lobes are visible with a width similar to $\mathcal{T}_0 > 0.5$. The phase evolution shows in both samples a jump of π at the first node. In sample A we clearly see a further increase of the phase that saturates near $3\pi/2$. The second side lobes are pronounced. Sample B shows traces of a residual additional lobe with a similar phase behavior.

shift towards higher values for sample B, which cannot be explained in detail, but might be related to the transition at this transmission. However, sample A still shows good phase rigidity and a second slip of phase, indicating a second side lobe. On the one hand one can explain this be the change of average conductance towards larger values, resulting in a larger transmission for larger $V_{\rm dc}$, where still side lobes are present. In addition, the second jump of phase deviates strongly from its usual value of π and saturates already at $\pi/2$. This further highlights the unexpected behavior of sample A, compared to sample B and the theory. And it shows the influence of the nonlinear current voltage characteristic.

Further differences between the samples are, as already mentioned, the interferometer size L and the distance D between the Mach-Zehnder interferometer and QPC 0. The dimensions of sample B are in general larger by a factor of ~ 1.5, so that the ratio D/L is roughly the same. According to the theory only this ratio and not their absolute value is important [35]. Thus there has to be another reason why this kind of cross-over in noise behavior is observed for sample A.

Altimiras et al. reported about experiments on energy relaxation processes in the quantum Hall edge state at $ff = 2$ [95–97], where the energy distribution of an edge channel is probed by a quantum dot level. In Ref. [98] Levkivskyi et al. present a theoretical study of such experiments. Within the already presented theoretical approach it could be shown that higher order cumulants can be suppressed after a distance L_g and the originally non-Gaussian noise becomes effectively Gaussian. This can happen when the plasmon spectrum is not linear. Even if there is only a weak nonlinearity in the plasmon

spectrum as

$$k_j(\omega) = \omega/v_j + \gamma_j \omega^2 sign(\omega), \quad v_1 = u,\ v_2 = v, \tag{6.10}$$

which can barely be seen in the conductance, it can lead to a suppression of the higher order cumulants at distances

$$L_g = 1/\gamma(\mathcal{T}_0 e V_{\mathrm{dc}})^2 \tag{6.11}$$

when the wave packets of width $v/\mathcal{T}_0 e V_{\mathrm{dc}}$ overlap. This also implies, that for larger voltages the length scale L_g is reduced. Since the dimensions of the interferometer of sample A, compared to sample B, are smaller, the energy scales are larger and thus the applied bias voltages need to be are larger [$V_1(\mathrm{sample\ A}) > V_1(\mathrm{sample\ B})$]. This might explain that for small voltages the behavior of sample A is similar to sample B and to the non-Gaussian prediction, but with increasing bias voltage the sample gets into an intermediate regime where higher order cumulants are suppressed and the noise becomes almost Gaussian, or at least does not have a binomial distribution anymore. Thus we can state that we have in sample A a very nonlinear differential conductance of QPC 0, which might be a sign for a strong nonlinearity in the plasmon spectrum.
This raises the question, whether a detailed investigation of interferometers with various length scales L and D might lead to further insight, both on the equilibration of the edge states and on the question how and when non-Gaussian behavior of a QPC can be seen.

7. Summary

"The attempt to understand the universe is one of the only things that elevates the human condition from farce to the elegance of tragedy."

Stephen Weinberg, Nobel Laureate in Physics, 1979

This thesis deals with *dephasing*, i.e. loss of coherence and properties due to external parameters, of a Mach-Zehnder interferometer, and how these properties are changed by *quantum noise*. Thus the work is devided into two parts. The first chapter, chapter 5, shows experiments that display the transport properties of an electronic Mach-Zehnder interferometer itself, e.g. its behavior as a function of QPC transmission. The (almost) exponential dephasing with temperature and interferometer size L reveals a characteristic thermal energy $k_{\mathrm{B}}T_0$ that is proportional to the coherence length l_φ, which can be estimated to be $l_\varphi \approx 10\,\mu$m in the samples measured for this thesis. Another important property is the dephasing as a function of a dc bias voltage V_{dc}. Here, three different regimes could be identified. One is the case for filling factors close to 1, where only one edge channel is present throughout the sample. In this regime a lobe structure with single side lobes, next to a high central one, is observed, that is well described by the phenomenological model including Gaussian noise. This introduces an energy ε_0 describing the Gaussian decay. Possible microscopic explanations are intra-channel interactions along the interferometer arms of the collective modes of the Luttinger liquid. The other regimes appear close to $\not{f} \approx 2$. When only one of the two incoming edge channels (the outer, which is used for the interference) is biased by V_{dc} a lobe structure with multiple side lobes of equal widths arises. Two energy scales can be extracted from this behavior. One is the period of the oscillations vs. V_{dc}, ε_L, the second is an energy that describes the decaying envelope with increasing V_{dc}, ε_0. This overall dephasing with bias can be equally well approximated with an exponential and a Gaussian envelope and both give similar energies ε_0. These two energy scales, ε_L and ε_0, are approximately equal. The third regime is when both edge channels at $\not{f} = 2$ are biased with V_{dc}. Here, depending on the QPC transmission $\mathcal{T}_1$, either an increase of visibility at low bias voltages is observed, accompanied with a slow decay at large bias voltages, or a lobe structure with a central lobe of increased width is seen. The increase of visibility with bias could be explained by expanding a phenomenological model for single side lobes, with a term considering a second biased, capacitive coupled edge channel.
The coherence of the Mach-Zehnder interferometer is governed by the filling factor

$2 > ff > 1$. The zero bias visibility is zero for $ff > 2$ and $ff < 1$, with a smooth evolution in between, exhibiting a maximum at $ff \approx 1.5$. All the characteristic energy scales, $k_{\mathrm{B}}T_0$, ε_0 and ε_L, show the same characteristic, minimum values close to integer filling factors and a maximum at 1.5. And energy scales of the lobe structure, ε_0 and ε_L, are approximately equal and the characteristic thermal energy is proportional to this energy with a factor $\approx 2\pi^2$.
At the end of this chapter it is shown, that the versatile coherence properties are best explained with the theory by Levkivskyi et al. [31], where the long-range Coulomb interaction between co-propagating edge channels leads to the charge and dipole mode u and v. Especially, the lobe structure with multiple side lobes close to $ff \approx 2$ originates from the dynamical phase factors of the plasmon modes and their oscillation of phase information between adjacent channels. Additionally the proportionallity to $k_{\mathrm{B}}T_0$ with the factor $2\pi^2$ is predicted in this theory, and its connection to the coherence length l_φ. Furthermore, the expected evolution of the plasmon modes with filling factor fits with the expacted characteristic of the energy scales.

In the second chapter, chapter 6, of the experimental part, a novel non-equilibrium phase transition, which is induced by the non-Gaussian noise of a QPC and was predicted by Levkivskyi et al. [35], is demonstrated. In this experiment the Mach-Zehnder interferometer is used as a phase sensitive detector to the noise produced by an upstream placed QPC 0. For this purpose two samples are investigated. The order parameter of this phase transition is proportional to the normalized inverse of the lobe periodicity $\varepsilon_L(\mathcal{T}_0)$. It is shown, that it stays almost constantly one for $\mathcal{T}_0 > 0.5$, drops rapidly to zero at $\mathcal{T}_0 \approx 0.5$ and is zero below. This represents a transition, from a lobe pattern with multiple side lobes, i.e. a finite periodicity, to one with only a single side lobe, i.e. an infinite period. A second attribute of the transition that is verified is an almost diverging dephasing for large bias at $\mathcal{T}_0 = 0.5$. Additionally, lobe structures are directly compared to numerical calculations of this model with the non-Gaussian noise, i.e. all current cumulants, and Gaussian noise, where higher order cumulants are truncated. These numerical calculations are provided by Ivan Levkivskyi in the group of Eugene Sukhorukov in Geneva. One sample shows almost perfect overall agreement to the theory. The second sample exhibits only qualitative aggreement, but the discrepancies are well explained and can be mainly addressed to strong nonlinearities of the differential conductance of the QPC 0.

Summing up, dephasing in a Mach-Zehnder interferometer is investigated in detail, especially at finite bias voltages V_{dc}. An explanation for a majority of the observed effects is given either with phenomenological models, or in terms of the theory of plasmonic excitations of co-propagating channels of Luttinger liquid, coupled by long-range Coulomb interaction. Furthermore, a formerly predicted noise-induced phase transition is demonstrated.

A. Recipes

In chapter 4 an overview of the sample fabrication was given. Here, I present a reproduction of the exact fabrication procedure for future scientists, as it can be also found on the "Wikipedia" of the homepage of the chair of Prof. D. Weiss and Prof. C. Strunk [99]. This recipe was gathered by Leonid Litvin out of other recipes and optimized for the preparation of Mach-Zehnder interferometers., and only stlightly changed by me (e.g. testing different annealing times for different wafer material).

Standard Cleaning

- 1min Aceton in ultrasonic bath
- Keep chip wet with aceton when continuing in 2-3 more aceton baths
- Few seconds bathing in propanol (IPS) and blow with N2

Mesa Preparation

Spinning resist:

- Shipley (Microposit) 1805, $t = 30\,\mathrm{s}$; 4500 rpm
- 2 min, prebake 90°C hot plate

Exposure:

- Mask aligner, $t = 12\,\mathrm{s}$

Developement:

- H_2O : Microposit 351 = 4 : 1; $t = 50\,\mathrm{s}$

- stop in cascade bath; blow dry
- O_2 plasma $t = 5$ s, 30% power, 2 mbar
- postbake 110°C in oven, 3 min

Mesa etching:

- $H_2O : H_2O_2 : H_2SO_4$ = 100 : 1 : 3
- $\sim$110 nm $\rightarrow$ 100 s
- Lift off resist

Ohmic contacts

This step is optional. You can also do it with EBL.

Spinning resist:

- ARP 374-0; 3000 rpm, 5 s$\rightarrow$6000 rpm, 30 s
- prebake 6 min, 90°C
- or alternatively three layers of Shipley with each time prebake as shown above

Exposure:

- 30 s with CB; 18 s without CB
- Chlorbenzol (CB) step:
  - bath in CB $t = 3$ min
  - blow dry
  - 10 min oven at 85°C

Developement:

- H_2O : NaOH = 3 : 1, $t = 60$ s
- stop in cascade bath

- O_2 plasma
- HCl-Dip
- to remove native oxide
- HCl : H_2O = 1 : 1, $t = 30\,\mathrm{s}$

Evaporation of Au/Ge and Ni:

- Eutectic ratio: 88% Au (0.968 g), 12% Ge (0.132 g)
- $\rightarrow 200 - 250\,\mathrm{nm}$ (220 nm needed for $d = 100\,\mathrm{nm}$ deep 2DEG)
- Ni: 55 nm (25% of Au/Ge thickness)
- Lift off, 10 min in 90°C aceton, with jet of aceton, additional cold aceton and propanol...

Annealing:

- 1. step: 350°C; 120 s; type II
- 2. step: 450°C; 50 s; type II
- 3. step: 50°C; 2 s; type III
- Test contacts at "Spitzenmessplatz"
- Contact resistances should be around $30 - 50\,\mathrm{kOhm}$ and ohmic of course.

Leads for the gates

Spinning resist:

- S1805 as shown above

Exposure:

- $t = 40\,\mathrm{s}$ with CB coming
- CB step

Developement:

- As shown above

Evaporation:

- Cr or Ti; 5 nm
- Au; 150 nm
- Lift off

EBL Mesa

- Poly(methyl methacrylate) (PMMA) 50k, 9%, 8000 rpm, 30 s, prebake 150°C, 10 min
- Exposure 180 μC/cm^2, pixel exposure time $\sim$12 μs, I$\sim$20 pA
- Development IPS : MIBK = 3 : 1, 30 s

Wet etching:

- O_2 plasma ashing, 5 s
- Post bake 110°C, 30 min, oven
- H_2SO_4 : H_2O_2 : H_2O = 3 : 1 : 100, 1 min 20 s, depth ($\sim$50 nm) rpm 3, sample surface perpendicular to etch flow, (water bath <1 min)
- Resist removal: aceton 90°C, >3 min, aceton bath propanol bath, 90°C

EBL Ohmic contact

- PMMA/MA 33%, 8% in Ethyllactat, 3000 rpm, 100 s, prebake 150°C, 10 min
- Exposure 112 μC/cm^2, pixel exposure time $\sim$12 μs, I$\sim$20 pA, reserve 0.3 pA.
- Development: IPS : MIBK = 3 : 1, 30 s

AuGe Ni deposition:

- O2 plasma ashing, 5 s

- (Post bake 130°C, 30 min, oven)
- HCl : H_2O = 1 : 1, 30 s, (rpm 3, water bath ∼1 min)
- O.968 g Au, 0.132 g Ge; ∼220 nm AuGe, 55 nm Ni, for 90 nm deep 2DEG (optionally double thickness holder for deeper 2DEG)
- Lift off: aceton 90°C, >10 min, aceton bath propanol bath (90°C)

Annealing:

- 1. step: 350°C; 120 s; type II
- 2. step: 450°C; 50 s; type II (for small Ohmic contacts one has to test annealing time for each wafer and goes up to almost more than 120 s)
- 3. step: 50°C; 2 s; type III

EBL Gates

- PMMA 50k, 6%, 8000 rpm, 30 s, prebake 150°C, 10 min
- Exposure 218 μC/cm^2, pixel exposure time >12 μs, I∼10 pA, reserve 0.3 pA.
- Development IPS : MIBK = 3 : 1, 30 s

Au deposition:

- Cr adhesion layer 5 nm, Au 40 nm
- Lift off: aceton 90°C, >10 min, aceton bath propanol bath (90°C)

EBL Air bridges

- PMMA 950k, 4%, 4000 rpm, 30 s, prebake 150°C, 10 min
- PMMA/MA 33%, 8% in Ethyllactat, 3000 rpm, 100 s, prebake 150°C, 10 min
- Exposure 157 μC/cm^2, pixel exposure time >12 μs, I∼20 pA, 30 kV
- Development IPS : MIBK = 3 : 1, 30 s

Metal deposition:

- O_2 plasma ashing, 5 s
- Sample holder for double thickness, deposit 5 nm Cr + 150 nm Au $\times 2$
- Lift off: aceton 90°C, >10 min, aceton bath propanol bath 90°C

B. Important energy scales and their interrelation

In this thesis, a number of energy scales appear, that describe different aspects of the dephasing properties of the coherence inside the Mach-Zehnder interferometer. This appendix is meant as a reference to keep track of this "zoo" of energy scales and to show their interconnection. This task faces some problems, because so far their is no theory available that can explain each and every energy scale and its connections to the others. As carried out in this thesis the theory by Levkivskyi et al. is favored, and with it most connections can be explained.

Energy scale	**Description**	**Interrelation**
$k_{\mathrm{B}}T_0$	Characteristic thermal energy. $\nu(T) \propto (1 + T/T_0)\exp(-T/T_0)$	$k_{\mathrm{B}}T_0 = \varepsilon_0/2\pi^2 = \varepsilon_L/2\pi^2$, $T_0 \propto l_\varphi T/2L$
ε_0	Describing the decaying envelope of the lobe structure with bias voltage V_{dc} at $\mathcal{T}_0 = 1$. $\exp\left[-(eV_{\mathrm{dc}})^2/2\varepsilon_0^2\right]$, or $\exp\left(-eV_{\mathrm{dc}}/\varepsilon_0\right)$	$\varepsilon_0 = 2\pi^2 k_{\mathrm{B}}T_0 = \hbar v'/L$
eV_0	Voltage of the node of a single side lobe characteristic. $ff < 1.5$	$eV_0 = \varepsilon_0/2$ in the case of single side lobes.
$\varepsilon_L = eV_L$	Describing periodicity of the multiple side lobe characteristic. $ff < 1.5$, $V_L = V_m - V_{m-1}$	$\varepsilon_L(\mathcal{T}_0 = 1) \approx \varepsilon_0 = 2\pi^2 k_{\mathrm{B}}T_0$
ε	Energy scale from Ref. [31], that describes multiple side lobes for $\mathcal{T}_0 = 1$. $\varepsilon = \hbar v/L$	$\varepsilon = 2\pi\varepsilon_0$
ε_D	Describing exponential decaying envelope of the lobe structure for $\mathcal{T}_0 < 1$, $\exp(-eV_{\mathrm{dc}}/\varepsilon_D)$.	

Table B.1.: Important energy scales, their description and interrelation.

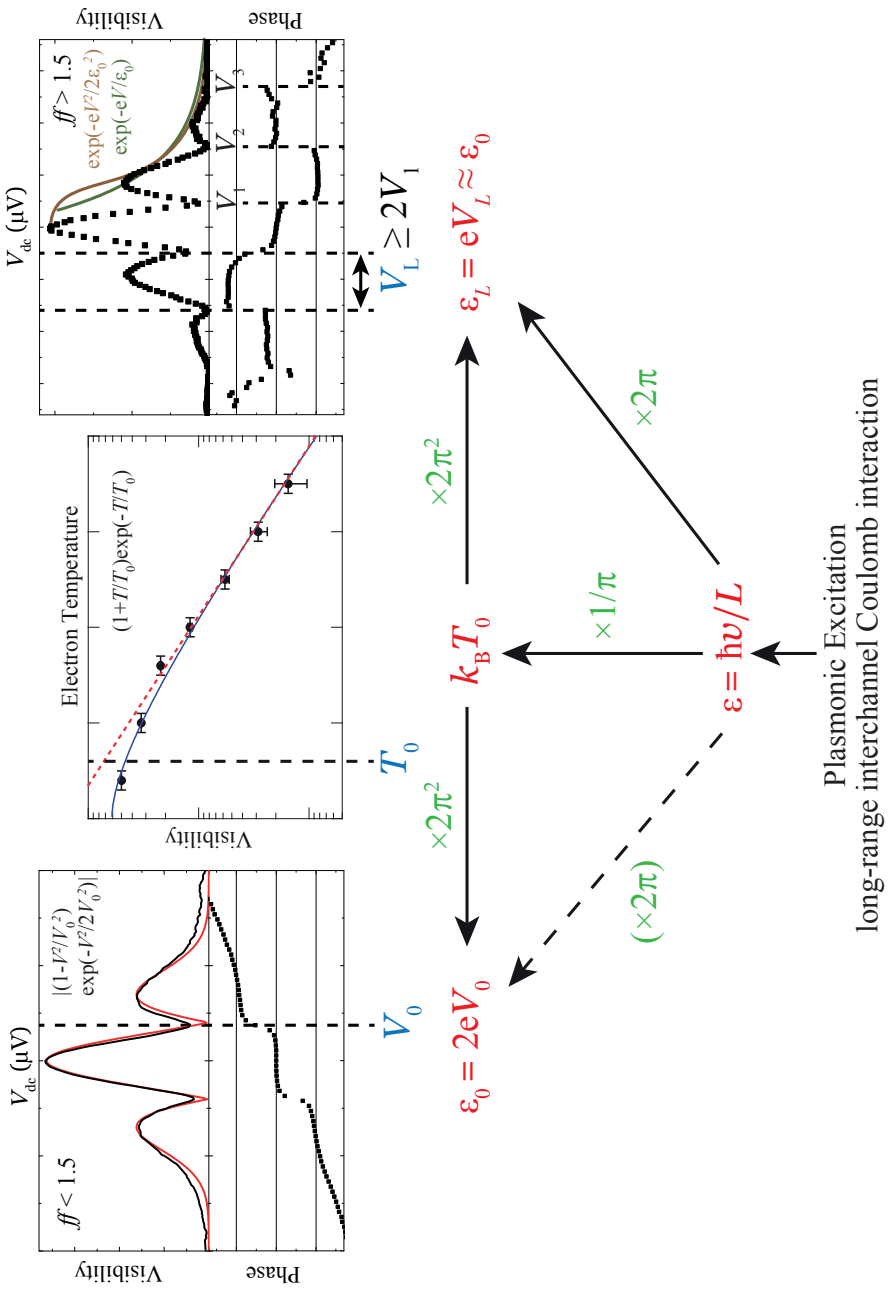

Figure B.1.: Visualization of most of the important energy scales and their interrelation described in Tab. B.1. Blue: Parameters from the experiment, together with typical measurements. Red: Corresponding energy scales. Green: Muliplicators, in connection with the arrow direction, indicate interconnection between the energy scales. Dashed arrow between ε and ε_0 of the single side lobe behavior denotes, that the plasmon theory does actually not make any prediction for a single side lobe pattern.

Bibliography

[1] M. Schlosshauer, "Decoherence, the measurement problem, and interpretations of quantum mechanics," *Rev. Mod. Phys.*, vol. 76, p. 1267, 2005.

[2] S. Kubatkin, A. Danilov, M. Hjort, J. Cornil, B. J. L., N. Stuhr-Hansen, P. Hedegård, and T. Bjørnholm, "Single-electron transistor of a single organic molecule with acess to several redox states," *Nature*, vol. 425, p. 698, 2003.

[3] S. Iijima, "Helical microtubules of graphie carbon," *Nature*, vol. 354, p. 56, 1991.

[4] Z. M. Wang, ed., *Self-Assembled Quantum Dots*. Springer, 2008.

[5] E. B. Foxman, P. L. McEuen, U. Meirav, N. S. Wingreen, Y. Meir, P. A. Belk, N. R. Belk, M. A. Kastner, and S. J. Wind, "Effects of quantum levels on transport through a Coulomb island," *Phys. Rev. B*, vol. 47, pp. 10020–10023, 1993.

[6] J. C. Licini, G. J. Dolan, and D. J. Bishop, "Weakly Localized Behavior in Quasi-One-Dimensional Li Films," *Phys. Rev. Lett.*, vol. 54, pp. 1585–1588, 1985.

[7] S. V. Morozov, K. S. Novoselov, M. I. Katsnelson, F. Schedin, L. A. Ponomarenko, D. Jiang, and A. K. Geim, "Strong suppression of weak localization in graphene," *Phys. Rev. Lett.*, vol. 97, p. 016801, 2006.

[8] A. A. Michelson and E. W. Morley, "On the Relative Motion of the Earth and the Luminiferous Ether," *American Journal of Science*, vol. 34, pp. 333–345, 1887.

[9] C. Jönssen, "Elektroneninterferenzen an mehreren künstlich hergestellten Feinspalten," *Zeitschrift für Physik*, vol. 161, pp. 454–474, 1961.

[10] A. Tonomura, J. Endo, T. Matsuda, T. Kawasaki, and H. Ezawa, "Demonstration of single-electron buildup of an interference pattern," *Am. J. Phys.*, vol. 57, pp. 117–120, 1989.

[11] M. Arndt, O. Nairz, J. Vos-Andreae, C. Keller, G. van der Zouw, and A. Zeilinger, "Wave-particle duality of C_{60} molecules," *Nature*, vol. 401, pp. 680–682, 1999.

[12] A. Yacoby, M. Heiblum, V. Umansky, H. Shtrikman, and D. Mahalu, "Unexpected Periodicity in an Electronic Double Slit Interference Experiment," *Phys. Rev. Lett.*, vol. 73, p. 3149, 1994.

[13] R. A. Webb, S. Washburn, C. P. Umbach, and R. B. Laibowitz, "Observation of h/e Aharonov-Bohm Oscillations in Normal-Metal Rings," *Phys. Rev. Lett.*, vol. 54,

p. 2696, 1985.

[14] F. E. Camino, W. Zhou, and V. J. Goldman, "Quantum transport in electron Fabry-Perot interferometers," *Phys. Rev. B*, vol. 76, p. 155305, 2007.

[15] Y. Ji, Y. Chung, D. Sprinzak, M. Heiblum, D. Mahalu, and H. Shtrikman, "An Electronic Mach-Zehnder Interferometer," *Nature*, vol. 422, p. 415, 2003.

[16] A. A. Clerk, M. H. Devoret, S. M. Girvin, F. Marquardt, and R. J. Schoelkopf, "Introduction to quantum noise, measurement, and amplification," *Rev. Mod. Phys.*, vol. 82, pp. 1155–1208, 2010.

[17] R. J. Glauber, *Quantum Theory of Optical Coherence: Selected Papers and Lectures*, ch. Chapter 8. Photon Statistics, pp. 140–187. Wiley-VCH, 2007.

[18] Y. M. Blanter and M. Büttiker, "Shot Noise in Mesoscopic Conductors," *Phys. Rep.*, vol. 336, p. 1, 2000.

[19] C. Beenaker and C. Schönenberger, "Quantum Shot Noise," *Physics Today*, vol. 56, p. 37, 2003.

[20] M. Reznikov, M. Heiblum, H. Shtrikman, and D. Mahalu, "Temporal Correlation of Electrons: Suppression of Shot Noise in a Ballistic Quantum Point Contact ," *Phys. Rev. Lett.*, vol. 75, p. 3340, 1995.

[21] L. DiCarlo, Y. Zhang, D. T. McClure, D. J. Reilly, C. M. Marcus, L. N. Pfeiffer, and K. W. West, "Shot-Noise Signatures of 0.7 Structure and Spin in a Quantum Point Contact," *Phys. Rev. Lett.*, vol. 97, p. 036810, 2006.

[22] M. Henny, S. Oberholzer, C. Strunk, and C. Schönenberger, "1/3-shot-noise suppression in diffusive nanowires," *Phys. Rev. B*, vol. 59, p. 2871, 1999.

[23] K. Kang, "Electronic Mach-Zehnder quantum eraser," *Phys. Rev. B*, vol. 75, p. 125326, 2007.

[24] S. Datta, *Electron transport in mesoscopic systems*. Cambridge University Press, 1995.

[25] K. von Klitzing, G. Dorda, and M. Pepper, "New Method for High-Accuracy Determination of the Fine-Structure Constant Based on Quantized Hall Resistance," *Phys. Rev. Lett.*, vol. 45, p. 494, 1980.

[26] D. B. Chklovskii, B. I. Shklovskii, and L. I. Glazman, "Electrostatics of edge channels," *Phys. Rev. B*, vol. 46, pp. 4026–4034, 1992.

[27] A. Siddiki and R. R. Gerhardts, "Incompressible strips in dissipative Hall bars as origin of quantized Hall plateaus," *Phys. Rev. B*, vol. 70, p. 195335, 2004.

[28] E. Ahlswede, P. Weitz, J. Weis, K. von Klitzing, and K. Eberl, "Hall potential profiles in the quantum Hall regime measured by a scanning force microscope,"

Physica B, vol. 298, pp. 562–566, 2001.

[29] M. Suddards, A. Baumgartner, M. Henini, and C. Mellor, "Scanning capacitance imaging of compressible and incompressible quantum Hall effect edge strips," *New J. Phys.*, vol. 14, p. 083015, 2012.

[30] T. Giamarchi, *Quantum Physics in One Dimension*. Oxford University Press, 2003.

[31] I. P. Levkivskyi and E. V. Sukhorukov, "Dephasing in the electronic Mach-Zehnder interferometer at filling factor $\nu = 2$," *Phys. Rev. B*, vol. 78, p. 045322, 2008.

[32] A. Helzel, L. Litvin, I. P. Levkivskyi, E. V. Sukhorukov, and C. Strunk, "Noise-induced Phase Transition in an Electronic Mach-Zehnder Interferometer - a Manifestation of Non-Gaussian Noise," *preprint arXiv:1211.5951*.

[33] S. Oberholzer, *Fluctuation Phenomena in Low Dimensional Conductors*. PhD thesis, Universitä t Basel, 2001.

[34] L. S. Levitov, H. Lee, and G. B. Lesovik, "Electron counting statistics and coherent states of electric current," *J. Math. Phys.*, vol. 37, p. 4845, 1996.

[35] I. P. Levkivskyi and E. V. Sukhorukov, "Noise-Induced Phase Transition in the Electronic Mach-Zehnder Interferometer," *Phys. Rev. Lett.*, vol. 103, p. 036801, 2009.

[36] H. Förster, S. Pilgram, and M. Büttiker, "Decoherence and full counting statistics in a Mach-Zehnder interferometer," *Phys. Rev. B*, vol. 72, p. 075301, 2005.

[37] D. V. Averin and E. V. Sukhorukov, "Counting statistics and detector properties of quantum point contacts," *Phys. Rev. Lett.*, vol. 95, p. 126803, 2005.

[38] S. Gustavsson, R. Leturq, B. Simovic, R. Schleser, P. Studerus, T. Ihn, K. Ensslin, D. C. Driscoll, and A. C. Gossard, "Counting statistics and super-Poissonian noise in a quantum dot," *Phys. Rev. B*, vol. 74, p. 195305, 2006.

[39] S. Gustavsson, R. Leturq, B. Simovic, R. Schleser, P. Studerus, T. Ihn, K. Ensslin, D. C. Driscoll, and A. C. Gossard, "Counting statistics of single electron transport in a quantum dot," *Phys. Rev. Lett.*, vol. 96, p. 076605, 2006.

[40] B. Reulet, J. Senzier, and D. E. Prober, "Environmental effects in the third moment of voltage fluctuations in a tunnel junction," *Phys. Rev. Lett.*, vol. 91, p. 196601, 2003.

[41] X. Jehl, P. Payet-Burin, C. Baraduc, R. Calemczuk, and M. Sanquer, "Andreev Reflection Enhanced Shot Noise in Mesoscopic SNS Junctions," *Phys. Rev. Lett.*, vol. 83, p. 1660, 1999.

[42] L. Saminadayar and D. C. Glattli, "Observation of the e/3 Fractionally Charged

Laughlin Quasiparticle," *Phys. Rev. Lett.*, vol. 79, pp. 2526–2529, 1997.

[43] R. de Picciotto, M. Reznikov, M. Heiblum, V. Umansky, G. Bunin, and D. Mahalu, "Direct observation of a fractional charge," *Nature*, vol. 389, pp. 162–164, 1997.

[44] M. Brooks, "Seven wonders of the quantum world," *New Scientist*, vol. 2759, pp. 36–37, 2010.

[45] W. Ehrenberg and R. E. Siday, "The Refractive Index in Electron Optics and the Principles of Dynamics," *Proc. Phys. Soc. B*, vol. 62, p. 8, 1949.

[46] Y. Aharonov and D. Bohm, "Significance of Electromagnetic Potentials in the Quantum Theory," *The Physical Review*, vol. 115, p. 485, 1959.

[47] R. G. Chambers, "Shift of an Electron Interference Pattern by enclosed magnetic Flux," *Phys. Rev. Lett.*, vol. 5, pp. 3–5, 1960.

[48] R. Schuster, E. Buks, M. Heiblum, D. Mahalu, V. Umansky, and H. Shtrikman, "Phase measurement in a quantum dot via a double-slit interference experiment," *Nature*, vol. 385, p. 417, 1997.

[49] S. Pedersen, A. E. Hansen, A. Kristensen, C. B. Sørensen, and P. E. Lindelof, "Observation of quantum asymmetry in an Aharonov-Bohm ring," *Phys. Rev. B*, vol. 61, p. 5457, 2000.

[50] S. Datta, M. R. Melloch, S. Bandyopadhyay, R. Noren, M. Vaziri, M. Miller, and R. Reifenberger, "Novel Interference Effects between Parallel Quantum Wells," *Phys. Rev. Lett.*, vol. 55, p. 2344, 1985.

[51] A. Aharony, O. Entin-Wohlmann, T. Otsuka, S. Katsumoto, H. Aikawa, and K. Kobayashi, "Breakdown of phase rigidity and variations of the Fano effect in closed Aharonov-Bohm interferometers," *Phys. Rev. B*, vol. 73, p. 195329, 2006.

[52] U. F. Keyser, C. Fühner, S. Borck, R. J. Haug, M. Bichler, G. Abstreiter, and W. Wegscheider, "Kondo Effect in a Few-Electron Quantum Ring," *Phys. Rev. Lett.*, vol. 90, p. 196601, 2003.

[53] D. Chang, G. L. Khym, K. Kang, Y. Chung, H. Lee, M. Seo, M. Heiblum, D. Mahalu, and V. Umansky, "Quantum mechanical complementarity probed in a closed-loop Aharonov-Bohm interferometer," *Nat. Phys.*, vol. 4, pp. 205–209, 2008.

[54] M. Born and E. Wolf, *Principles of Optics*. Cambridge University Press, 1999.

[55] A. C. Elitzur and L. Vaidman, "Quantum mechanical interaction-free measurements," *Foundations of Physics*, vol. 23, pp. 987–997, 1993.

[56] P. Kwiat, H. Weinfurter, T. Herzog, A. Zeilinger, and M. Kasevich, "Experimental Realization of Interaction-Free Measurement," in *Symposium on the Foundations of Modern Physics*, 1994.

[57] R. Hanbury Brown and R. Q. Twiss, "A Test of a New Type of Stellar Interferometer on Sirius," *Nature*, vol. 178, pp. 1046–1048, 1956.

[58] T. Jeltes, J. M. McNamara, W. Hogervorst, W. Vassen, V. Krachmalnicoff, M. Schellekens, A. Perrin, H. Chang, D. Boiron, A. Aspect, and C. I. Westbrook, "Comparison of the Hanbury Brown-Twiss effect for bosons and fermions," *Nature*, vol. 445, pp. 402–405, 2007.

[59] I. Neder, N. Ofek, Y. Chung, M. Heiblum, D. Mahalu, and V. Umansky, "Interference between two indistinguishable electrons from indipendent sources," *Nature*, vol. 448, p. 333, 2007.

[60] V. S.-W. Chung, P. Samuelsson, and M. Büttiker, "Visibility of current and shot noise in electrical Mach-Zehnder and Hanvury Brown Twiss interferometers," *Phys. Rev. B*, vol. 72, p. 125320, 2005.

[61] M. Büttiker, P. Samuelsson, and E. V. Sukhorukov, "Entangled Hanbury Brown Twiss effects with edge states," *Physica E*, vol. 20, pp. 33–42, 2003.

[62] P. Roulleau, F. Portier, D. C. Glattli, P. Roche, A. Cavanna, G. Faini, U. Gennser, and D. Mailly, "Finite bias visibility of the electronic Mach-Zehnder interferometer," *Phys. Rev. B*, vol. 76, p. 161309(R), 2007.

[63] F. Pobell, *Matter and Methods at Low Temperature*. Springer, 1996.

[64] U. Graumann, *Ohmsche Kontakte zu zweidimensionalen Elektronensystemen*. personal script.

[65] E. J. Koop, M. J. Iqbal, F. Limbach, M. Boute, B. J. Van Wees, D. Reuter, A. D. Wieck, B. J. Kooi, and C. H. Van Der Wal, "The annealing mechanism of AuGe/Ni/Au ohmic contacts to a two-dimensional electron gas in GaAs/AlGaAs heterostructures," *arXiv:0809.0928v1*, 2008.

[66] A. K. Hüttel, K. Eberl, and S. Ludwig, "A widely tunable few-electron droplet," *J. Phys.: Condens. Matter*, vol. 19, p. 236202, 2007.

[67] M. Kataoka, C. J. B. Ford, G. Faini, D. Mailly, M. Y. Simmons, D. R. Mace, C.-T. Liang, and D. A. Ritchie, "Detection of Coulomb Charging around an Antidot in the Quantum Hall Regime," *Phys. Rev. Lett.*, vol. 83, p. 160, 1999.

[68] C. J. B. Ford, P. J. Simpson, I. Zailer, D. R. Mace, M. Yosefin, M. Pepper, D. A. Ritchie, J. E. F. Frost, M. P. Grimshaw, and G. A. C. Jones, "Charging and double-frequency Aharonov-Bohm effects in an open system," *Phys. Rev. B*, vol. 49, p. 17456, 1994.

[69] L. V. Litvin, A. Helzel, H. P. Tranitz, W. Wegscheider, and C. Strunk, "Two beam Aharonov-Bohm interference in the integer quantum Hall regime," *Physica E*, vol. 40, pp. 1706–1708, 2008.

[70] L. V. Litvin, H. P. Tranitz, W. Wegscheider, and C. Strunk, "Decoherence and single electron charging in an electronic Mach-Zehnder interferometer," *Phys. Rev. B*, vol. 75, p. 033315, 2007.

[71] L. V. Litvin, A. Helzel, H. P. Tranitz, W. Wegscheider, and C. Strunk, "Edge-channel interference controlled by Landau level filling," *Phys. Rev. B*, vol. 78, p. 075303, 2008.

[72] L. V. Litvin, A. Helzel, H. P. Tranitz, W. Wegscheider, and C. Strunk, "Phase of the transmission amplitude for a quantum dot embedded in the arm of an electronic Mach-Zehnder interferometer," *Phys. Rev. B*, vol. 81, p. 205425, 2010.

[73] A. Yacoby, M. Heiblum, D. Mahalu, and H. Shtrikman, "Coherence and Phase Sensitive Measurements in a Quantum Dot," *Phys. Rev. Lett.*, vol. 74, p. 4047, 1995.

[74] E. Buks, R. Schuster, D. Heiblum, M. Mahalu, V. Umansky, and H. Shrtikman, "Measurement of phase and magnitude of the reflection coefficient of a quantum dot," *Phys. Rev. Lett.*, vol. 77, p. 4664, 1996.

[75] K. Kobayashi, H. Aikawa, S. Katsumoto, and Y. Iye, "Tuning of the Fano effect through a quantum dot in an Aharonov-Bohm interferometer," *Phys. Rev. Lett.*, vol. 88, p. 256806, 2002.

[76] M. Hashisaka, Y. Yamauchi, K. Chida, S. Nakamura, K. Kobayashi, and T. Ono, "Noise measurement system at electron temperature down to 20 mK with combinations of the low pass filters," *Review of Scientific Instruments*, vol. 80, p. 096105, 2009.

[77] P. Roulleau, F. Portier, P. Roche, A. Cavanna, G. Faini, U. Gennser, and D. Mailly, "Direct measurement of the coherence length of edge states in the integer quantum Hall regime," *Phys. Rev. Lett.*, vol. 100, p. 126802, 2008.

[78] E. Bieri, M. Weiss, O. Göktas, M. Hauser, C. Schönenberger, and S. Oberholzer, "Finite-bias visibility dependence in an electronic Mach-Zehnder interferometer," *Phys. Rev. B*, vol. 79, p. 245324, 2009.

[79] Y. Yamauchi, M. Hashisaka, S. Nakamura, K. Chida, S. Kasai, T. Ono, R. Leturcq, K. Ensslin, D. C. Driscoll, A. C. Gossard, and K. Kobayashi, "Universality of bias- and temperature-induced dephasing in ballistic electronic interferometers," *Phys. Rev. B*, vol. 79, p. 161306(R), 2009.

[80] J. P. Bird, K. Ishibashi, M. Stopa, Y. Aoyagi, and T. Sugano, "Coulomb blockade of the Aharonov-Bohm effect in GaAs/Al_xGa_{1-x}As quantum dots," *Phys. Rev. B*, vol. 50, p. 14983, 1994.

[81] A. E. Hansen, A. Kristensen, S. Pedersen, C. B. Sørensen, and P. E. Lindelof, "Mesoscopic decoherence in Aharonov-Bohm rings," *Phys. Rev. B*, vol. 64,

p. 045327, 2001.

[82] K. Kobayashi, H. Aikawa, S. Katsumoto, and Y. Iye, "Probe-Configuration-Dependent Decoherence in an Aharonov-Bohm Ring," *J. Phys. Soc. Jpn*, vol. 71, p. L2094, 2002.

[83] M. Cassé, Z. D. Kvon, G. M. Gusev, E. B. Olshanetskii, L. V. Litvin, A. V. Plotnikov, D. K. Maude, and J. C. Portal, "Temperature dependence of the Aharonov-Bohm oscillations and the energy spectrum in a single-mode ballistic ring," *Phys. Rev. B*, vol. 62, p. 2624, 2000.

[84] M. Hashisaka, A. Helzel, S. Nakamura, L. Litvin, Y. Yamauchi, K. Kobayashi, T. Ono, H.-P. Tranitz, W. Wegscheider, and C. Strunk, "Temperature dependence of the visibility in an electronic Mach-Zehnder interferometer," *Physica E*, vol. 42, pp. 1091–1094, 2010.

[85] I. P. Levkivskyi, A. Boyarsky, J. Fröhlich, and E. V. Sukhorukov, "Mach-Zehnder interferometry of fractional quantum Hall edge states," *Phys. Rev. B*, vol. 80, p. 045319, 2009.

[86] J. T. Chalker, Y. Gefen, and M. Y. Veillette, "Decoherence and interactions in an electronic Mach-Zehnder interferometer," *Phys. Rev. B*, vol. 76, p. 085320, 2007.

[87] I. Neder, M. Heiblum, Y. Levonson, D. Mahalu, and V. Umansky, "Unexpected behavior in a two-path electron interferometer," *Phys. Rev. Lett.*, vol. 96, p. 016804, 2006.

[88] S.-C. Youn, H.-W. Lee, and H.-S. Sim, "Nonequilibrium dephasing in an electronic Mach-Zehnder interferometer," *Phys. Rev. Lett.*, vol. 100, p. 196807, 2008.

[89] I. Neder and E. Ginossar, "Behavior of electronic interferometers in the nonlinear regime," *Phys. Rev. Lett.*, vol. 100, p. 196806, 2008.

[90] D. L. Kovrizhin and J. T. Chalker, "Multiparticle interference in electronic Mach-Zehnder interferometers," *Phys. Rev. B*, vol. 81, p. 155318, 2010.

[91] F. Marquardt and C. Neuenhahn, "Dephasing by electron-electron interactions in a ballistic Mach-Zehnder interferometer," *New J. Phys.*, vol. 10, p. 115018, 2008.

[92] I. Neder, F. Marquardt, M. Heiblum, D. Mahalu, and V. Umansky, "Controlled dephasing of electrons by non-gaussian shot noise," *Nat. Phys.*, vol. 3, p. 534, 2007.

[93] P. Roulleau, F. Portier, P. Roche, A. Cavanna, G. Faini, U. Gennser, and D. Mailly, "Noise Dephasing in Edge States of the Integer Quantum Hall Regime," *Phys. Rev. Lett.*, vol. 101, p. 186803, 2008.

[94] I. Neder and F. Marquardt, "Coherence oscillations in dephasing by non-Gaussian shot noise," *New J. Phys.*, vol. 9, p. 112, 2007.

[95] C. Altimiras, H. le Sueur, U. Gennser, A. Cavanna, D. Mailly, and F. Pierre, "Non-equilibrium edge-channel spectroscopy in the integer quantum Hall regime," *Nat. Phys.*, vol. 6, pp. 34–39, 2010.

[96] H. le Sueur, C. Altimiras, U. Gennser, A. Cavanna, D. Mailly, and F. Pierre, "Energy Relaxation in the Integer Quantum Hall Regime," *Phys. Rev. Lett.*, vol. 105, p. 056803, 2010.

[97] C. Altimiras, H. le Sueur, U. Gennser, A. Cavanna, D. Mailly, and F. Pierre, "Tuning Energy Relaxation along Quantum Hall Channels," *Phys. Rev. Lett.*, vol. 105, p. 226804, 2010.

[98] I. P. Levkivskyi and E. V. Sukhorukov, "Energy relaxation at quantum Hall edge," *Phys. Rev. B*, vol. 85, p. 075309, 2012.

[99] *http://www-app.uni-regensburg.de/Fakultaeten/Physik/Weiss/Wiki/index.php*.

Acknowledgement

This thesis did not develop without some help of other people. And here I would like to thank all of them for their kind support. For their help especially to my scientific work, I thank

- *Prof. Dr. Christoph Strunk*, my advisor, for giving me the opportunity to work on a topic on which only few people in the world work on. He always was there when there was the necessity to discuss problems and data. He gave me any support he could and for the things he could not, he found collaborators for me. Having different approaches to understand physics, all discussions turned out to be productive.
- *Dr. Leonid V. Litvin*, for teaching me everything I needed to know about how to build and how to measure Mach-Zehnder interferometers. In the first years of my PhD, he was the basis of my scientific work. And also in every other aspect of the work, may it be help in the lab, fixing the fridge, or working in the cleanroom. Without his supervision, this thesis wouldn't be, what it is now.
- *Dr. Eugene V. Sukhorukov* and *Dr. Ivan P. Levkivskyi*, the theoreticians every experimentalist so strongly needs. More than their pure theory, it was their patience to explain me the formulas they derived, so I would understand finally. I wouldn't know what I was measuring all the time, if they were not there to show me. Every e-mail I received from them increased my understanding of the physics, that lay beneath the data.
- *Prof. Dr. Kobayashi Kensuke*, who gave me the possibility to work for three months in his research group in Kyoto, Japan. It was a very constructive time to work and discuss with him, and even when the measurements turned out to be less successful, he showed the understanding, that this things can happen. And I want to thank all members of his research group and of the chair of Prof. Dr. Ono Teruo, and especially Dr. Hashisaka Masayuki and Dr. Nakamura Shuji, who accompanied me not only in the lab. I want to thank everyone very heartly for giving me a "home" in Japan, for raw beef liver and sake.
- *Dr. Stefan Ludwig*, our collaborator of the SFB 631. He always had good advice concerning 2DEG and top gate structure and was always interested in our Regens-

burg projects. It was always nice to stay a day in Munich and talk about physics. In the course of this, I also want to thank every member of the SFB 631, with whom I could spend time during workshops and meetings.

- *Prof. Dr. Werner Wegscheider*, *Dr. Dieter Schuh* and *Imke Gronwald* supplied me with great high mobility semiconductor heterostructures. And also when I had problems contacting the 2DEG, they gave me advise.
- *Prof. Dr. Dieter Weiss*, the head of the chair at which this work was performed, for the well equipped clean room and all the other facilities.

The direct help from the mentioned people for my work was necessary and important! Nevertheless, I wouldn't have been able to complete this thesis without additional support with rather "practical" things. So here I like to thank

- Claudia Rahm and Elke Haushalter, the secretaries of our chair and the real center of it. Without their endeavors and guidance and understanding when it comes to bureaucracy or any problem that arises in daily life at the chair, only few things would work. Their door was always open for help, they always had easy and simple solutions, which made life in the chair so much easier.
- Uli, Tom and Micheal, our technicians, who were always there when one needed some machine fixed, heavy metal, weld or even grind a cryostat.
- Christian Haimerl und Thomas Solleder, the "helium guys". They supplied me with all the liquid helium I needed, even when the liquefier hardly worked or when bringing back the helium can too late.
- Dieter Riedl and all other members of the electronic workshop, who can fix any electronic device, or who just build anything of which one gives them a curcuit diagram and even, by the way, improving it.

The above persons did not only support me directly in my work, but also morally and personally. However, there are persons, whom I want to thank especially for this kind of help

- Markus and Tom, with whom I shared more than just the office for many years and known even since the times of the diploma thesis. It was always fun and interesting to discuss and talk to them about pretty much everything that one faces in the work and in live. No Quake could destroy our team spirit.
- all the members of the chair and especially of our group. It was a pleasure to be with such a variety of characters, to learn from them and enjoy their creativity during our usual afternoon cake or cookies. Matthias, Sung-Ho, Magda (by now honorary member of the group), Daniel, Daniel, Sasmita, Flo, Juri, Alois, Peter and all other students that joined temporary, thank you all.

Finally I want to thank the people who took the effort to proofread this thesis. First of all Magda, who was a even greater help than any textbook. Markus not only had to suffer from all my talking about Mach-Zehnder interferometers in the office, but also worked his way through the most important chapters. Andi (not me) contributed a lot to improve the language.